Master Thesis, Department of Geosciences

Geomechanical and Structural characteristics of of a paleoreservoir-caprock sucsession

Sandstones of Humbugflats, Central Utah

Eivind B. Larsen

UNIVERSITY OF OSLO

FACULTY OF MATHEMATICS AND NATURAL SCIENCES

Geomechanical and Structural characteristics of a paleoreservoir-caprock sucsession

Sandstones of Humbugflats, Central Utah

Eivind B. Larsen

Master Thesis in Geosciences

Discipline: Structural Geology

Department of Geosciences
Faculty of Mathematics and Natural Sciences

University of Oslo

June 2015

Supervisors: Alvar Braathen and Elin Skurtveit
This work is published digitally through DUO – Digitale Utgivelser ved UiO
http://www.duo.uio.no
It is also catalogued in BIBSYS (http://www.bibsys.no/english)

Abstract

Different horizons within an exposed deformed sedimentary sequence can, along with the fracture pattern, potentially be utilized by reducing fluids, in turn altering the mineralogical composition of the unit. Potentially resulting in discoloring (bleaching) and changes to the mechanical integrity of an entire layer, exemplified by a paleo-reservoir in an exposed sequence of the Entrada Sandstone in Utah, USA. The main focus of this study has been to investigate the mechanical strengths of the different units and map the fracture patterns in order to provide detailed data on the different lithologies. Further trying to find patterns in the collected data, in both the fracture patterns, supplemented with data on the deformation bands within the paleo-reservoir, and within the mechanical properties of the different units. Detailed mapping of the fractures has been conducted on the studied outcrop, situated at Humbugflats on the north end of the San Rafael Swell. In total 82 tests have been conducted to get constraints on the mechanical differences of the units.

The data gathered on the fractures generally concur with previous studies conducted in the area, with minor differences. The fractures and deformation bands can be populated into two main fracture populations and three deformation band populations. The mechanical data reveal that the mechanical strength of the units is related to the porosity of the rock within, in consensus with earlier studies.

The mechanism for the proposed bleaching in the paleo reservoir is thought to be a reducing fluid, saturated with CO_2 driven by buoyancy. Causing fluid migration along fractures and into the paleo-reservoir, increasing the fluid pressure in the reservoir causing it to extensively deform. The results of this study provide a summary for geomechanical differences caused by bleaching and fluid saturation of a paleo-reservoir.

Acknowledgments

This master´s thesis would not have been possible without the help from my supervisors, Alvar Braathen and Elin Skurtveit. I would like to thank Alvar for his guidance during the filed work and for answering my questions whenever needed, and Elin for helping me with all the geotechnical work.

For helping me and allowing me to use their lab, a huge thanks to everyone at The Norwegian Geotechnical Institute (NGI) laboratory and NGI, especially Reidar Otter, Magnus Soldal and Sven Vangbæk.

A huge thanks go out to Ida Hope for driving me around all of Utah and good discussion regarding our findings in the field, along with Ivar Mitkandal for helping out during the field work.

I would also like to thank everyone at ZEB, particularly Ingrid and Henning for sharing their coffee with me, and my passion for brakes. And to Christian and Tor for being the coolest people I know.

And finally an enormous thanks to Ine, for choosing to live with me and for being supporting no matter what.

Contents

1 Introduction

1.1 Aim of work

At the northern end of the San Rafael swell, Utah, USA a pristine example of an unroofed, presumed bleached, paleo-reservoir stands out as a single white layer amongst predominantly red sandstone in an exposed sedimentary sequence.

This study aims to put forth a detailed description of the fracture pattern of said exposure which along with a geomechanical framework found for the sequence addresses the geomechanical differences resulting in the intensely deformed paleo-reservoir exposed today.

The study is based on data gathered through field investigations and laboratory work at the Norwegian Geotechnical Institute (NGI). Recordings and descriptions of fractures, deformation bands and faults within the exposed sequence along with more general geological background form the basis for the field observations. The laboratory work is comprised of samples collected from selected layers tested for tensile strength and uniaxial compressive strength (UCS).

The paleo-reservoir exposed in the sedimentary sequence can be used as an analog to potential CO2-storage reservoirs today. It is therefore important to have an extensive understanding of how the reservoir "reacts" to an introduced CO_2 bearing fluid. Is the mechanical integrity of the reservoir changed as a result of the introduced fluid and increased fluid pressure, if this is the case what caused the geomechanical differences in the studied rock? If a potential CO_2-reservoir is found in red Jurassic sandstones, "bleaching" becomes an important factor. Can the bleaching potentially reduce the strength of the layer as hematite is removed from the grains? These and a lot of other unanswered questions are important to investigated further. These aspects of CO_2 storage are important as they key observations to have choosing potential reservoirs.

1.2 Regional geology

1.2.1 Geological setting

The studied outcrop is situated at north end of the Humbugflats in Utah, USA, inside the San Rafael Swell, one of the most prominent features of the Colorado plateau (described in greater detail bellow). The Colorado plateau is geographically an elevated desert situated at the boarder area of the four corners between Utah, Colorado, Arizona and New Mexico (Fig. 1.1). Today the Colorado plateau is at an approximately 2km above sea level (Pederson et al., 2002), the present day situation came after the initial rise of the Colorado plateau area during the late Cretaceous and early Paleocene (Fillmore, 2011).

Figure 1.1 The Colorado Plateau outlined in red, covering vast areas of Utah, Colorado, Arizona and New Mexico. Modified from Google earth satellite image

1.2.2 Structure

Humbugflats is situated on the north end of the San Rafael swell in front of the eastern limb of a large anticline/monocline structure (see fig 1.2). This large monocline is a result of contraction during the Laramide Orogeny, starting in the late Cretaceous, ending in Paleocene (Bump and Davis, 2003, Pederson et al., 2002, Fillmore, 2011, Davis, 1999, Davis, 1978). The driving forces behind the Laramide orogeny has been heavily debated throughout the years, but today there is overall consensus that it links to shallowing subduction of the oceanic Farallon plate beneath North America. What caused this change in subduction is still debated (Fillmore, 2011). Alongside the above-mentioned San Rafael swell, the Laramide orogeny is seen as a number of similar uplift-features, or rather basement cored monoclines of the Colorado plateau, e.g Monument

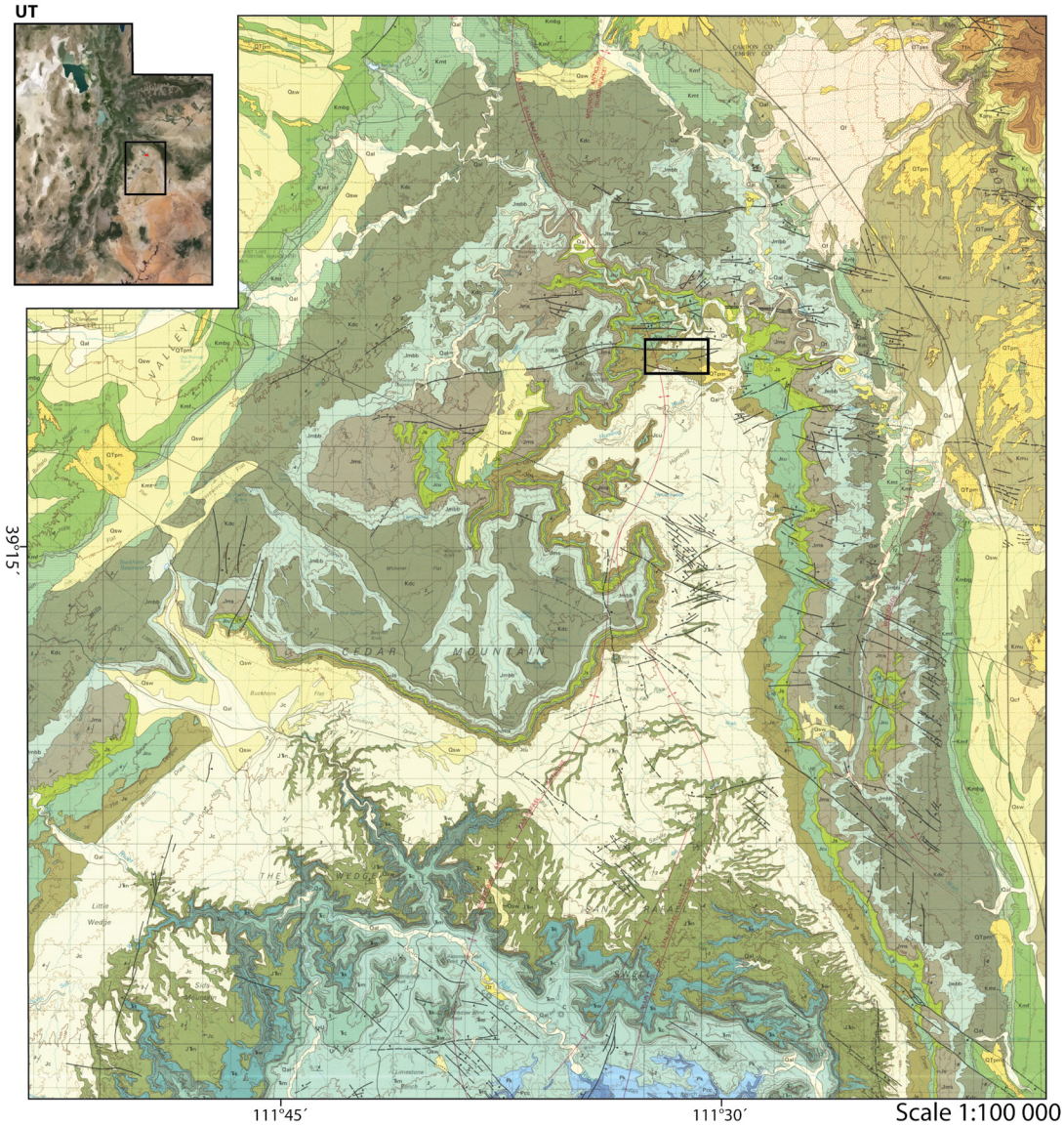

Figure 1.2 Geological map of the study area, outlining the San Rafael Swell and Location of the study area within. Modified from Witkind (1988).

Uplift and Kaibab Uplift. However, the deep root in basement and deformation of the overburden are complex and not fully understood for all uplifts (Bump and Davis, 2003, Solum et al., 2010). Another enigmatic issue is the reactivation of faults during this period, impact areas fare away from the active subduction zone (Fillmore, 2011). The events mentioned are chronically summarized in figure 1.3.

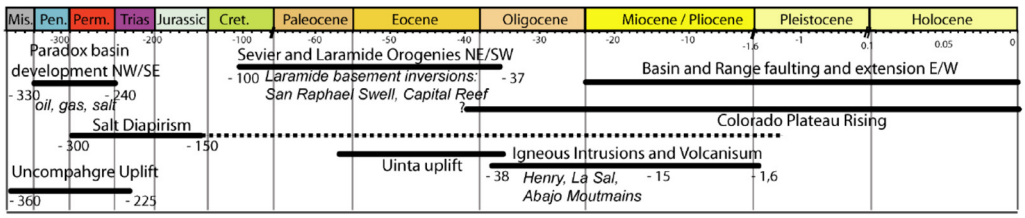

Figure 1.3 Age relationships between major tectonic events and known uplifts and basins. Taken from Frery (2012).

The San Rafael Swell, a 130km long and 55 km wide prominent geographical and geological feature, stands out from the surrounding plateau with a greater relief then its surroundings. The swell is an asymmetrical anticline, or monocline, verging east and trending in a NNE direction, bound by a striking moderately dipping limb along its eastern margin (Davis, 1999, Davis, 1978, Bump and Davis, 2003). Interpretation of the structures ascribed it to a deep thrust uplifting basement towards the east (Bump and Davis, 2003). Reactivated faults during the Laramide Orogeny are believed to control the location of the swell during Precambrian (Fillmore, 2011, Solum et al., 2010).

A number of younger faults active in the late Cretaceous to Paleocene and possibly again in the Quaternary are found in this part of Utah, cutting into the older structures. The best known fault activity linked to plausible deep salt movement is the Moab Fault followed along strike to the NE by the Little Grand Wash fault, Salt Wash Graben and Iron Wash fault (Foxford et al., 1998, Dockrill and Shipton, 2010, Richey, 2013). These are typically relatively steeply dipping normal faults, likely originating from Triassic (Foxford et al., 1998). The chronological relationships between the normal faults and the San Rafael swell are questionable, but Richey (2013) argues that they post-date the swell during late reactivation(s).

1.2.3 Stratigraphy

The sedimentary sequence in these parts of Utah is predominantly of Cretaceous and Jurassic age, deposited in a fluctuating depositional environment. The Jurassic units display the change from a non-marine depositional environment in the early Jurassic, into a marine depositional environment in an epicontinental sea during the middle Jurassic before going back into deposition in non-marine basin during the late Jurassic (Hintze and Kowallis, 2009). In ascending order from the oldest to the youngest the different lithologies found in the area are; Entrada Ss., Curtis Fm., Summerville Fm., Morrison Fm., Cedar Mt. Fm., Dakota Ss. and Mancos Shale. Bellow The Entrada Ss. the older Carmel Fm. and Navajo Ss. (see fig.1.4), present in small outcrops further south in the San Rafael swell. The studied outcrop is mainly consisting of sedimentary rock of the Entrada Ss., although a small part of the Curtis Fm. can be seen above.

The Entrada Ss. is divided into three principal members, in stratigraphic ascending order; Dewey Bridge Member, Slick Rock Member and Moab Tongue Member. Members that are not as widespread as the above mentioned are also found. the so-called earthy member of Entrada Ss. is a lesser extent member, that can be correlated to the Slick rock member in other areas (O'Sullivan, 2010). The Dewey Bridge member is consisting mostly of costal sabkha deposits of sand, silt and mudstones (Chan et

al., 2000). The Slick rock member, which overlies the Dewy bridge member consists of eolian sandstone dune bodies. This marks the transition from beach to eolian dune deposits, with the more silt dominated Dewy Bridge member into the higher permeability sandstone units of the Slick Rock member (Chan et al., 2000). The different individual sandstone bodies of the Slick Rock member are relatively limited in size laterally, and are interlaid by sabkha siltstones (Garden et al., 2001). The Moab Tongue member is made up of mostly white colored sandstones, relatively large in lateral extent (Chan et al., 2000). The Earthy member encountered in the study area is most likely deposited in a marine to marginal marine / costal plain setting containing fine-grained red beds and irregular crevasse splay channels (O'Sullivan, 2010).

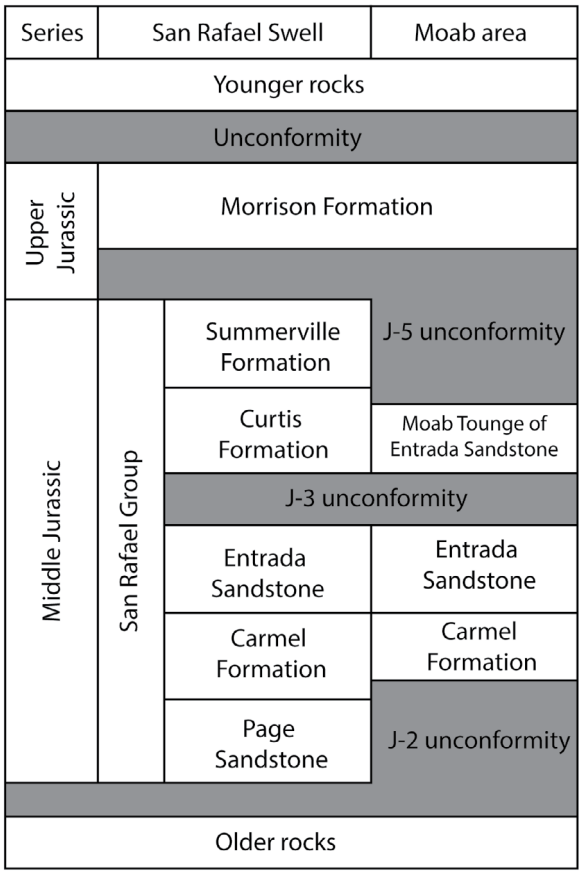

Figure 1.4 Simplified stratigraphy of the San Rafael Swell and Moab area, showing their relative positions. Modified from O'Sullivan (2010).

The Curtis Fm. lies unconformable on top of the Entrada inside the San Rafael group, in literature referred to as the J-3 unconformity (O'Sullivan, 2010). The Curtis formation defines another marine event in this part of Utah. Marine fossils found in the Curtis formation in the San Rafael Swell and Capitol Reef areas indicates a short period of marine conditions between the fluvial/costal plain settings in both the bellow in the earthy facies of Entrada and above the Summerville formation (Hintze and Kowallis, 2009, O'Sullivan, 2010).

1.3 Definitions

Fractures are divided into two end members, extension and shear fractures, based on the type and direction of stress they form under. An extension fracture is created when the stress is applied parallel to the maximum tensile stress (normal stress), typically seen as a tensile fracture where the stress component is perpendicular to the fracture plane. A shear fracture is formed when stress is applied in the shear direction, displaying movement along the fracture plane (Gudmundsson, 2011). The two different end members can be described with the Mohr-Coulomb failure envelope, see fig. 1.5 Interested readers are referred to e.g. Gudmundsson (2011) for further details.

Bleaching is in this thesis referring to the alteration of the mineralogical composition of a rock, causing discoloring from red to white as a result of the removal of hematite grain coting by an external agent (Garden et al., 2001).

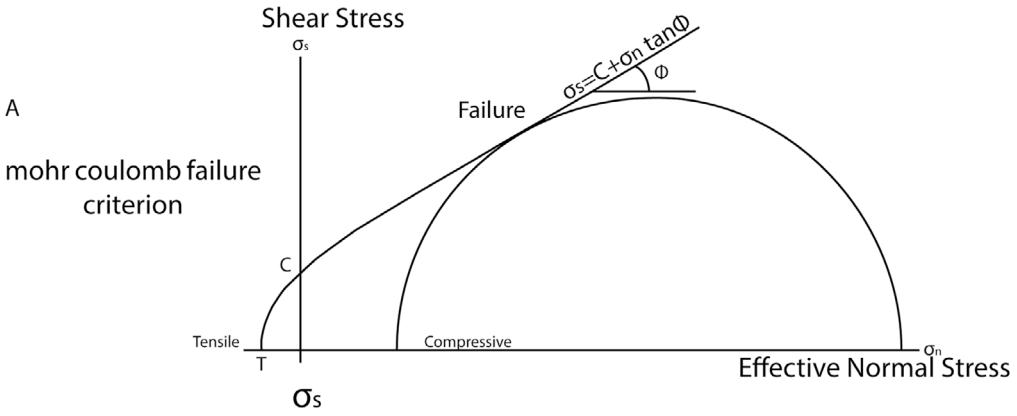

Figure 1.5 The Mohr-Coulomb failure criterion illustrating the difference between Normal stress causing a tensile failure and the shear stress causing a shear fracture. After Gudmundsson (2011).

2 Methods

This chapter covers the methods utilized to acquire the data used as basis for the following results and discussions. The methods will be divided into two sections, one for field methods and one for lab methods. The field methods are in situ measurements and data collection, while the lab methods are test procedures used during testing of the samples collected in the field. The methods are further divided into smaller sections based on their use and application.

2.1 Field methods

2.1.1 Techniques

Several different techniques were utilized to gather data in the field. All strike/dip measurements gathered during the fieldwork were recorded manually with a compass following the right hand rule. 1D Scan lines, as described by Singhal and Gupta (2010), were also used to collect statistical data on the distribution of fractures in the different layers of the succession studied. Each scan line had a length of 10m and the fractures within were counted per meter going northeast to southwest along the outcrop. This implies that fractures in an approximate direction parallel to the scan line, are rare in the statistical data, which in theory can create a bias in the dataset. Where possible, the scan lines were recorded parallel with the corresponding scan line from the layer above or below. The fractures were recorded as “through going” or “bed-confined”, whether they, as their respective label explain, are going through the whole succession or if they are restricted to their respective layer, mostly terminating at the interface of layers. The strike/ dip of every recorded fracture plane was also noted. Spherical fractures related to surface processes and erosion was disregarded based on their irregular orientation and appearance of the fracture plane.

2.1.2 Permeability measurements

To record the permeability of the respective layers in outcrop a mobile permeameter was used, specifically NER´s TinyPerm II. This device measures the time required to fill the vacuum created in the syringe/chamber of the TinyPerm by sucking air through the nozzle of the instrument, scaled to the rock surface. The response of the system is calculated and given as an output on the control unit. This number is then used to calculate the permeability with equation I. This equation is based upon the theoretical relationship between the response of the system and the permeability of the matrix (New England Research, 2015). Permeability measurements close to the Tiny perm II´s minimum threshold of 1 mD have previously been found to produce datasets with

a large bias. Magnabosco et al. (2014) have therefore suggested a correction, equation II, for measurements ranging from 0.001 to 2 mD. By applying the correction and removing permeability measurements bellow 0.1 mD they have reduce the uncertainty of their data significantly.

$$T=-0.8206 \log_{10} k + 12.8737 \qquad \textbf{I}$$

T is the TinyPerm value recorded and k is the permeability given in millidarcy.

To ensure good results the median value of three measurements, with a maximal error of +/- 0.2 at each, for each layer, was used to calculate the permeability.

$$Y = 12.091X + 4.5174 \qquad \textbf{II}$$

The linear relationship for Y, measured permeability and X, calculated plug permeability (Magnabosco et al., 2014).

2.1.3 Stratigraphic column

In order to create the stratigraphic column an imaginary 1D line through the stratigraphic sequence was recorded and logged like described in Nichols (2009). The style described by Nichols has to some extent been modernized, displaying bedding structures within the layers. The column was logged systematically from bottom to top, only to diverge from the imaginary line when necessary to get good observations. Along this line all layers were measured in thickness and grain size recorded. All structures, such as planar lamination, cross-lamination, cross stratification, burrows and roots and fossils were noted. Logging paper was used along with a grain size chart and typical symbols of bedding in accordance with USGS (2006) standards were used.

2.2 Lab methods

2.2.1 Sample preparation

The samples used during testing are prepared according to the standards for uniaxial compressive strength tests (UCS) and brazilian tests. These two standards will be thoroughly presented in the two following sections, 2.2.2 and 2.2.3. In this section the methods and techniques used for the preparation of the specimens are presented. The procedures prepping the samples are mostly analogous for the two, although the specimens used to test them are different. For the brazilian tests, discs are created with a diameter twice the thickness, while plugs with a long axis, ideally 5cm, are created for the UCS tests.

The samples collected in the field are assessed based on the strength of the material and their potential to create the highest number of specimens as possible. The strength of the material is assessed in order to determine if the sample is resilient enough to withstand the use of water in the preparation procedures. If the material is too weak, suction is used instead of water when the samples are cut and drilled. After the samples are assessed the layering on the rock samples are marked, and then cut accordingly into more convenient hand sizes. For these cutting procedures a diamante saw with a circular blade is used.

The next step in the preparation is to create two parallel surfaces on all the samples, corresponding with the layering of the sample. These surfaces will become the plane end-surfaces of the plugs produced for UCS tests. The parallelism of these surfaces is therefore important because the distribution of load in the plug is dependent on this, further elaboration on this can be found in section 2.3.3. To attain parallel surfaces on the stronger sandstone samples they are grinded down to a desired thickness with an accuracy of 0.001mm across the whole surface (fig. 2.1B). The weaker sandstones are not strong enough to withstand this type of grinding, much because water is used to moisten the surface and reduce friction. The parallelism of the surfaces created during sawing is therefore the highest accuracy achieved for these samples.

When all the samples have been through the first two steps, the plugs and discs can be drilled out. The drill points are marked in such a way that the material is exploited as much as possible (fig.2.1A). The specimen discs used to conduct brazilian tests are drilled with their long axis parallel to layering, while the plugs used for UCS tests specimens have their long axis perpendicular to layering. The setup used for the drilling is relatively simple (Fig. 2.1C and D). The sample is placed on large rock disc with a

higher density then the sample, this is done to ensure that the plug stays intact at the end of the drilling. Instead of drilling out of the sample in the bottom, the drill continues 5 mm into the rock disc below so the drill won't loose friction spinning the plug.

The sample is fixed with a plate on top, screwed down with nuts and bolts. On top of this suction or water is added. To secure even contact some gypsum is used to even out the roughness of the surface due to individual sand grains creating irregularities. When

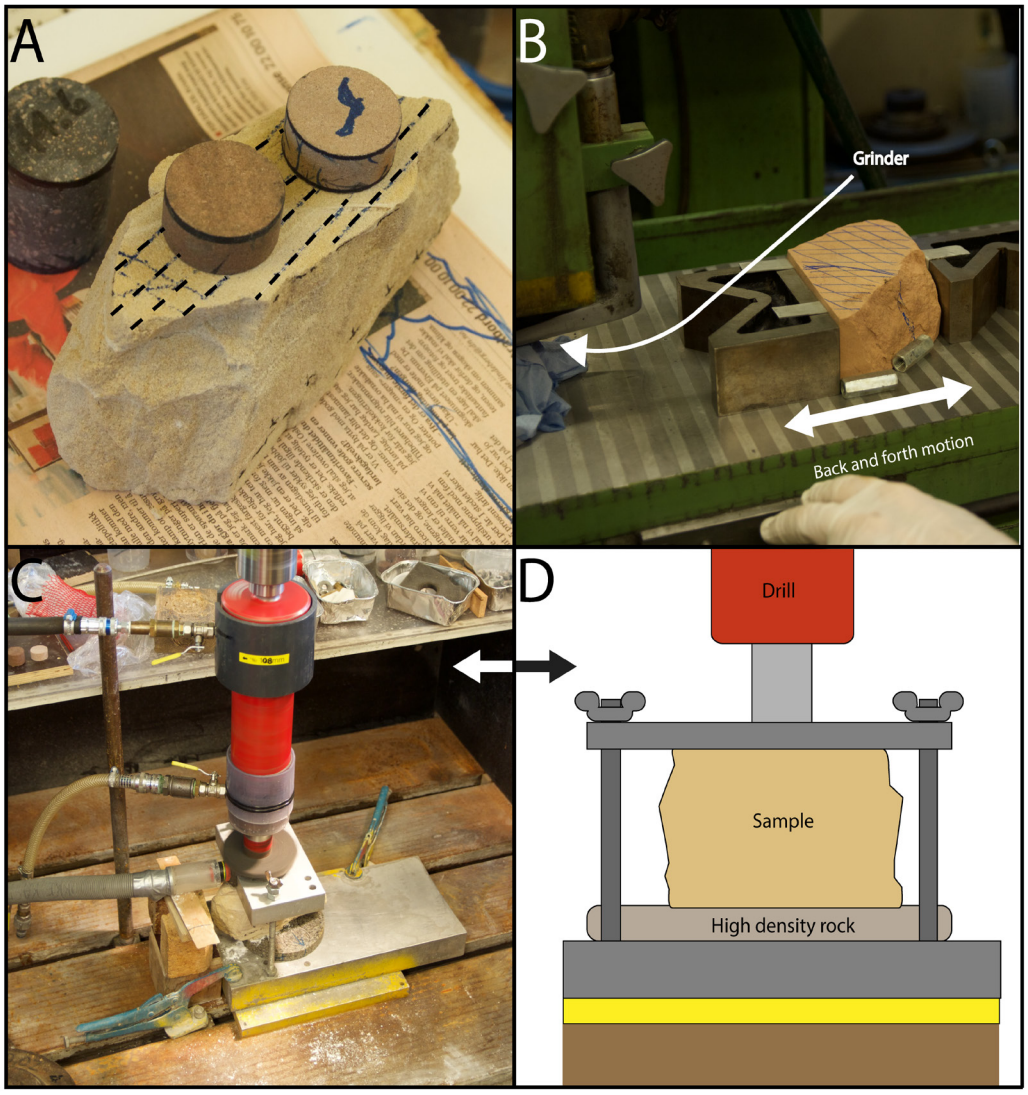

Figure 2.1. A; Illustrates the technique used to select plug drilling points on the specimen according to the layering. The layering is indicated with black stippled lines. B; The setup used for grinding. The sample is locked to the stage so it is unable to move. The stage goes back and forth underneath the grinder until a selected thickness for the sample is achieved. C; Drilling a UCS plug from a weak sandstone, where suction is used. D; A sketch of the drilling setup used for all the samples, either with water or suction.

drilling out the USC-plugs the samples are cut at the appropriate length before drilling. The Brazilian discs have to be cut afterwards, giving them the appropriate thickness. When cutting the Brazilian discs a pre-fabricated device is used to secure even and accurate cutting.

After the specimens are prepared from the hand samples, they are weighted and measured before the testing can start. In order to secure accurate measurements a digital scalar is used to measure the diameter and height/thickness of the specimens. In order to get accurate measurements both the diameter and height of the specimens are measured at different points and the average is calculated and used as their true value.

2.2.2 Porosity

The porosity of the investigated layers is calculated from the average bulk density and particle density. Since the reference layers all have a quartz-dominated mineralogy, the theoretical particle density of quartz, 2.65 g/cm^3, is used in the calculations for all the layers . The bulk density on the other hand is calculated from the weight and volume of the specimens created for the UCS and brazilian tests. In order determine the amount of space in-between the grains, i.e the porosity, the bulk density of the specimen is divided by the theoretical particle density of quartz as shown in the equation III (Palchik and Hatzor, 2004). Since the particle density of quartz is used, the calculated porosity will not be completely accurate, because the specimens consist of a range of particles besides the dominant quartz.

$$\phi = 1 - \frac{\rho_{bulk}}{\rho_{particle}} \qquad \textbf{III}$$

Where ϕ is the porosity and ρ is the density. For particle density, the theoretical particle density for quartz is used (2.65 g/cm^3), while the bulk density is calculated from the specimens.

The porosity calculations are supplemented with microscope observations. Thin sections were created from samples of the reference layers in order to determine the mineralogy and observe the porosity of the rocks. The rocks used for the thin sections were injected with blue epoxy in order to highlight the porosity of the material. The porosity can in this way be assessed in an effective way to supplement the calculations with observational data.

2.2.3 Tensile strength

To determine the tensile strength of the targeted layers in the succession, an indirect tensile strength was measured from samples that were collected from the respective layers in the field. This was done with brazilian tests conducted in the NGI lab.

Before one can start the testing the sample specimens, the apparatus must be adjusted according to the ISRM standards “suggested method for determining indirect tensile strength by the Brazil test”(Bieniawski and Hawkes, 1978).

The instrument used during the testing consists of a “loading component” that applies a load, pushing upon a “sample unit”. The “sample unit” consists of steel “jaws”, one upper and one lower. The upper jaw remains in position, while the lower jaw moves as load is applied. The jaws are adjusted to be in contact with the sample specimen so that the load is distributed along one plane. (fig. 2.2). The ISRM standard sets guidelines on the width, the curvature radius on area of contact and the distance between the guiding pins that ensures that the jaws move without rotating. The standard states that the jaws ideally have a width that’s 1.1 x specimen thickness, a radius that equals 1.5 x specimen radius and that the length of the guiding pins permits rotation of one jaw equal to 4 x 10^{-3} radians out of plane with regards to the other jaw(Bieniawski and Hawkes, 1978).

The sample specimen itself is prepared so that the diameter is as close to 25mm as possible, while the thickness of the sample is 0.5 x diameter. The standard states that the irregularities of specimens cylindrical shape should not exceed more than 0.025mm, and that the end faces shall be flat to 0.25mm and parallel to within 0.25°. Before the sample is ready to be tested, a layer of masking tape is wrapped around the sample to secure even contact between the steel jaws and the sample surface. During testing the load is applied at a constant rate to assure that the specimen fails at the weakest point. Failure should occur within 15-30 seconds after contact, to ensure a relatively homogenized and representative dataset (Bieniawski and Hawkes, 1978).

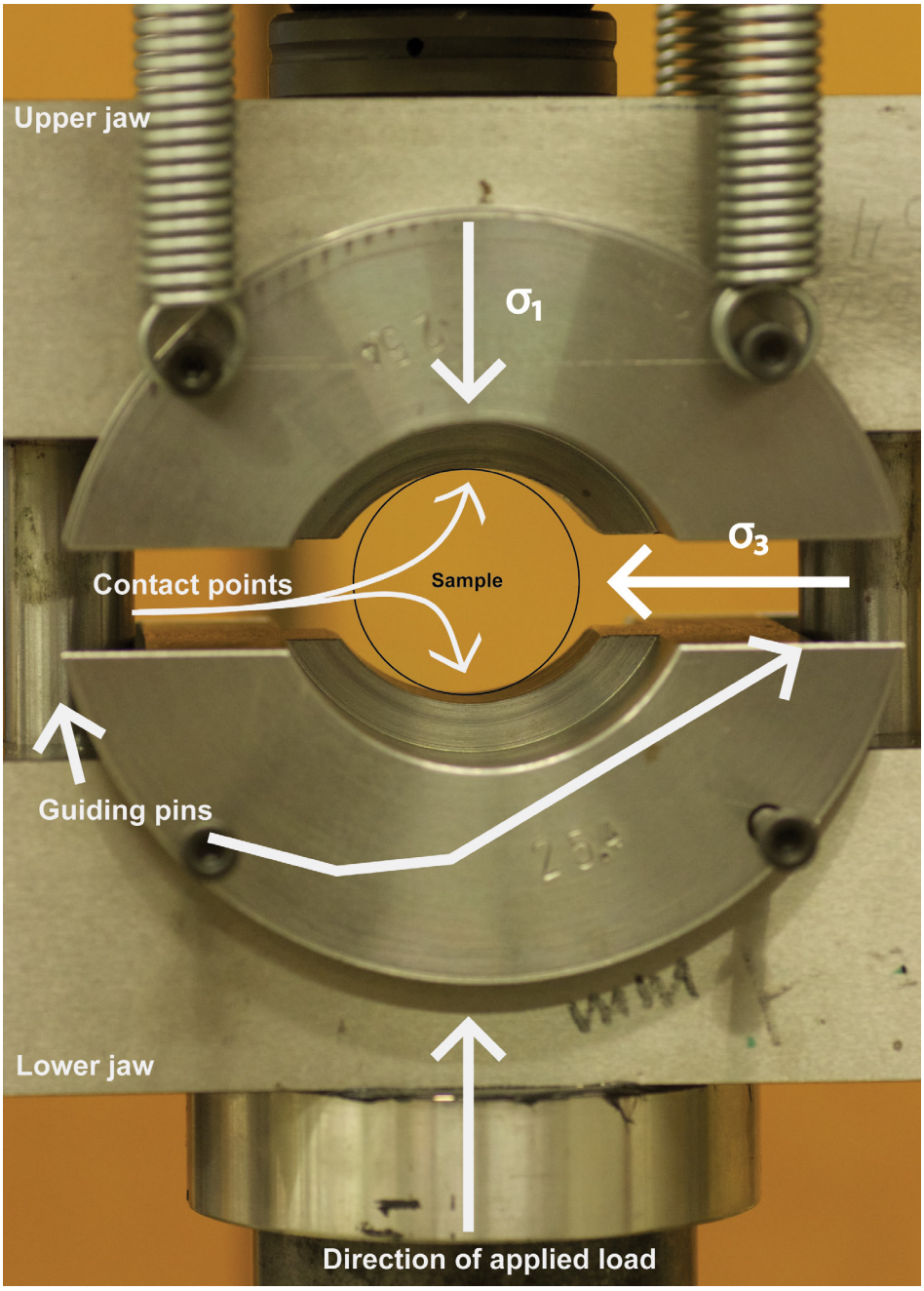

Figure 2.2. The “sample unit” of the instrument used during brazilian tests, with key parts labeled and direction of applied load marked. The principle stress axis are are also given.

To calculate the indirect tensile strength, σ_t, of the sample specimen, the following equation is used

$$\sigma_t = 0.636\frac{P}{Dt}(MPa) \qquad \textbf{IV}$$

P, is the recorded load at the point of tensile failure given in kilo newton. D is the diameter of the specimen while t is the thickness, both given in millimeter.

2.2.4 Compressive strength

For determination of the compressive strength, the ASTM (2010) standard for "Compressive Strength and Elastic Moduli of Intact Rock Core Specimens under Varying States of Stress and Temperatures" has been used to set up and conduct the tests. The procedures used follow the method used for "Uniaxial compressive strength of intact rock core specimens" (method C) found in the standard.

The loading device used to determine the compressive strengths is subjected to the same requirements as the one used determining the tensile strength. Therefore the same device is used in both tests. Besides the loading device, the tests are set up differently. The instrumenting is set up with two end plates, the lower one being mounted directly on the loading device and the top being mounted with half bearings so that it is able move freely. Both ends plates are fitted with p/s-wave transmitter/receivers to measure the p/s-wave velocities in the specimen during testing (fig. 2.3). For these transmitters/ receivers there are no standards stating how they should be mounted. They are located in such a way that they replace the contact end of the plates in the loading rig. Although it is an alteration of the setup described in the standard, the diameter of the transmitter/ receiver coincides with that of the specimen, like the end plates used/described in the standard. The setup used during these test should therefore be within the standard and have no impact on the end result.

The specimens used for testing are cylindrical rock cores, which have been drilled out of representative samples. The standard states that a desirable length to diameter is 2.0:1 up to 2.5:0, while ratios below this should be avoided. During preparation of the specimens, a ratio of 50 to 25 mm has been the ideal strived to achieve. Before testing, each specimen has been covered with glad-wrap to ensure that the samples are intact

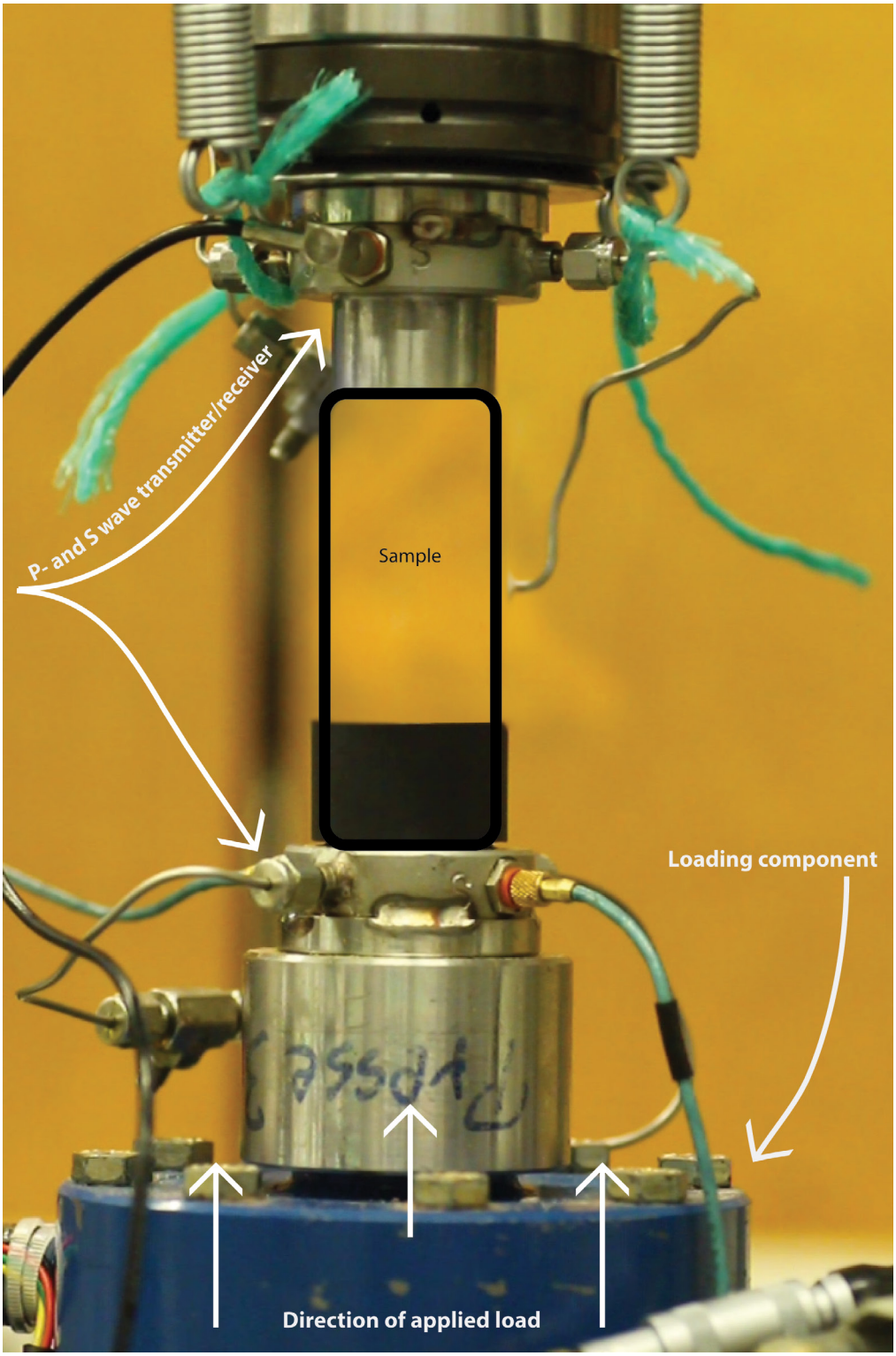

Figure 2.3. The sample- and load component setup used during the uniaxial compressive strength tests. Key parts are labeled and the direction of applied load is pointed out.

after testing. This wrap is not affecting the results.

During testing, the instrument is reset after each test. The specimen is inserted into the rig and aligned whit the top and bottom and spherical seat, free to move. Load is then applied continuously onto the sample with a rate allowing failure to occur within a time frame of 2-15 min. Load is measured at an interval of 1second, recording the peak load at failure.

The calculation of the uniaxial compressive strength, σ_u, can be done with the following formula.

$$\sigma_u = \frac{P}{A} \qquad \textbf{V}$$

Where P, is the peak load given in kilo newton and A is the cross sectional area given in square millimeter.

During testing the deformation is also recorded, in order to calculate the axial strain. Deformation is recorded at the same interval as the load, continuously through the test, with the aid of a gauge measuring the total change in the length of the whole system. The deformation is then calibrated afterwards in order to rectify for false deformation of the instrument. The methods used for this correction will be discussed in further detail in the next section. The strain is calculated in order to create a stress vs. strain curve to describe the mechanical changes in the specimen before failure.

The calculation of strain is based on the change in length of the gauge, using the following formula:

$$\varepsilon_a = \frac{\Delta L}{L} \qquad \textbf{VI}$$

Strain, $\varepsilon_{a,}$ is given as the measured change of length parallel to σ_1, ΔL, divided by the undeformed length/height of the sample, L.

2.2.5 Data management

Large datasets are recorded during the tests conducted in the laboratory. Depending on the raw data, different procedures have to be applied in order to create usable data. As explained in the previous sections, the same loading unit is used for both the brazilian and UCS tests. The tests will therefore naturally produce the same type of data output for both types. Consequently the same post-test procedures are used. The gauge used to record the load is calibrated before use and the data acquired from the test is accurate without any manipulation. In theory the data can therefore be used without correction, but the gauge starts recording the load from the point where the loading component is activated until it is turned of. This is problematic because the interest lies in the amount of load the specimen is able to withstand before failure, therefore a starting point must be selected. This point is defined as the point where the specimen comes in contact with the "sample unit" (Fig.s 2.2, 2.3).

In the raw data this can be found as the first point showing a steady rise in the recorded output values. At this point the data is zeroed, which means that the selected zero point is subtracted from itself and the following data points. This corrects the start and gives us the correct amount of load withstood by the specimen and not the whole system. In order to get even and comparable results, the individual tests should ideally have a relatively similar zero value/point. For the data collected during the UCS tests, a load of 0.05 kN marked the steady rise in the output data for most of the specimens tested. Therefore the value closest or equal to 0.05kN was chosen as a zero point creating a comparable dataset for all the specimens used for UCS testing. This was also done for the data recorded during the brazilian tests. Here a different zero value were selected for each layer because of the differences within the dataset.

When the zero value has been chosen a load vs time graph can be plotted. Common for both tests, Brazilian and UCS, is the procedure used to obtain the critical/ peak load recorded during testing. Application of load on a specimen at a constant rate allows strain to build up in the specimen until it reaches a critical load. This load is essentially the P value used in equation III and IV. The critical load can be detected in the graph at the point where the load drops significantly. This happens after the strain that has been built up in the specimen is released at failure (Fig 2.4). This drop looks a bit different for the graphs displaying a shear failure and a tensile failure (fig. 2.4A and B)

Alongside the load, the deformation of the specimens was also recorded during the UCS tests. In order to measure the deformation of the specimen, the change in height

of the whole system is measured. Like the raw data collected from the loading gauge, the raw data from the deformation measurements also has to be zeroed from the point of contact. This is done from the corresponding data point to the load selected as zero in the dataset. The deformation is accordingly set to zero and the measured deformation form this point is now within the specimen. Unlike the load gauge, the deformation gauge is not completely calibrated before testing.

Before the specimens are tested a false deformation test is conducted in order to find the amount of deformation within the equipment itself, the so-called false deformation. These data are used to create a correction curve used to to calibrate the deformation data for the other specimens post testing. The slope of the curve gives a function of deformation by load:

$$Y = 0.0058X + 0.0607 \qquad \textbf{VII}$$

Y, deformation as a function of X, load.

The linear function is given as y=Ax+B, when applied as a correction to the deformation, the B part of the function results in negative values shifting the results to a negative start. In order to not do another correction, the B part of the function is removed. The applied correction, Y=0.0058x, is then subtracted from the deformation data removing the false deformation from the data. The corrected data can now be used to calculate the strain as explained in the previous section.

2.2.6 Graphs

After the data has been processed two types of graphs are created, a load vs. time for both, Brazilian and UCS tests, and a stress vs. strain graph for the UCS tests. The load vs. time graph is used as a graphical illustration of the critical/ peak load recorded during testing and a supplement when selecting the right value from the dataset. Application of load on a specimen at a constant rate allows strain to build up in the specimen until it reaches a critical load. This load is essentially the P value used in equation III and IV. The critical load can be detected in the graph at the point where the load drops significantly. This happens after the strain that has been built up in the specimen is released at failure (Fig 2.4). This drop looks a bit different for the graphs displaying a shear failure and a tensile failure (fig. 2.4A and B).

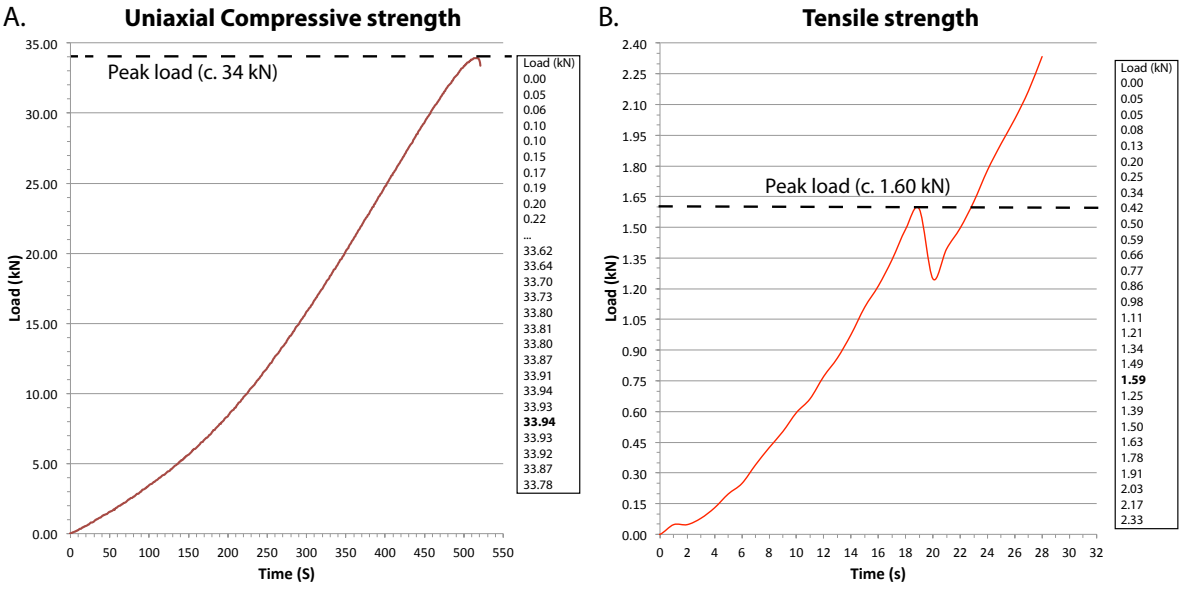

Figure 2.4 A: Load vs. time graph plotted from the UCS test results. B: Load vs. time graph plotted from the brazilian test results c. Both A and B illustrates the method used to select the value in combination with the data output. A section of the load data is displayed on right side of both graphs It is not always as straightforward as shown in this example. In weaker material it can be difficult to decide when and what the right peak value is. To supplement the dataset a camera-rig was used in determination of the point of failure. The camera equipment is a supplement to the existing methods, as it is too inaccurate to be used on its own.

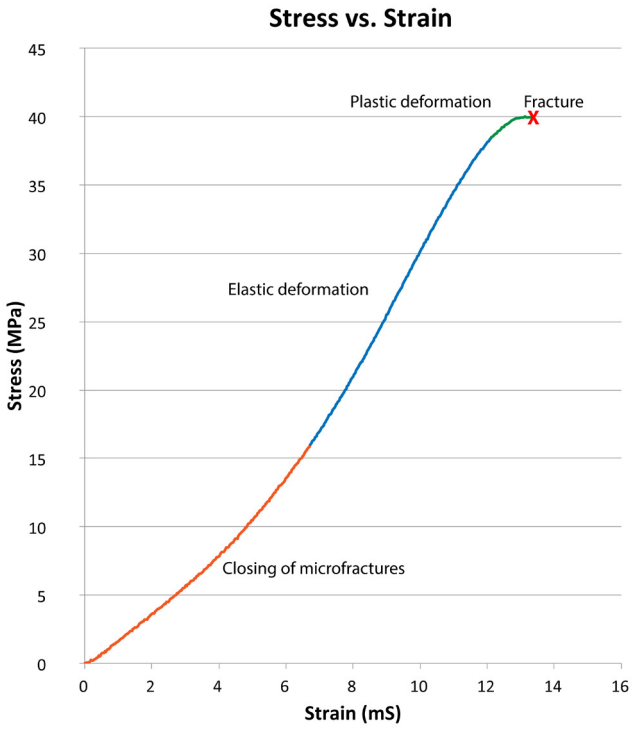

L.4.2.5

Figure 2.5 Specimen L.4.2.5 illustrating a typical stress/strain curve found for the specimens collected at Humbugflats. The three stages of deformation are drawn with different colors and labeled with type of deformation: Red, exponential growth. Blue: linear growth. Green: logistic growth.

The Stress vs. Strain graphs plotted from the data acquired during UCS tests illustrate the relationship between the strain (deformation) and the stress (load) experienced by the specimen during loading. The graph produced can be divided into segments based on the type of deformation experienced by the specimen. The tests conducted on the sample material from Humbugflats typically produce a graph like shown in figure 2.5. The graph can be divided into three segments; exponential growth, linear growth and logistic growth. The first segment of non-linear growth is interpreted to be the result of closure of micro-fractures (Li et al., 1998, Scholz, 1968). During linear growth the specimen is elastically deformed before the curve flattens and the specimen is plastically deformed (Fossen, 2010). This segment is relatively short for these specimens, due to the lack of confining pressure allowing the specimen be deformed under pressure. The third and final segment ends when the peak load is reached and the specimen eventually fails and fractures.

3 Results

This chapter presents the results based in datasets acquired during the fieldwork at the Humbugflats, Utah and lab testing at the NGI. In order to understand the mechanical differences found and controlling factors in distribution of fractures and deformation bands throughout the succession, four layers have been chosen as reference layers.

The layers are chosen based on their respective position in the succession with regards to the proposed bleached deformed sandstone (CO_2 reservoir). Two layers are below the CO_2 reservoir and one above. The layers will be referred to as layer 1, 2, 3 and 4 (L.1, L.2, L.3 and L.4. as shown in figure 3.1).

Figure 3.1 Overview of the northeastern side of the rock sequence at Humbugflats. The reference layers with their position and continuation are shown, with the labels connected to the lower boundary of the respective layer. The blue stippled line indicates the approximate path of the stratigraphic log.

3.1 Stratigraphy of study area

The stratigraphic log from Humbugflats reveals a very homogenous sequence of mostly massive and layered sandstone, shown in fig 3.2, belonging to the Entrada Ss. (Witkind, 1988). There are also a few cross-bedded sandstones and coal layers found in the sequence. One of these cross-bedded sandstones, L.3, stands out from the other sandstones in the rock sequence, as it is saturated with deformation bands (CO_2 reservoir.). Besides being full of deformation bands, it is brightly tan/white in the color opposed to the brown to reddish color common for the rest of the sequence. The succession can be divided into 9 sedimentary facies, as seen in table 3.1.

As seen from the facies distribution, facies A dominates the entire exposed succession with segments of the remaining facies coming inn at different levels (see fig.3.2). The inferred depositional environment for facies A and B is to be that of a fluvial plain with fluvial overbank and levee deposits. Facies E is inferred to be fluvial channels within the fluvial plain, while facies F is inferred to be a dune complex crossing the fluvial plain. O'Sullivan (2010) has referred to this part of Entrada, the earthy facies, as being marine to marginal marine in origin while the slick rock facies of Entrada is more eolian. In order to classify the study area as marginal marine or costal plain a few observations are lacking (e.g. bioturbation and double muddrapes). The stratigraphic log and exposed rock sequence ends with the abrupt transition from the Entrada sandstone to the Curtis formation. This boundary is set at the bottom of a green conglomerate that has eroded into the top of Entrada. This boundary is defined by the J-3 inconformity (O'Sullivan, 2010).

Table 3.1 Description of nine facies A-I based on measured and observed units of the sedimentary exposure at Humbugflats. The facies are listed in order from most dominant to least dominant, and described based on grain size, unit thickness and observed sedimentary structure.

A	**Massive sandstone (F sand):** Massive sandstone without any sign of layering. Sharp depositional contacts with altering thicknesses ranging from 0.1-6m. Variations of red to reddish-brown color.	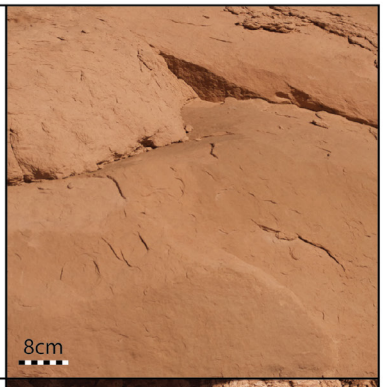
B	**Layered sandstone (Silt-Vf-F sand):** Distinctively layered redish brown sandstone units. Mostly sharp depositional contacts, but erosional contacts are visible at two points. Varying grain size ranging from silt-very fine up to very fine-fine sand. Thicknesses of 0.1-1 m. Typically red to brown in color.	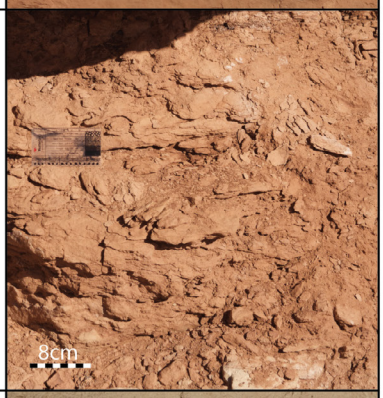
C	**Layered sandstone (F-M sand):** White to pink consolidated layered sandstone with sharp depositional boundaries. Thicknesses ranging from 0.1-1.5m.	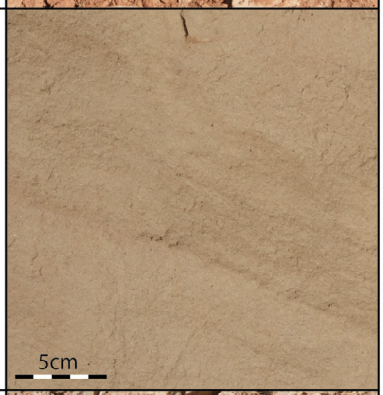
D	**Silt stone (silt-Vf sand):** Gray silt layers with sharp depositional boundaries. Normally thin layers of 5-20cm in thickness. Grain size somewhere between silt and very fine sand**.**	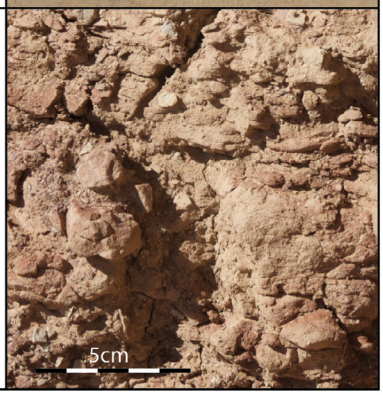

E	**Cross stratified sandstone (M sand):** White to grayish sandstones with visible relatively small cross stratification. Sharp depositional contacts. Thicknesses of 10-30 cm	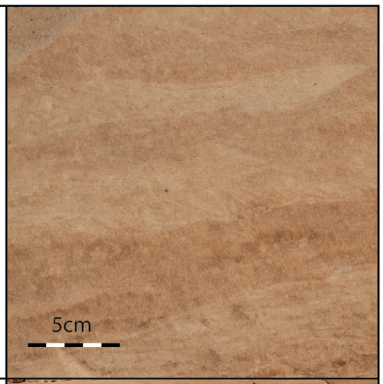
F	**Cross stratified sandstone (M sand):** Tan to white sandstone with large cross stratifications implying that it is dune deposits. Sharp depositional contacts. 2-3m in thickness.	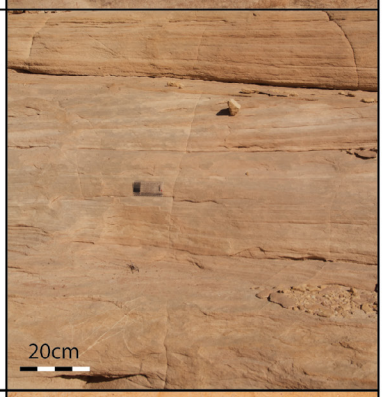
G	**Coal layer:** Black organic layer. Ranging in thickness from 5-30cm. Interlayered with silt.	
H1 H2	**Layered silt stone (silt):** Red layered silt layers with thicknesses of c. 1-5 cm, gradual depositional boundaries. Similar to facies B only finer. **Layered sandstone (F sand):** Gray to white sandstone layers, similar to facies G only thinner. Thicknesses of c. 3-5cm.	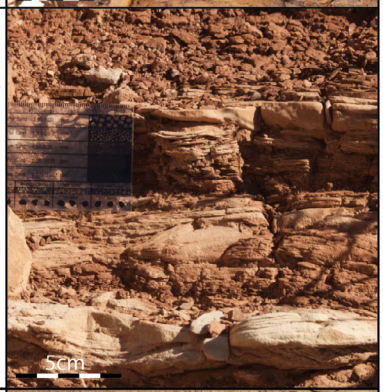
I	**Evaporite layer:** White evaporite layer.	

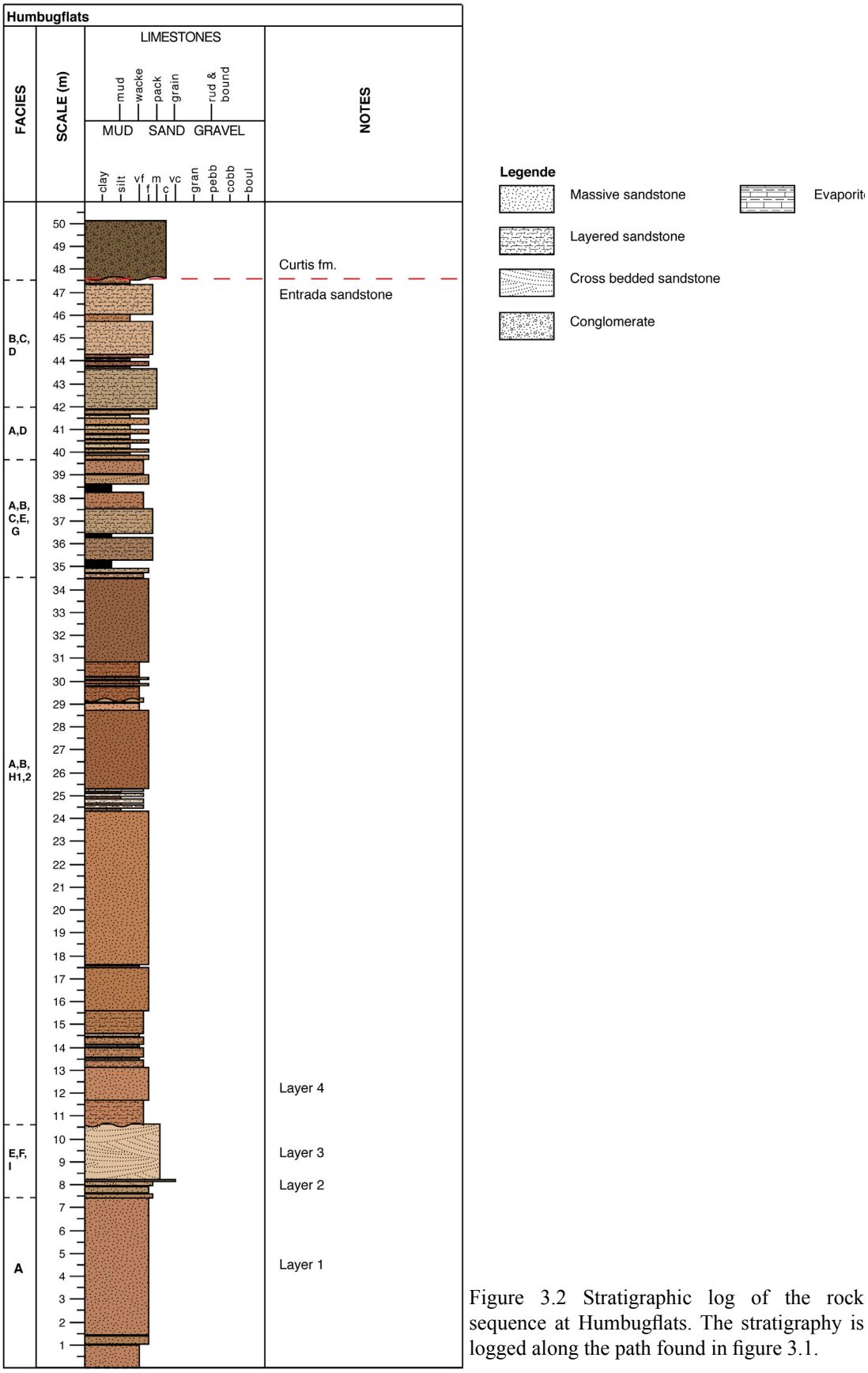

Figure 3.2 Stratigraphic log of the rock sequence at Humbugflats. The stratigraphy is logged along the path found in figure 3.1.

3.2 Mineralogy

Thin sections from the four reference layers have been studied in order to compare the mineralogical composition of the different reference layers.

L.1 and L.4: The studies reveal a quartz dominated composition for all the layers. The observations from layers 1 and 4 confirm that they most likely are of a similar origin. The mineralogical composition is as mentioned dominated by quartz, but smaller amounts of plagioclase, <5%, and carbonate are also seen. Alongside these minerals, veins of iron oxides are found in both thin sections although they are a more prominent feature in layer 1. This is diagnostic feature that separate L.1 and L.4 from L.2 and L.3. Oxides in the form of opaque phases are also present in layer 1 and 4 through out the whole thin section. Besides the more prominent veining found in layer 1, it also has a tighter mineral structure, with less pore space between the grains opposed to layer 4. The porosity calculations for the different layers confirm this; see section 3.2 (Table 3.3, 3.4 and 3.5).

L.2: Layer 2 even more porous than L.1 and L.4, but similarly it can be classified as a quartzite. A more prominent feature is some larger carbonate crystals. The third mineral phase in layer 2 is plagioclase, which is relatively randomly scattered throughout the thin section. Some areas show grain crushing of quartz along curved paths, but further investigation needed to define a mechanism.

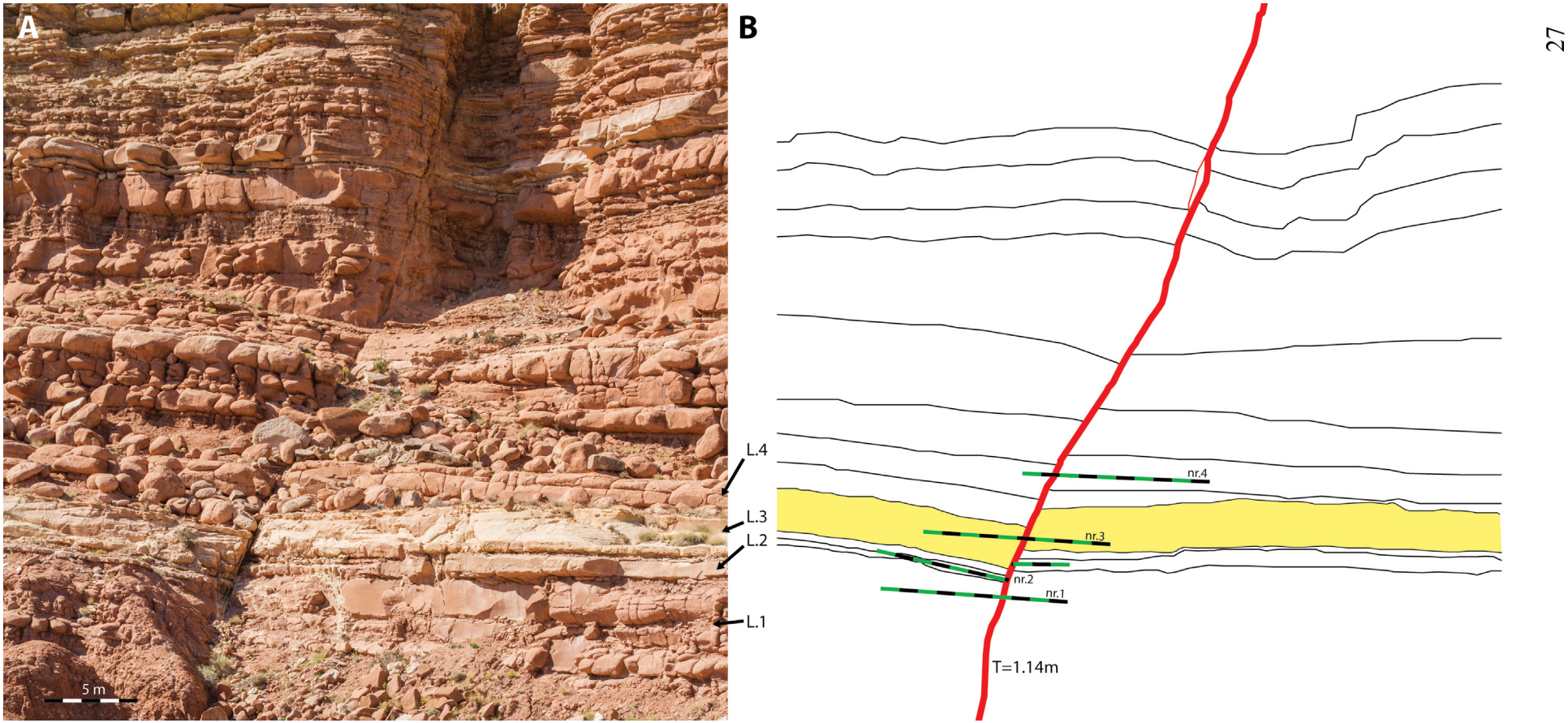

Figure 3.3 (A) Photograph of studied fault in the rock sequence. Interpretation: (B) Sketch of ´A` showing the fault trace in red. The primary bedding surfaces are marked with black lines. The bleached layer 3 is colored in yellow as a marker. Also included are the approximate positions of the scan lines shown as green and black stippled lines. One color segment of the stippled line equals 1m. The horizontal position with regards to the fault is accurate to a meter scale, while the vertical position is chosen based on layering.

3.3 Faults and fractures, Scan line data

3.3.1 Fault description

A number of faults are present in the Humbugflats area, on both sides of the studied rock sequence and within the sequence itself. One of these faults was studied to characterize such structures. The fault was chosen based on its location to the crest of the anticline and in the center of the study area. The fault has a good exposure of both the damage zones and fault core. The fault itself is cutting the entire rock sequence offsetting all the layers, with a throw down to the SW.

Discreet structures

The fault is defined by a fault plane oriented 120/70 suggesting it's a normal fault. The fault core hosts a principle slip surface that has accumulated most of the movement along the fault. This slip surface is exposed towards the hanging wall side. The slip surface is well developed and through-going despite the small throw on the fault. Around 1-1.5m. This coincides with a relatively narrow damage zones, illustrated by the 4 scan lines across the fault. These scan lines show that the fault is accompanied by increased fracturing in the inner 1m (see bellow), making up a tabular strain envelope. Besides the principle slip surface, there are no secondary slip surfaces along the lower part of the fault trace. Further up in the section such a segment is believed to be present, but due to the un-accessible exposure no detailed descriptions could be made.

Membranes

Where the fault cuts layer 3 the fault core is measured and described in more detail. The fault core hosts the mentioned slip surface and a cemented sand gouge. This gouge of the study site is 20 cm thick and continuous along the fault trace for x m before becoming covered by scree.

3.3.2 Fracture distribution recorded by scan lines

The scan lines crossing the fault show a clear trend, where fracture rises from what can be defined as a background level. In order to further constrain the background level of fracturing seven scan lines where in total taken along layer 4, and another five in a second layer above. These scan lines reveal a background level ranging from 0.5 to 1.1 fractures per meter. The average is calculated to be just above 0.7 fractures per meter.

Approaching the fault the fracture frequency rises in all the layers investigated. In layer 4, the fracture frequency peaks at 4 fractures in a meter wide zone on both sides of

the fault. In layer 1, 2 and 3, the fault is affecting a wider area (fig. 3.3). A peak in the fracture frequency can be found for all the layers. Although the background frequency only is established for layer 4, a large variation in the frequency is unlikely based on the similarities found for the layers.

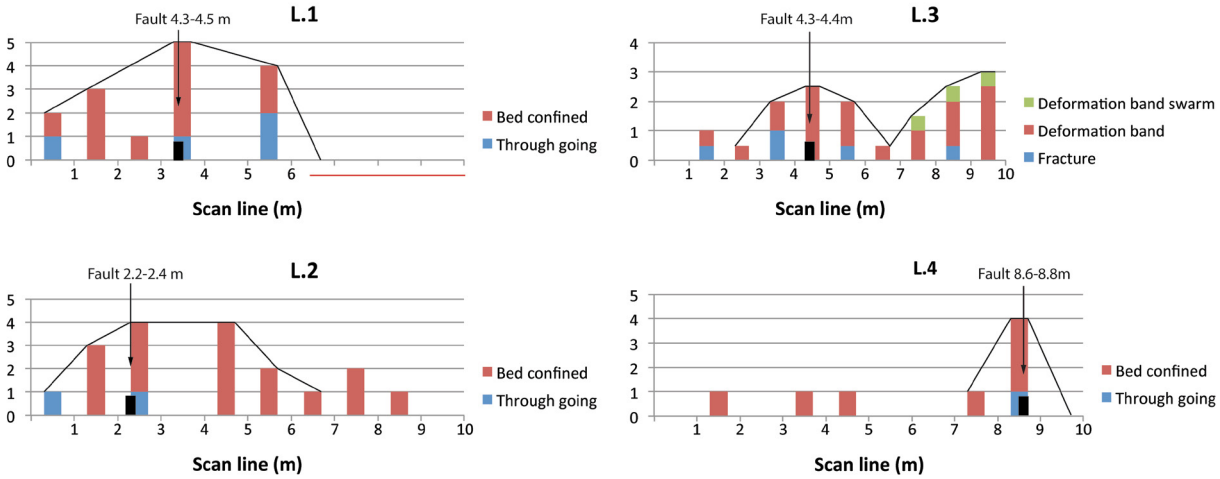

Figure 3.4 Graphic presentation of the scan lines across the fault. The fault is indicated with arrows and numbers indicating the width of the ft. core. The bed-confined fractures, red, are clearly dominating, although the through going fractures, blue, are found through out the scan lines. The general trends found for the different scan lines are indicated with black lines. The scan line completed at L.1 was cut short after 6m because the rest of the scan line/ layer was out of reach.

In L.3 the frequency of deformation bands have been recoded as well as the fractures. A slight peak in deformation bands are found within 3 meters of the fault, but an even higher peak can be found going further out from the fault towards the end of the scan line. The implications of this will be discussed in grater detail below.

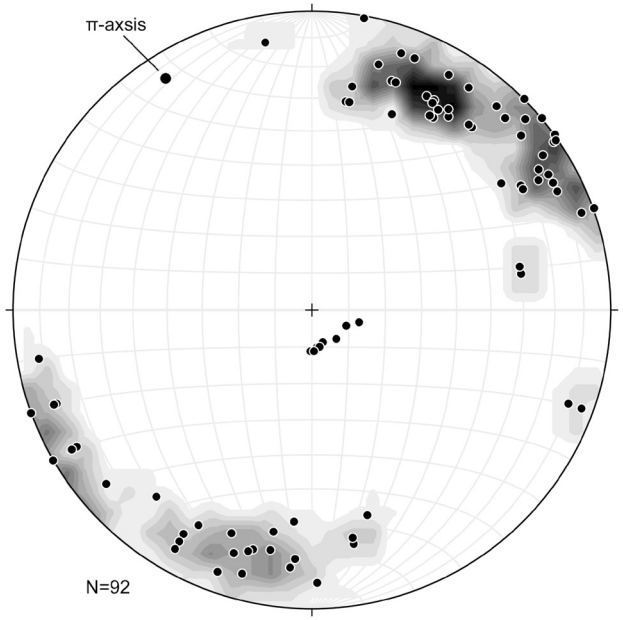

Figure 3.5. Stereo-nett showing two distinctive fracture-planes populations contoured. The bedding of the gentle anticline in the sequence is also included along with the fold axis

Conjugated fractures

The strike/ dip of the fractures recorded in the reference layers outline two populations of conjugate fractures, trending respectively NNW-SSE and WNW-ESE, as seen in Fig 3.5.

3.4 Permeability of ref. layers

To investigate the permeability differences in the rock sequence at Humbugflats, measurements were conducted approximately along the path of the stratigraphic log. Measurements were taken on the reference layers (L.1, L.2, L.3). Measurements were taken in situ with the TinyPerm II (see chapter 2 for facts on instrument and method), and recorded values were used to calculate the permeability.

Table 3.2 Permeability calculations for L.1-L.4. TinyPerm II values from three measurements at each reference layer, with permeability calculated from the median. The tiny perm II measurements were taken directly on the outcrop, removing the outer surface to minimize the effected of erosion. The permeability of L.1 and L.2 has been corrected according to the procedures presented in the methods.

Layer	L.1	L.2	L.3	L.4
Measurements (TinyPerm II value)	13.03	12.06	10.73	12.70
	12.74	12.08	10.77	12.61
	12.92	12.07	10.72	12.67
Median	12.92	12.07	10.73	12.67
Permeability (mD)	0.88	9.54	409.61	1.77
Corrected perm. (mD)	0.58	-	-	1.54

The results show that L.1 and L.4, both have distinctly lower permeability than the other layers, respectively 0.58 mD and 1.54 mD. The increase in permeability from these two layers and up L.2, 9.54 mD, is relatively large compared to the difference between the two. L.3 stands out from the others having a significantly higher permeability of 409.61 mD (see table 3.2).

3.5 Uniaxial compressive strength and Tensile strength from laboratory study

In order to quantify the differences in strength throughout the sequence, samples collected in the field have been tested for uniaxial compressive strength and indirect tensile strength in the laboratory (See methods in section 2.3.2 and 2.3.3). In order to have a representative dataset, 82 drilled out specimens were tested. In total 11 uniaxial compressive strength test and 71 brazilian tests were conducted. Tensile fractures are overrepresented in the field area with respect to shear fractures. Because of this observation in the field, samples for brazilian testing were prioritized during sample preparation, due to the relatively limited amount of material.

3.5.1 Uniaxial compressive strength

The uniaxial compressive strength is calculated from the maximum load at the time of failure related to the cross sectional area. The acquisition of the peak load is described and illustrated in the methods, see section 2.3.6. For each individual layer the sample specimens display a similar development and build up of strain. The individual differences between specimens typically manifest as how fast strain is built uplinked to the time it takes to reach failure. Individual findings in each layer will be presented in separate sections. Due to the lack of sufficient material from L.2, UCS tests were conducted on this layer.

Table 3.3 Description and characteristics of the specimens used to test the uniaxial compressive strength. The table includes the mass, height and diameter of the specimens along with a short description of the state the specimen was at the time of testing. Layering is perpendicular to the long axis of the specimens.

Layer	Sample ID	Dry mass	Height	Diameter	Description	Picture
		g	*mm*	*mm*		
1	L.1.1.1	67.74	56.35	25.04	The specimen is intact, without any damage to the surface. No fractures visible.	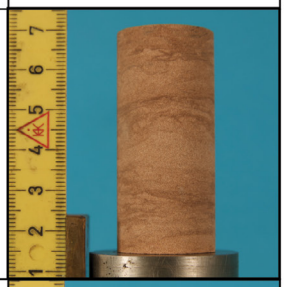
1	L.1.1.2	65.73	56.37	25.05	A large pice of the specimen has been chipped of during the preparation.	
1	L.1.1.3	67.77	56.36	25.03	Intact specimen without external damage or visible weaknesses.	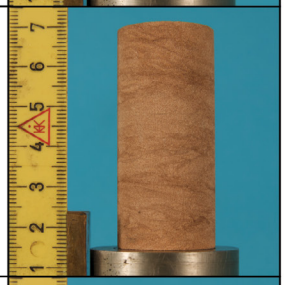
1	L.1.1.4	67.99	56.36	25.03	Intact specimen without external damage or visible weaknesses.	
3	L.3.1.1	50.75	55.53	24.50	The specimen is drilled perpendicular to layering reveling weaknesses along the layering. The specimen is able to withstand little to no force parallel to layering without breaking. Somewhat more resilient perpendicular to layering.	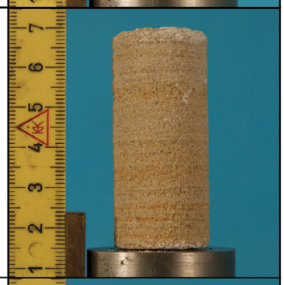
3	L.3.1.3	50.31	54.98	24.59	Same as above.	

Layer	Sample ID	Dry mass	Height	Diameter	Description	Picture
		g	*mm*	*mm*		
4	L.4.1.1	60.94	54.29	25.02	A more massive sandstone making it difficult to determine the direction of layering. A pre exciting weakness in the form of a fracture is visible in the specimen parallel to the long axis of the specimen.	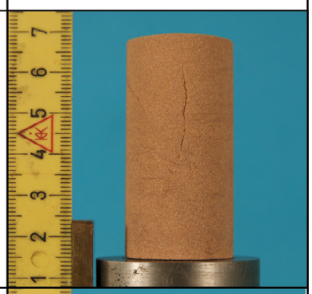
4	L.4.1.2	60.10	54.32	25.03	The specimen has been chipped during prepara-tion. The damaged part of the specimen will in theory not effect the test because of its placement within the specimen relative to the direction to the applied load.	
4	L.4.1.3	61.47	54.33	25.03	Intact specimen without external damage or visible weaknesses.	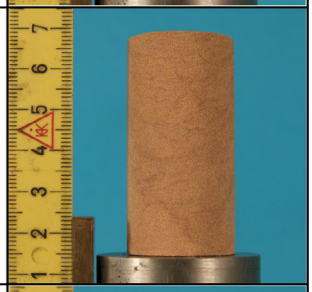
4	L.4.1.4	60.23	54.30	24.99	Intact specimen without external damage or visible weaknesses.	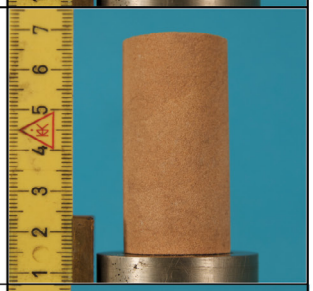
3	L.4.1.5	60.21	54.30	25.00	Intact specimen without external damage or visible weaknesses.	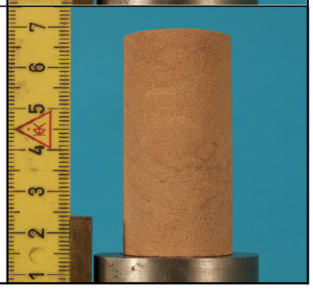

Aspects of tests of specimens

The selection of specimens shows only insignificant differences in height and diameter, making them ideal to compare. The dimensions of all the specimens originating from layer one lay within a standard deviation of +/- 0.01 mm, for both the height and diameter. The accuracy achieved preparing these specimens add confidence to the results they produce. One noticeable deviation in the sample material is from L.1. Specimen L.1.1.2 is almost 2 grams lighter then the other samples that gives a standard deviation of +/- 0.92. The reason for this is simply that a part of the sample has chipped of during the preparation of the sample. Although this appears to be a weakness, it should in theory not affect the results because the chipped surface is not where the load is applied.

The physical differences between the specimens created from L.3 (L.3.1.1 and L.3.1.3) are evident looking at the measurements acquired. The largest difference is in the height, which is not taken into consideration when calculating the uniaxial compressive strength. Nevertheless the difference in both weight and height can be used to explain the different responses observed when loading the two specimens.

Specimens prepared from L.4 this is to a large extent similar to those from L.1. A standard deviation of +/- 0.02 for the diameter and +/- 0.01 for the height illustrates this. The largest differences between the specimens are found for the weight of each sample, with differences exceeding 1 gram.

L.1 and L.4

Results form the four specimens tested from L.1 are shown in fig. 3.6 A and B. In the first 100 seconds of the load vs. time graph the specimens all have approximately the same slope, after this point the curves split into two groups (Fig 3.6 A), reflecting the stiffness of the material. Specimen L.1.1.2 and L.1.1.4 are stiffer than the L.1.1.1 and L.1.1.3. The difference between the two groups is also evident in the stress vs. strain graph (fig 3.6 B). The uniaxial compressive strength of L.4 is determined by analysis of five specimens. The figure is only based upon four specimens, because specimen L.4.1.4 experienced difficulties. The remaining specimens show a development in the stress vs. strain graph similar to those found for L.1.

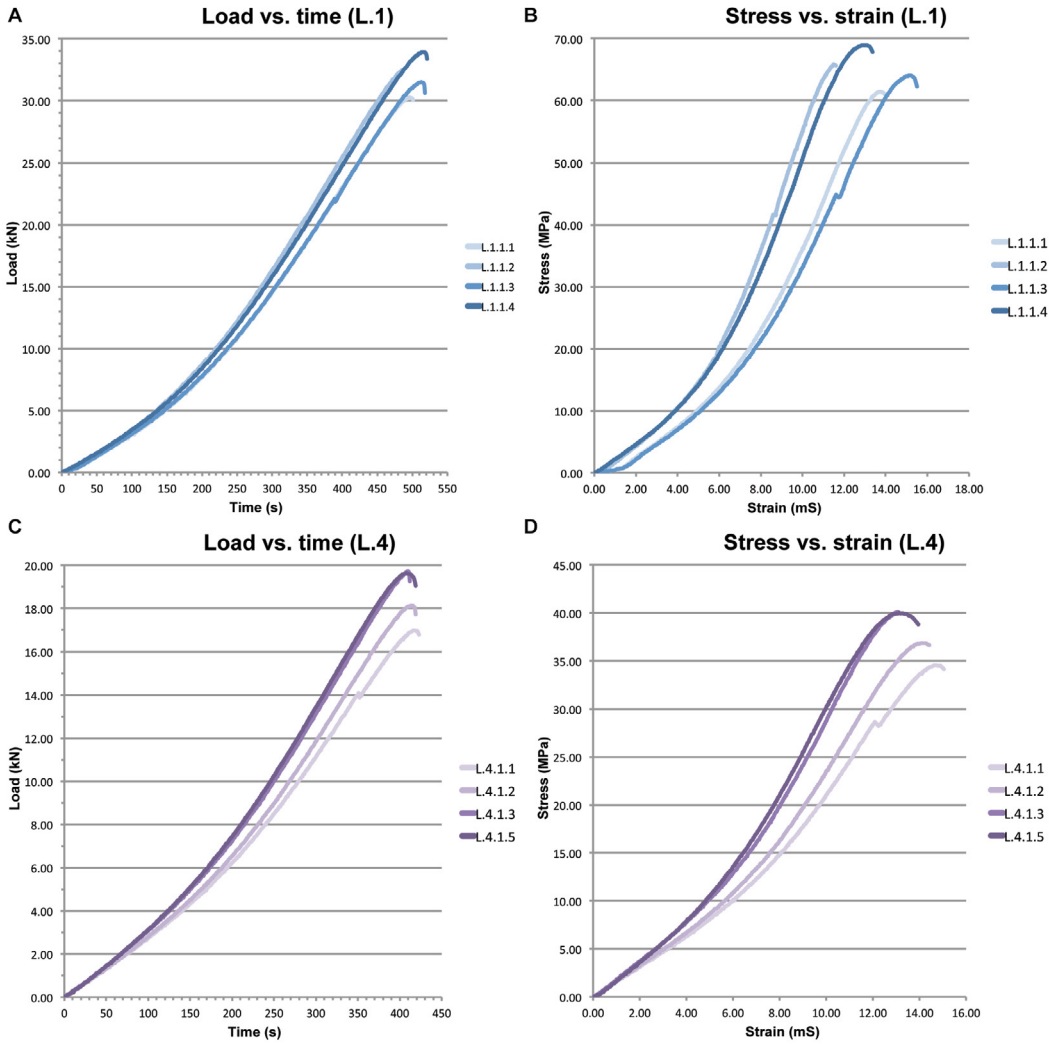

Figure 3.6 A: Load vs. time graph for specimens from L.1 (L.1.1.1-L.1.1.4). Each curve represents the recorded load attained during laboratory testing of the specimens. B: Stress vs. strain graph of calculated stress and strain for L.1.C: Load vs. time graph for L.4. Based on the modified output values attained during testing. D: Stress vs. strain graph of calculated stress and strain.

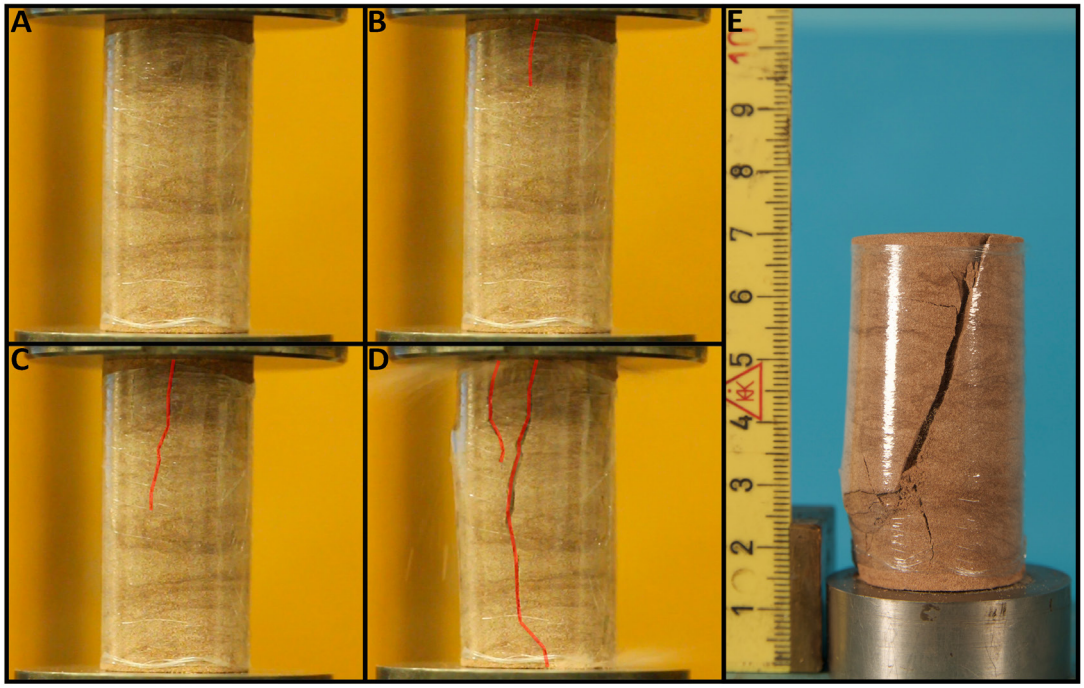

Figure 3.7. Evolution of a fracture in specimen L.1.1.3, with the fracture outlined in red. A) pre-failure: Intact specimen before the peak load is reached. B) Fracture stage 1: the fracture starts to develop in the top part of the specimen. C) Fracture stage 2: a continued growth. D) Final stage of fracturing: a through going fracture has developed. E) Post-fracture. Photo taken of the specimen here turned around 180° to show a typical shear fracture.

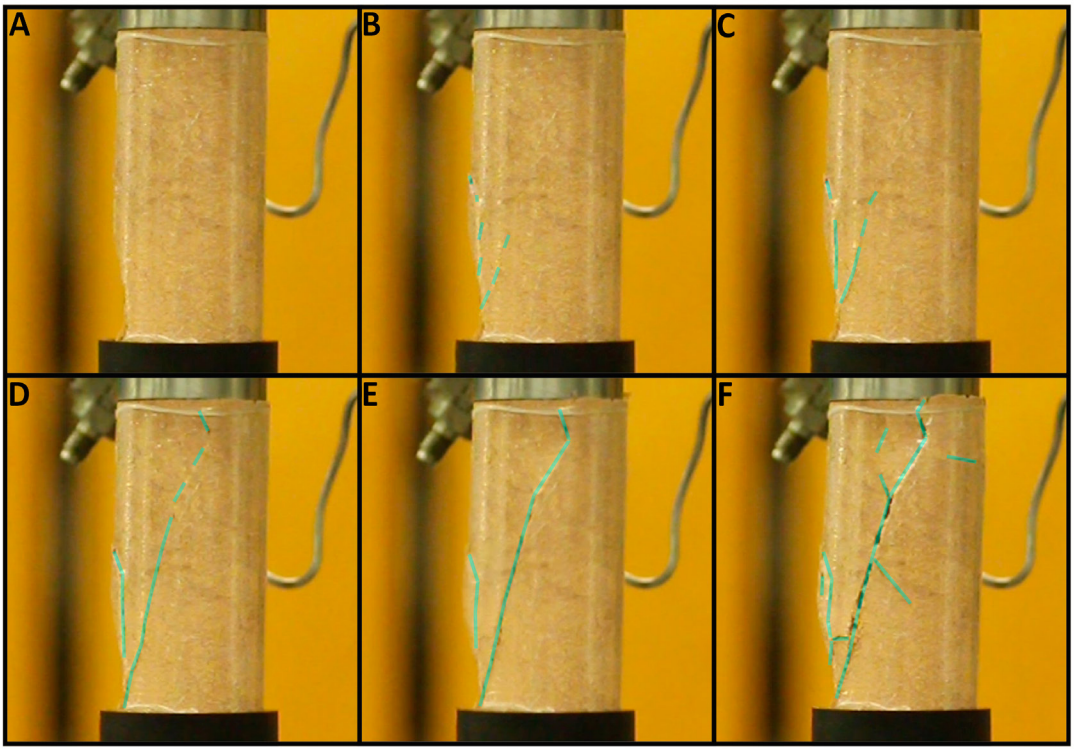

Figure 3.8 The development of a shear fracture in specimen L.4.1.2 in six phases. A: Pre fracture, unaffected specimen before failure. B: Stage 1, the fracture is established at the bottom of the specimen. C and D: Stage 2, growth of the fracture. E: Stage 3, movement along the principle slip surface. F: final stage/ post fracture: shear fracture. The fracture is marked with a mint green colored line.

The individual curves in figure 3.6 can be divided into three segments (see methods). First a non-linear segment, which for the two groups from L.1, respectively, lasts until 2-4 mS, before a more linear curve appear. The first group, L.1.1.2 and L.1.1.4, has a parallel development until a strain of approximately 6 mS is reached, marking the end of the non-linear growth. L.1.1.4 continues in a relatively similar manner until the relatively linear growth ends, at this point the curve starts flattening. L.1.1.2 exhibits a slight release of stress, at the point where the L.1.1.4 and L.1.1.2 curves separate, at 6 mS. L.1.1.2 then shows yet another slight release of stress (c.42MPa, 8mS). Both these "events" are most likely a result of closure of pre existing weaknesses within the specimen. The growth of the L.1.1.2 curve continues until the curve starts to flatten, this section of the curve is significantly shorter for this specimen than for the other three. Like L.1 the specimens tested from L.4 can be placed in two groups after a similar development in the beginning. Within the first group, L.4.1.3 and L.4.1.5, the development of stress and strain is almost identical, separating them is the momentarily failure after the critical stress is reached for L.4.1.3. This creates a peak in the graph, rather than a curved failure, like seen for L.4.1.5.

Figure 3.9 Conjugated fractures developed in specimen L.4.1.1. The fractures are outlined in green and number after temporal occurrence.

The second grouping of L.1, consisting of L.1.1.1 and L.1.1.3 develops in a similar style, accumulating load at lower rate than the first group, indicating a slower buildup of stress/strain. The build up of strain is identical for the two specimens until a strain of c. 3 mS is reached. L.1.1.1 continues with the steepest slope of the two, having a slightly higher stiffness. L.1.1.3 has a gentler slope, although it accumulates the highest amount of stress. The slopes of the two groups differ only with ca. 1kN after they depart form each other at around 100 seconds. The second group from L.4, L.4.1.1 and L.4.1.2, have combined a gentler slope than the first group although the difference between their respective curves is only slightly smaller then the difference between the two groups. Like L.1.1.2 and L.1.1.3, L.4.1.1 has a release of stress during the accumulation of strain. L.4.1.2 has a more similar development as the two specimens, L.4.1.3 and L.4.1.5, found in the first group even though the specimen has a lower stiffness (young's modulus).

Table 3.4 Table showing the results from the uniaxial compressive strength tests of specimens from layer 1 and layer 4. The calculated porosity of the specimens is also included.

Sample ID	**Volume**	**Density**	**Porosity**	**Peak load**	σ_s	Υ	**Young´s modulus**	**Time to fracture**
	cm^3	*g/cm^3*	*%*	*kN*	*MPa*	*mS*	*E*	*MM:SS*
L.1.1.1	27.74	2.44	7.83	30.26	61.45	13.77	4.46	08:16
L.1.1.2	27.77	2.37	10.67	32.44	65.82	11.49	5.73	08:03
L.1.1.3	27.71	2.45	7.72	31.53	64.07	15.15	4.23	08:32
L.1.1.4	27.72	2.45	7.44	33.94	68.98	12.82	5.38	08:33
L.4.1.1	26.68	2.28	13.80	16.99	34.55	14.69	2.35	06:56
L.4.1.2	26.71	2.25	15.11	18.14	36.86	14.21	2.59	06:52
L.4.1.3	26.72	2.30	13.19	19.74	40.11	13.07	3.07	06:49
L.4.1.5	26.64	2.26	14.71	19.63	39.99	13.12	3.05	06:47

Table 3.4 includes results calculated from the physical properties of the sample material and results calculated from the analyzed data points recorded during laboratory testing of the material. Of most inters is the uniaxial compressive strength and the porosity, which will be compared with the other results. The data obtained form the specimens are used to calculate the uniaxial compressive strength, σ_s, and the axial strain, γ, the results of these calculations are used to say something about the strength of the layer as a whole.

The average UCS of L.1, i.e the stress, 65.08 MPa +/- 3.15, is ascribed to the L.1 as a whole. The average UCS for L.4 is calculated to 38.31 MPa. This average strength lies below the majority of the compressive strength for each individual specimen due to the low peak load recorder for L.4.1.1. The spread in results from L.1 and L.4 are quite large compered to L.3 (see bellow). The results also revels that the three last specimens have

very consistent, both in measurements and results. The porosity calculations reveal very consistent results, with one exception. The high porosity found for L.1.1.2 is a result of the specimens damaged surface, see table 3.2. This affect the density calculated from a perfectly cylindrical. If L.1.1.2 is disregarded and the reaming calculations are used to find an average porosity for L.1 as a whole, the result is a porosity of 7.7%. For the specimens from L.4 the porosity calculations are slightly higher, with an average porosity of 13.8 %. These results are consistent with the observations conducted with the microscope (see section 3.1.1).

Fig. 3.7 and Fig 3.8. display they typical development of a shear fracture in L.1 and L.4 The initial fracture nucleates and then propagates from the top (fig 3.7), or the bottom (Fig. 3.8) of the specimen, developing into a larger fracture with an angle to $\sigma 1$. The main fracture continues to propagate into the middle part of the specimen. At this point the fracture is still in the opening mode

In other specimens several fractures develop, into conjugated fractures as load is still applied. An example of this is found in specimen L.4.1.1 (fig. 3.9), where a shear fracture forms first. Then a conjugated shear fracture develops as a second fracture.

Layer 3

Layer 3 stands out from the other layers investigated with respect to the amount of load it is able to accumulate before failure. This is clearly illustrated in figure 3.8. The load sustained by the specimens is only around 1 kN. Only two specimens, L.3.1.1 and L.3.1.3 were tested to investigate the uniaxial compressive strength of layer 1. The database used to create the two curves show that it is difficult to ensure an even loading at small loads. The curves are both generally uneven, although the trend is relatively clear.

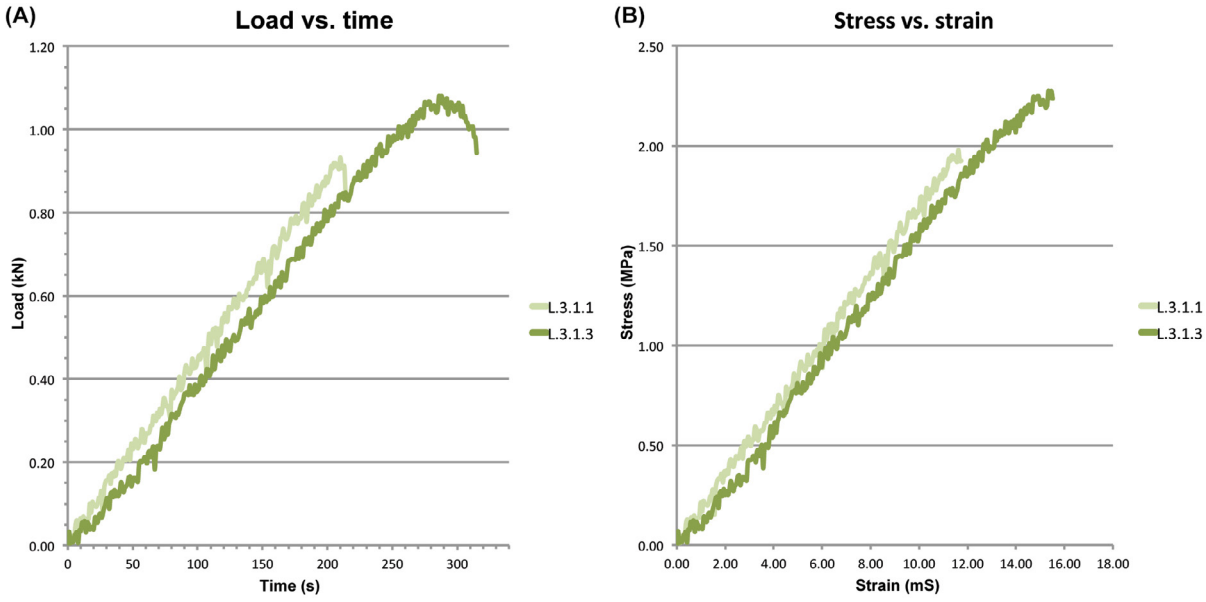

Figure 3.10 Load vs. time graph for Layer 3. The graph is based upon results obtained during lab testing of specimen L.3.1.1 and L.3.1.3, in their respective colors green and red. The sample material was so week that it was difficult to prepare enough sample material. This became obvious when testing the material as well. The rough curves can be a result of static noise from the instrument or simply a lot of small weakness in the specimen, such as low cohesion between the sand grains. Low cohesion can cause grains to roll/ collapse creating the small insignificant drops in sustained load.

Besides the relatively large difference in the time relapsed before failure, the stress vs. strain graph reveals almost identical stiffness for both specimens. The graph as a whole shows that layer 3 as a whole can withstand a load of around 1.1 kN. These two peak loads for L.3 are so low that they are comparable to load measurements investigating indirect tensile strength rather than uniaxial compressive strength. Further elaboration on this will come in the next paragraph.

Although the two specimens are relatively different the data produce relatively similar results, both the specimens are within +/-0.13 kN form each others peak load (table 3.5) verifying that a good uniaxial compressive strength of the material is found. As

shown in fig 3.11, the created fracture is not a typical shear fracture, but rather a tensile fracture. If this is correct it demonstrates that the material is to week to create a shear fracture without being confined. The average calculated compressive strength is 2.12 MPa, which is way bellow what could be expected as a uniaxial compressive strength. This low result is an indication of a material that only will produce tensile fractures.

The Porosity of L.3 is found to be almost 30%, which can be a factor controlling the low strength found for the layer. This conforms with the high permeability presented in table 3.1.

Table 3.5 Table of uniaxial compressive strength and porosity of L.3.

Sample ID	**Volume**	**Density**	**Porosity**	**Peak load**	σ_s	Υ	**Young´s modulus**	**Time to fracture**
	cm^3	*g/cm^3*	*%*	*kN*	*MPa*	*mS*	*E*	*MM:SS*
L.3.1.1	26.17	1.94	26.81	0.93	1.98	11.62	0.17	03:30
L.3.1.3	26.10	1.93	27.25	1.08	2.27	15.34	0.15	04:45

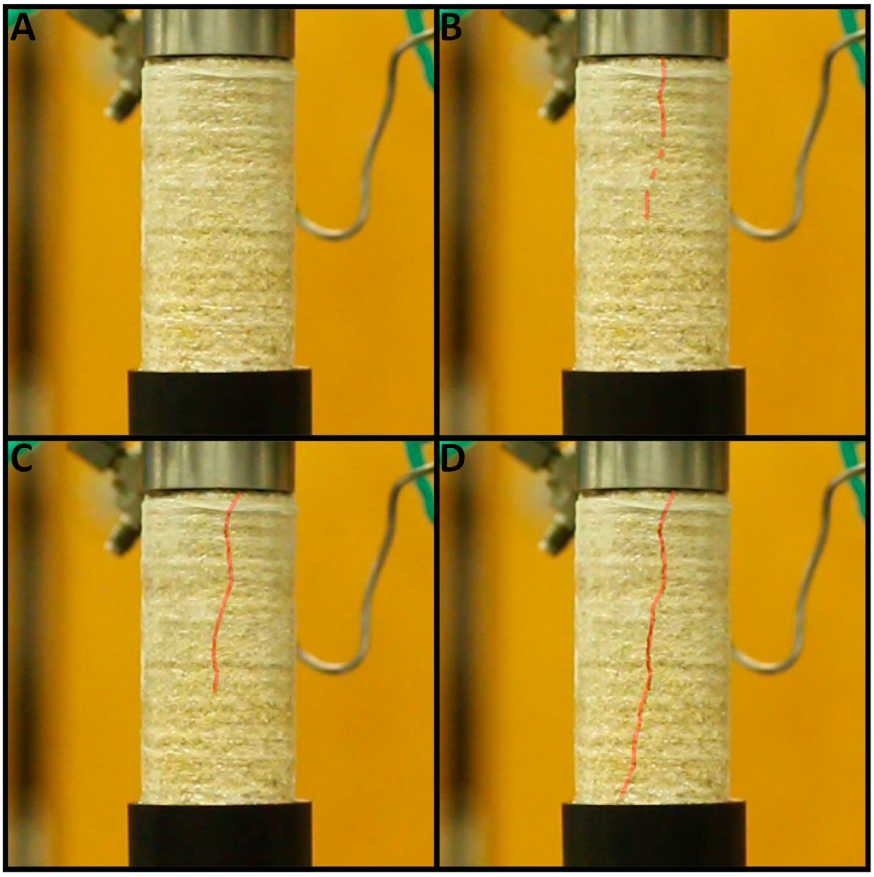

Figure 3.11. The development of a fracture in L.3.1.1.The fracture is marked with a red line. A: pre failure, intact specimen unaffected by the applied load. B: Stage 1, a fracture is established in the upper part of the specimen. C: Stage two, the fracture propagates downwards in the specimen as the fracture is expanding. D: Stage three/final stage, the fully developed fracture continues to expand as load is applied.

3.5.2 Tensile strength

In order to quantify the tensile strength of the reference layers, the indirect tensile strength is calculated from data attained during brazilian tests. Determination of the indirect tensile strength of each layer is based on 71 specimens representing the reference layers, L.1, L.2, L.3 and L.4. In order to get an overview and a good understanding of the results, a selection of tests from each layer will be presented in the graphs in following paragraphs. Note that a complete overveiw of the samples tested can be found in appendice 1.

Layer 1

The tensile strength of L.1 is based on the results of nine brazilian tests. Three specimens of the same cylinder, L.1.2.3 (A,B and C), all follow a similar trajectory before reaching critical loads at 1.24 kN and 1.31 kN (fig.3.12), illustrating a typical trend found for all the layers. The specimens produced from the same cylinder normally produce similar results, as the differences within the cylinder are so small. The accumulation of strain in specimen L.1.2.2C is relatively similar to three specimens from L.1.2.3. Contrary to these, L.1.2.2C is able to withstand a higher load i.e. higher strain before the failure occurs. The critical load reached is significantly higher than for the three

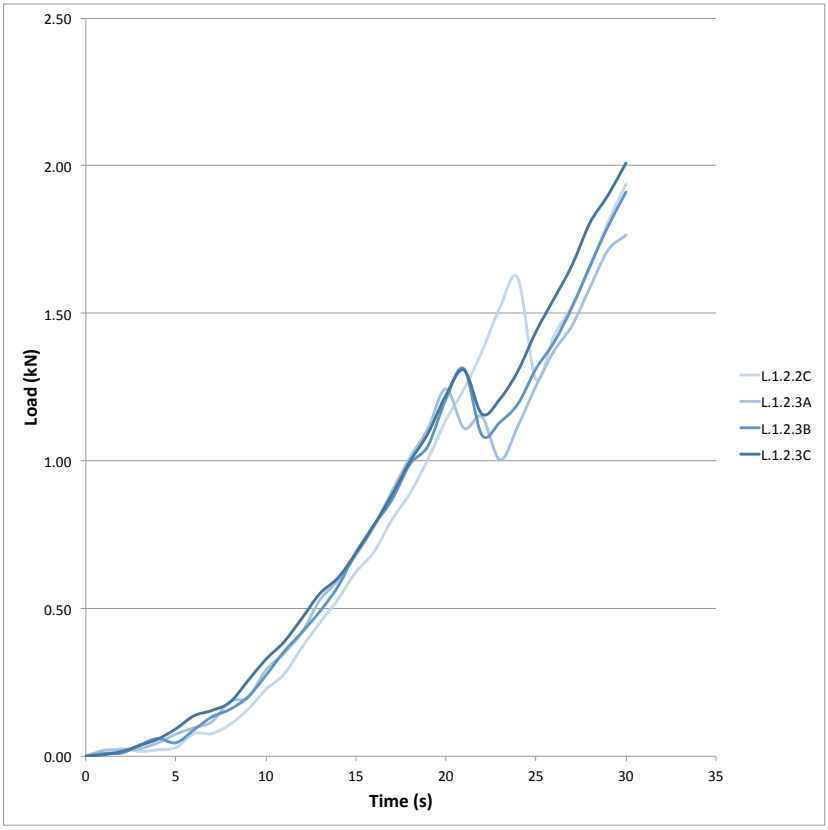

Figure 3.12. Load vs. Time graph for L.1, based on brazilian test conducted on four specimens. The selected four specimens represent the population as a whole, chosen based on the results they produced and their properties to ensure a good basis for comparison.

other specimens.

The graph show that the data used to establish the curves are relatively consistent and their main differences lay in the recorded critical load. All the curves show a relatively similar growth and timing of failure within a given time-load region, however, the spread in recorded peak load for the specimens result in a relative large spread in the results.

Table 3.6. Calculated indirect tensile strength for layer one. The gray rows are indicating which specimens were used as examples in figure 3.14

Sample ID	**Density**	**Porosity**	**Critical Load**	**σ_t**	**Time to fracture**
	g/cm^3	%	*kN*	*MPa*	*s*
L.1.2.2A	2.42	8.7	1.10	2.21	32
L.1.2.2B	2.43	8.4	1.68	3.38	30
L.1.2.2C	2.44	7.8	1.62	3.26	24
L.1.2.2D	2.42	8.7	1.49	3.00	20
L.1.2.3A	2.41	9.1	1.24	2.50	20
L.1.2.3B	2.42	8.6	1.31	2.63	21
L.1.2.3C	2.43	8.3	1.31	2.64	21
L.1.2.3D	2.42	8.7	1.17	2.34	19
L.1.2.3E	2.41	9.1	0.84	1.68	18
Average	2.42	8.6	1.32	2.66	23

The results show a relatively large spread in the calculated tensile strength. The total average strength of the layer is calculated to be 2.66 +/- 0.50 Mpa. The results show a relatively large spread in the results compared to the other layers (see below). Nevertheless these differences are not believed to be significant in a broader sense. The

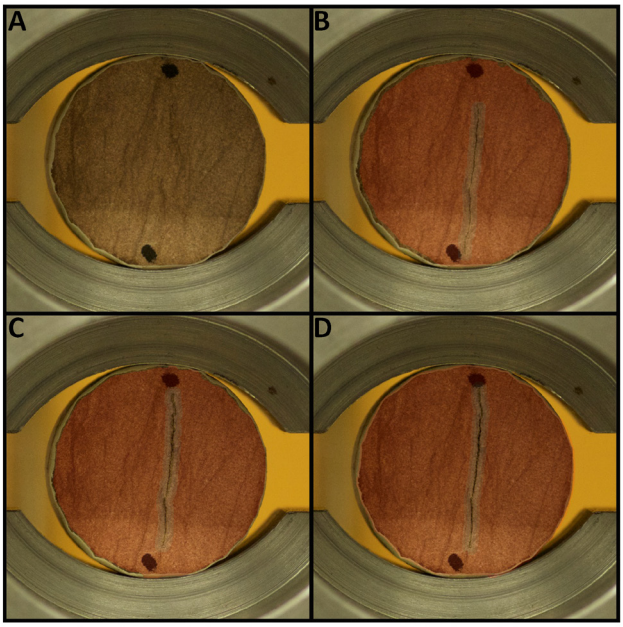

Figure 3.13 The development of a tensile fracture in specimen L.1.2.3C. The fracture is highlighted with a surrounding “see through” red color. The fracturing is divided into three stages. A: Pre fracture, B: The fracture is formed in the center of the specimen, from this point the fracture propagates along the load axsis (see methods). C: growth and expansion, the fracture still propagating towards the top and bottom of the specimen. D: Expansion until another fracture takes over.

timing of failure also points towards a homogeneous population. With exception of the first specimen and the last, L.1.2.2A and L.1.2.3E, the specimens that originate from the same cylinder have a smaller standard deviation than the population as a whole.

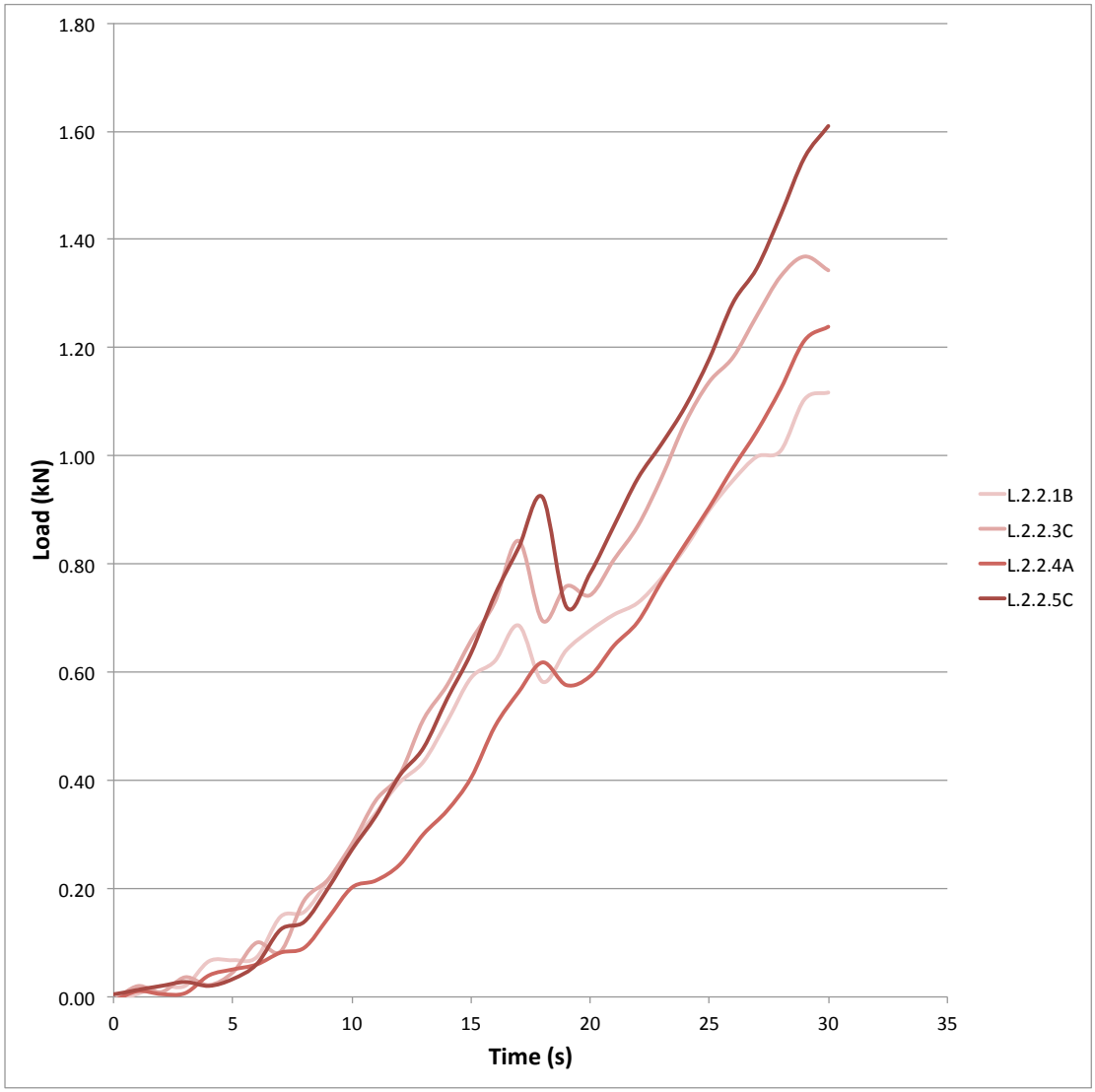

Figure 3.14 Load vs. Time graph for layer 2, based on the data collected during testing of Specimens L.2.2.1B, L.2.2.3C, L.2.2.4A and L.2.2.5C are used as examples of the typical development found in these data and makes up the basis for the load versus time graph.

Layer 2

In total 17 brazilian tests where preformed on specimens from L.2. The results are showing layer consistent measurements, giving confidence to the produced results.

The data presented in fig. 3.14 reveals that the specimens can be placed in two populations. Specimen L.2.2.3C and L.2.2.5C both reach a significantly higher peak load than the other two. The specimens have relatively uneven curves, pointing towards an irregular accumulation of strain. Before a load of 0.2kN is reached the measurements

Table 3.7. Calculated indirect tensile strength for layer two, key measurements and timing of failure. The gray rows are indicating which specimens that were used as examples in figure 3.16.

Sample ID	**Density**	**Porosity**	**Critical Load**	**σ_t**	**Time to fracture**
	g/cm^3	%	*kN*	*MPa*	*s*
L.2.2.1A	2.21	16.7	0.59	1.20	14
L.2.2.1B	2.19	17.2	0.69	1.39	17
L.2.2.1C	2.17	17.9	0.54	1.10	16
L.2.2.1D	2.16	18.6	0.51	1.02	16
L.2.2.2A	2.10	20.9	0.63	1.28	23
L.2.2.2B	2.13	19.4	0.40	0.82	13
L.2.2.2C	2.16	18.6	0.55	1.10	15
L.2.2.3A	2.20	16.9	0.50	1.01	12
L.2.2.3B	2.23	15.7	0.74	1.50	15
L.2.2.3C	2.22	16.3	0.84	1.69	17
L.2.2.4A	2.11	20.2	0.62	1.27	18
L.2.2.4B	2.12	19.8	0.50	1.02	14
L.2.2.4C	2.11	20.2	0.48	0.98	14
L.2.2.5A	2.18	17.6	0.62	1.26	19
L.2.2.5B	2.22	16.3	0.81	1.65	14
L.2.2.5C	2.21	16.7	0.92	1.87	18
L.2.2.5D	2.09	21.0	0.40	0.80	16
Average	2.17	18.2	0.61	1.23	16

are to a large extend affected by the lack of direct contact with the specimen and static noise produced by the instrument. L.2.2.5C accumulate strain at a relatively constant rate during after loading after the 0.2 kN. Specimen L.2.2.1B and L.2.2.4A show an uneven accumulation of strain before it is released.

The last specimens prepared from each cylinder have a significantly different thickness than the other specimens from the same cylinder. Because the thickness is included in the calculations (see methods) this should not affect the calculated strain (Table 3.7).

The average tensile strength for layer two is calculated to be 1.23 +/- 0.30 Mpa. The relatively large spread in the results, underlined by the standard deviation cannot be explained by the irregularities found in the specimen dimensions. The calculated tensile strength for both L.2.2.1D and L.2.2.2C is within what can be regarded as the normal range in the results, and the thickness of these two specimens are around 12.70mm, which is in the high end of measured thicknesses. The specimen that has the highest tensile strength, L.2.2.5C, is not irregular in any way. Based on these observations the spread in the results must be a result of internal differences in the specimens or small irregularities on the surface where load is aplied.

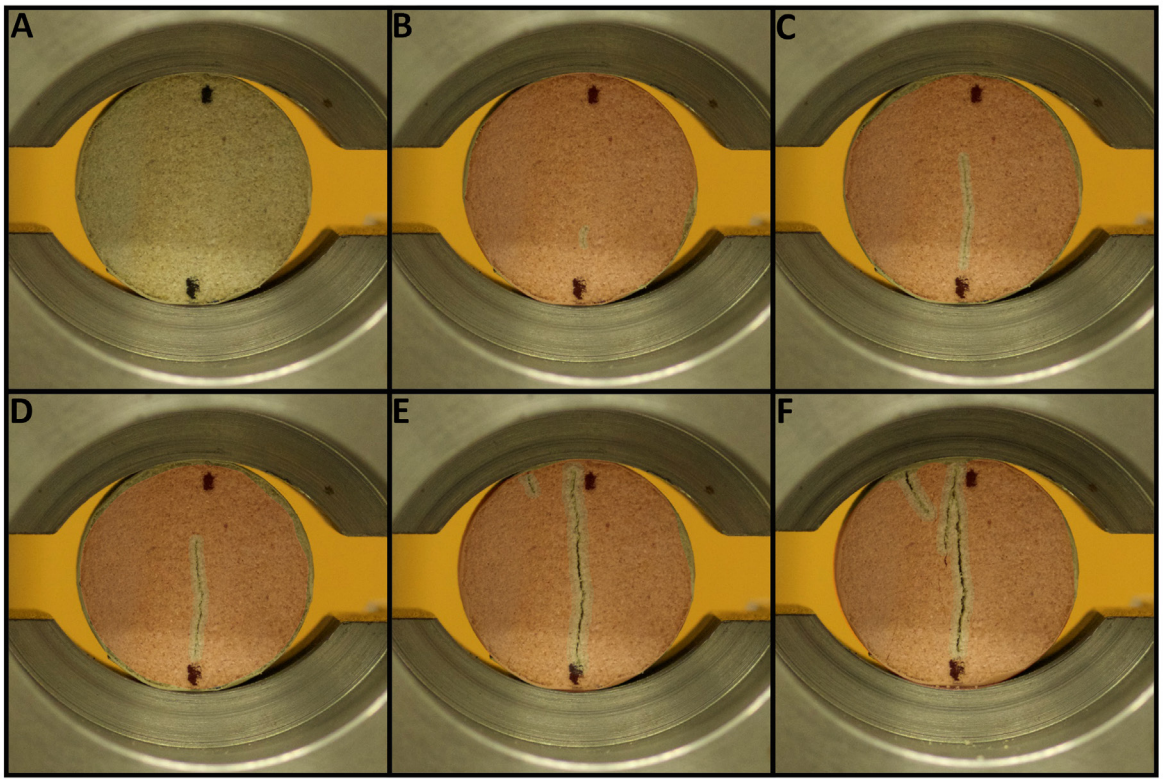

Figure 3.15. Specimen L.2.2.5C is used to illustrate a typical extension fracture and its development. An extensional fractures development through 6 phases. The fracture is highlighted with surrounding see trough colors in shades of red. A: pre fracture, an intact specimen during loading before the critical load is reached. B: Stage 1, the fracture is established in lower end of the specimen after the critical load is reached. C and D: stage 2, a continued growth an opening of the fracture. The fracture grows upwards and expands at the same time. The fracture continues to propagate along one axis. E: stage 3, the fracture has now established itself through the sample. The fracture is at this point only opening perpendicular to the fracture. F: final stage: as the fracture opens smaller fractures start developing as the specimen is continually being deformed.

Layer 3

The calculated tensile strength of L.3 is based on analysis of 26 brazilian tests conducted on specimens prepared from the sample material. The data recorded revealed low peak values throughout the dataset. The relatively small amount of strain the specimens were able to withstand resulted in irregular curves. Resulting from the combination of week specimens and static noise produced by instrument registered at low loads. The peak values of the specimens are relatively consistent. The difference between the highest and lowest peak load is only on the order of +/- 0.09 kN.

In order to describe the trend of the irregular curves and enhance the peaks, a running average was calculated for each specimen with an N=5 value (fig. 3.17). Displaying the overall trend of the specimens in a more efficient and visible way. The calculated running average only serves as aid in order to interpret the graph and the data collected during testing, while the peak value used to calculate the tensile strength recorded from the original data.

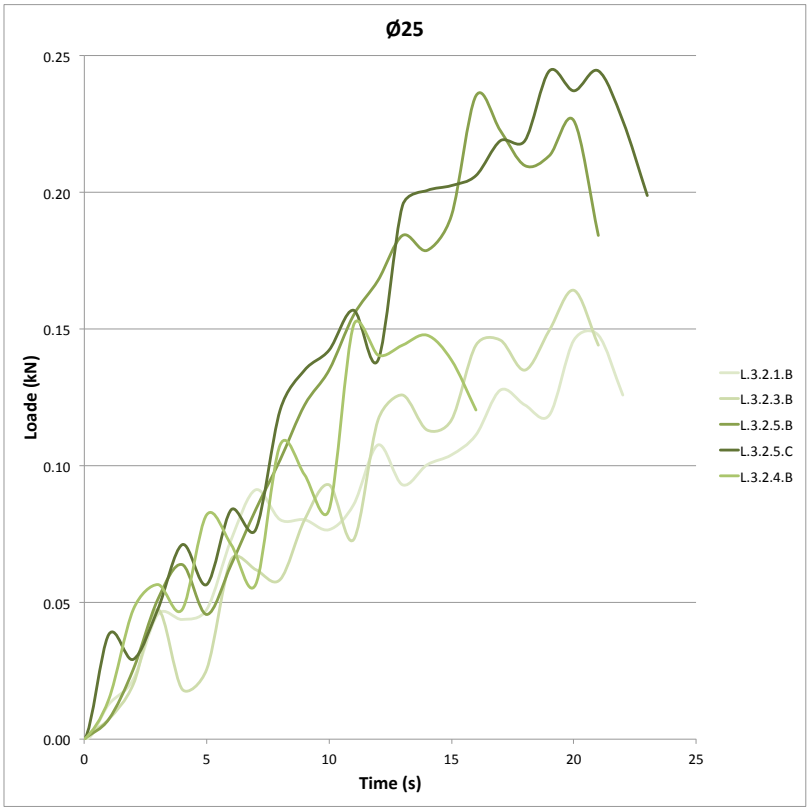

Figure 3.16. Load vs. Time graph for layer 1. The curve is based on the data collected from testing of, specimen L.3.2.1B, -L.3.2.3B, -L.3.2.4.B, -L.3.2.5B and –L.3.2.5C. These specimens are prepared with an ideal diameter of 25mm.

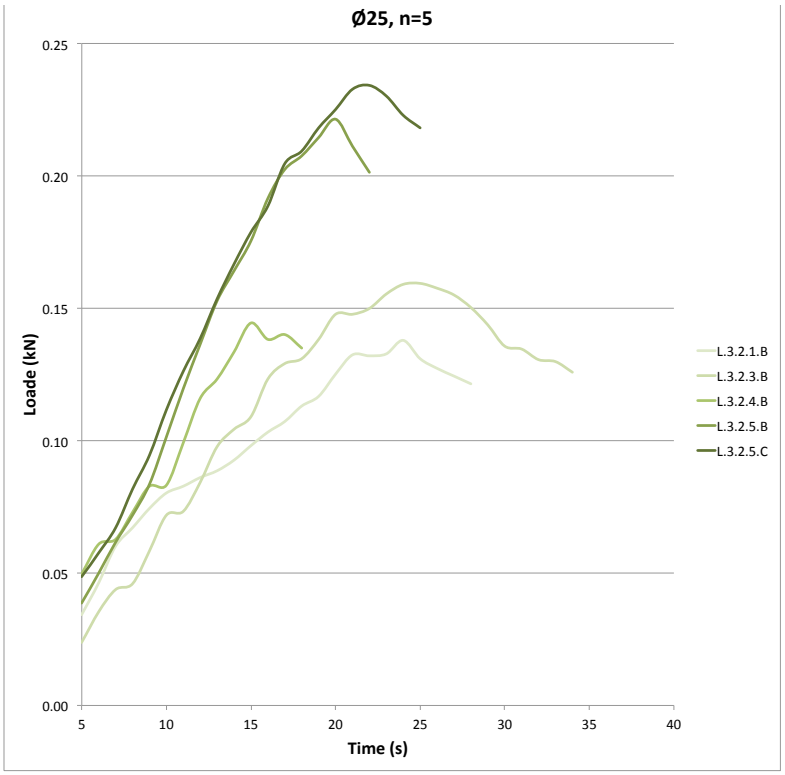

Figure 3.17. Load vs. Time graph for the calculated running average of the specimens used as examples for layer 3. The specimen used are L.3.2.1B, -L.3.2.3B, -L.3.2.4.B, -L.3.2.5B and –L.3.2.5C. The specimens are prepared with an ideal diameter of 25mm.

The five specimens used as examples show distinctive paths for each specimen (fig.3.17). Despite the relatively homogenous critical loads found for the specimens their development is distinctive for each cylinder. L.3.2.5B and C clearly display this, as the slope of their curve is steeper and easily distinctive from the other specimens. The other specimens all have different cylinders as origins, and therefore their accumulation of strain is different. Compering them with other specimens originating from the same cylinder it becomes evident that these specimens also follow the same pattern. This illustrates the importance of a homogeneous sample material. The critical loads recorded range from approximately 0.29 kN for L.3.2.5C to just below 0.20 kN for L.3.2.1B.

A set of sample specimen was prepared with a diameter of circa 38mm. The data recorded from these specimens are less affected by instrumental interferences during testing at low loads because they are able to accumulate strain at a higher level than their smaller counterparts. The specimens as a population display an overall trend similar to the one found in the specimens with a diameter of 25mm. In total seven specimens were prepared with a diameter of 38mm form L.3. The individual slopes of the curves presented in figure 3.18 define an overall trend in the dataset. The specimens

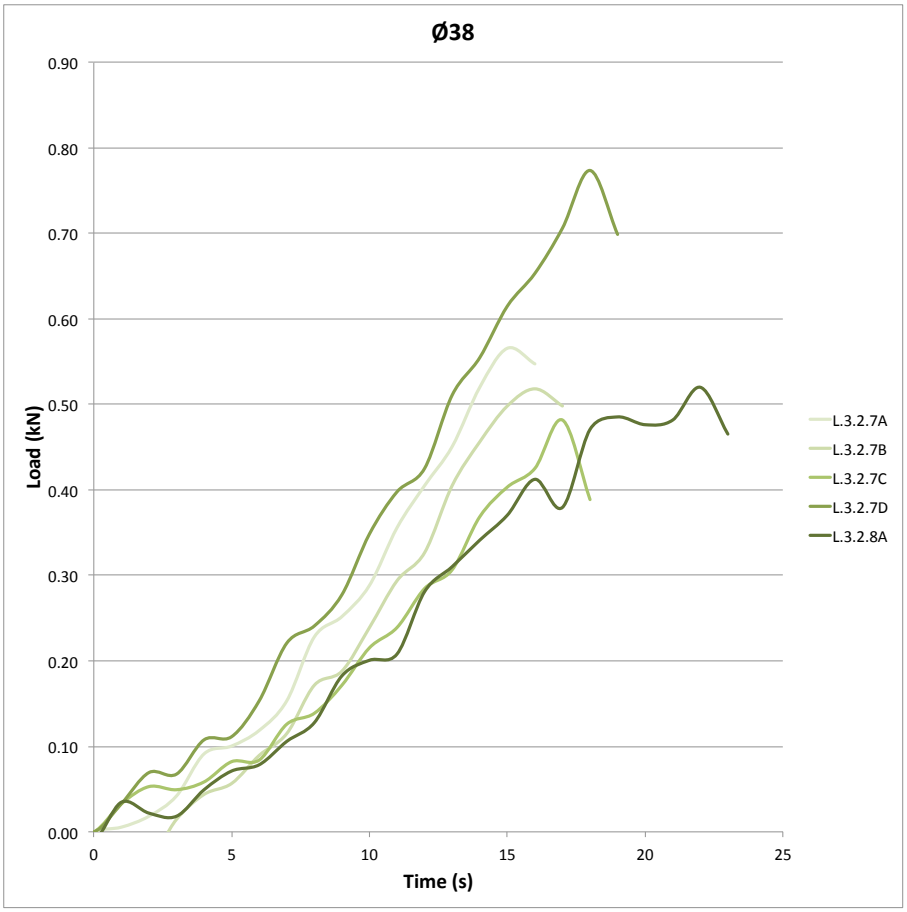

Figure 3.18. Load vs. time graph for layer 1, based on specimens L.3.2.8A, -L.3.2.7A, -B, -C and –D. These specimens are prepared with an ideal diameter of 38mm.

are showing a similar accumulation of strain over time, not found in the specimens prepared with smaller diameter.

The results are relatively consistent between the specimens of different diameter. The

Table 3.8. Calculated indirect tensile strength for layer three, key measurements and timing of failure. The gray fields are the specimens used to create figure 3.19 and 3.20.

Sample ID	**Density**	**Porosity**	**Critical Load**	**σ_t**	**Time to fracture**
	g/cm^3	%	*kN*	*MPa*	*s*
L.3.2.1A	1.88	29.0	0.22	0.45	32
L.3.2.1B	1.87	29.5	0.15	0.31	21
L.3.2.1C	1.87	29.5	0.11	0.23	21
L.3.2.2A	1.85	30.3	0.11	0.23	26
L.3.2.2B	1.86	29.7	0.15	0.31	30
L.3.2.2C	1.86	29.9	0.10	0.21	18
L.3.2.2D	1.78	32.7	0.13	0.32	18
L.3.2.3A	1.87	29.5	0.19	0.40	22
L.3.2.3B	1.86	29.9	0.16	0.33	20
L.3.2.3C	1.87	29.6	0.18	0.38	17
L.3.2.3D	1.88	29.2	0.17	0.35	25
L.3.2.4A	1.87	29.4	0.15	0.32	20
L.3.2.4B	1.86	29.6	0.15	0.32	11
L.3.2.4C	1.87	29.3	0.15	0.32	18
L.3.2.5A	1.88	28.9	0.21	0.44	15
L.3.2.5B	1.89	28.7	0.24	0.50	16
L.3.2.5C	1.90	28.4	0.24	0.50	19
L.3.2.5D	1.88	28.9	0.23	0.48	21
L.3.2.6A	1.85	30.1	0.21	0.43	25
L.3.2.7A	1.95	26.4	0.57	0.52	15
L.3.2.7B	1.95	26.6	0.52	0.46	16
L.3.2.7C	1.95	26.6	0.48	0.43	17
L.3.2.7D	1.97	25.5	0.77	0.68	18
L.3.2.8A	1.96	26.1	0.66	0.59	34
L.3.2.8B	1.96	26.2	0.65	0.58	32
L.3.2.8C	1.96	26.1	0.74	0.66	22
Average	1.89	28.7	0.29	0.41	21

correspondences between the two groups of specimens give confidence to the results and their validity. The total average tensile strength is calculated to 0.41 +/- 0.012 MPa. Looking at the two groups separately reveals a slightly lower average for specimens with 25Ø, 0.36 +/- 0.09 MPa and a higher average, 0.56 +/- 0.09 MPa for the larger 38Ø-group.

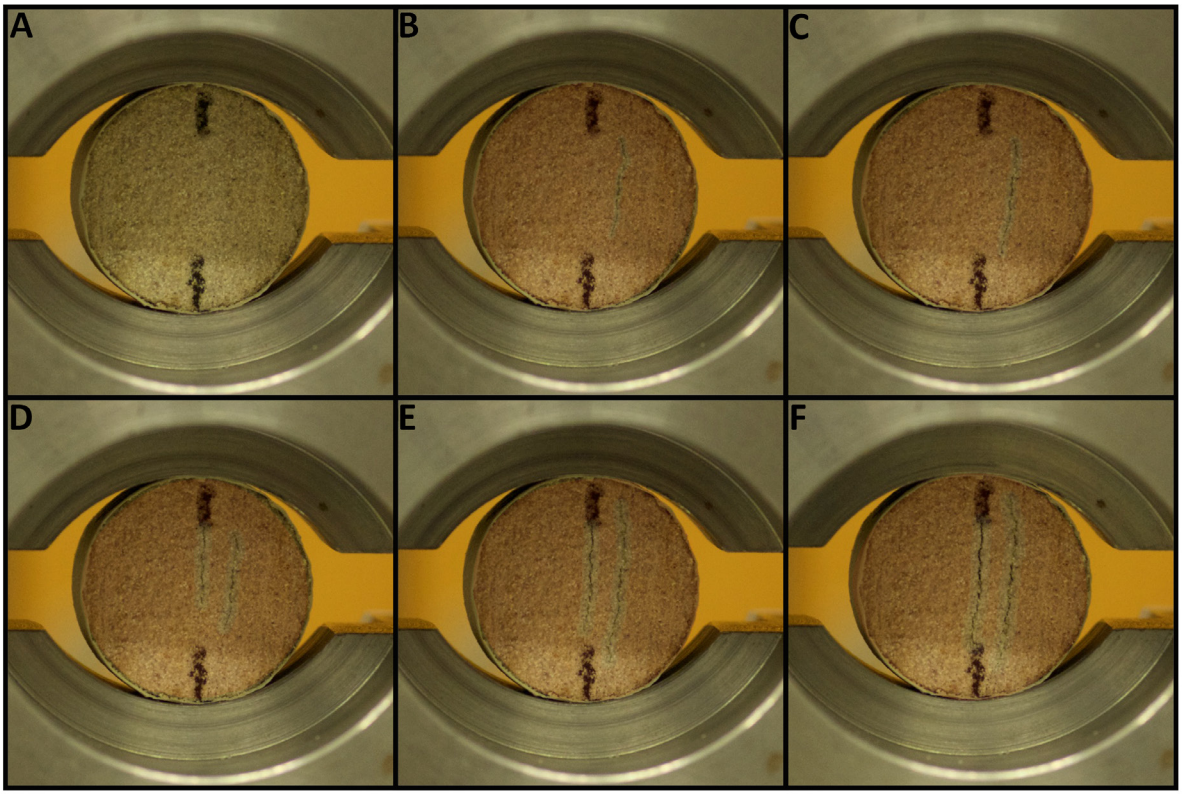

Figure 3.19. Extension fracture in Specimen L.3.2.4B illustrating the typical development of an extension fracture in L.3. The development of the fracture is divided into 6 phases. A: Pre fracture, the intact specimen unaffected by the applied load. B, Stage 1; a fracture starts developing at the right side of the specimen. C, Stage 2; the fracture propagates through the specimen utilize the layering were the least amount of resistance is found. expanding in the σ_3 direction, perpendicular to layering D, Stage 3; a second fracture is establishing itself in the middle part of the specimen. E, Stage 4; the two fractures propagates along the layering, while expanding. F, Stage 5; In the final stage the two fractures continue to expand until the load is released. The second fracture is a response to the continued deformation of the specimen, in order to keep the mass balance the specimen continues to expand perpendicular to σ_1 The fractures are highlighted with see trough shades of red applied to the figure.

Layer 4

The data collected from the forth layer is very consistent with regards to both recorded peak load and growth, i.e. accumulation of strain (fig. 3.20).

The timing of failure is relatively synchronized for all the specimens. Before failure the slopes of the specimens are insignificantly different. The specimens can be divided into two groups based on their peak load. Common for all the curves are their relatively irregular growth in the beginning, were strain is accumulated at an inconsistent rate during loading. The specimen attains a certain amount of load before the curves become linear. In the beginning they are slightly exponential.

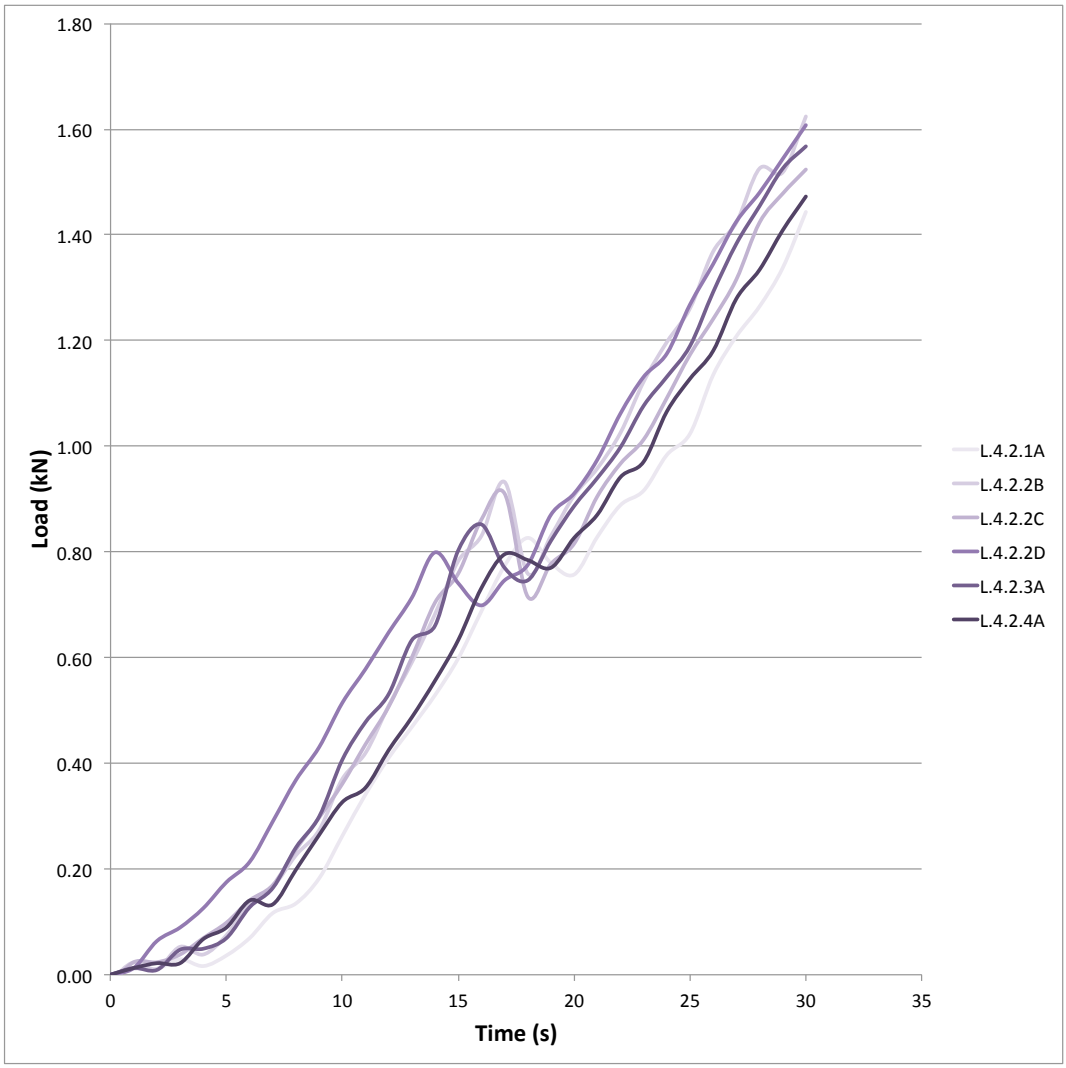

Figure 3.20. Load vs. Time graph based on the data points recorded during testing of specimens from the forth layer. The graph is based on the data of L.4.2.1A, L.4.2.2B, -C, -D, L.4.2.3A and -D

The calculated tensile strengths for the specimens are reasonably consistent throughout the dataset, which the standard deviation of +/- 0.16 reinforces. The average tensile strength for the layer is calculated to 1.66kN. This is in the low end of the examples used in fig, but the trends shown are consistent throughout the data.

Table 3.9. Calculated indirect tensile strength for layer four, key measurements and timing of failure. The grey fields are the specimens used as examples in figure 3.22.

Sample ID	**Density**	**Porosity**	**Critical Load**	**σ_t**	**Time to fracture**
	g/cm^3	%	*kN*	*MPa*	*s*
L.4.2.1A	2.27	14.3	0.83	1.67	18
L.4.2.1B	2.26	14.6	0.87	1.76	19
L.4.2.1C	2.26	14.8	0.72	1.44	15
L.4.2.1D	2.26	14.8	0.70	1.43	15
L.4.2.2A	2.26	14.6	0.79	1.62	15
L.4.2.2B	2.26	14.7	0.93	1.88	17
L.4.2.2C	2.28	14.0	0.91	1.84	17
L.4.2.2D	2.28	14.0	0.80	1.62	14
L.4.2.2E	2.27	14.3	0.72	1.46	15
L.4.2.3A	2.27	14.3	0.85	1.73	16
L.4.2.3B	2.27	14.2	0.72	1.46	14
L.4.2.3C	2.26	14.6	0.78	1.56	15
L.4.2.3D	2.30	13.3	0.83	1.69	13
L.4.2.3E	2.28	14.0	0.67	1.36	15
L.4.2.4A	2.23	16.0	0.80	1.61	17
L.4.2.4B	2.26	14.6	0.80	1.60	15
L.4.2.4C	2.29	13.6	0.96	1.93	18
L.4.2.4D	2.26	14.6	0.89	1.76	16
Average	2.27	14.4	0.81	1.63	16

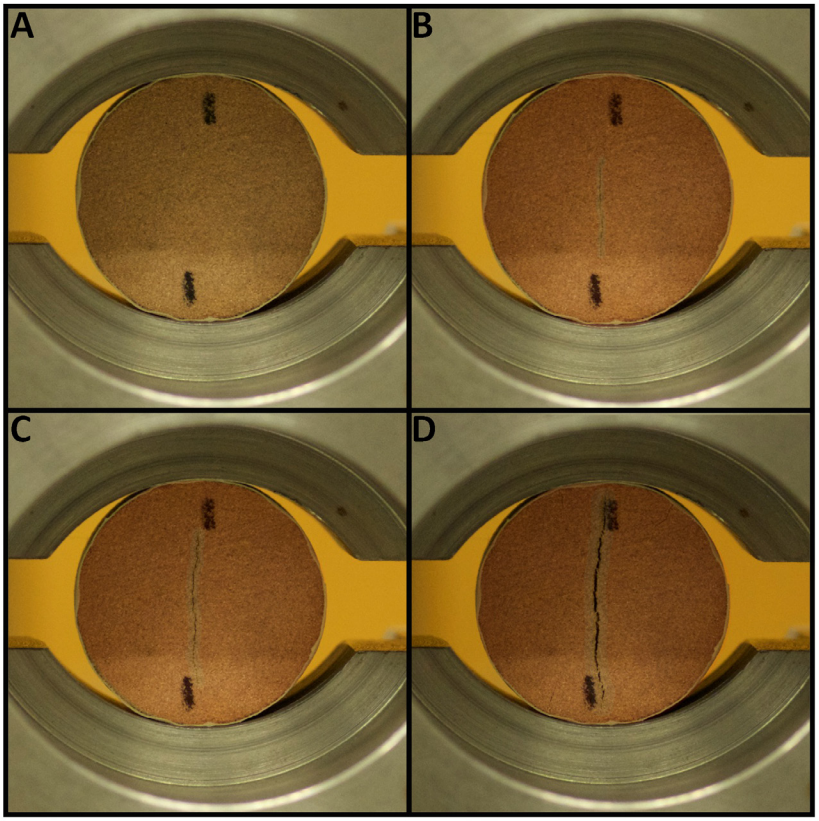

Figure 3.21. An extension fracture established in specimen L.4.2.2D during testing, used to illustrate the development of a tensile fracture in layer four as load is continuously applied. The development is divided into 4 phases. A, pre-fracture; intact specimen unaffected by the load before failure. B, Stage 1; the fracture is established in the middle of the specimen as a relatively straight fracture parallel to σ_1. C, Stage 2; in a continuation of the first stages the fracture opens and grows further and the amount of extension is becoming more significant as the fracture opens perpendicular to the axis of σ_1. D, Stage 3; in the final stage the fracture is fully developed, restricted by the size of the specimen. The fracture is still opening as a response to the continued load applied and the extensional component of the fracture perpendicular to σ_1 continues growth until the load is released. When the fracture is established throughout the specimen, smaller fractures along the edge of the specimen has starts to develop as a response to the still ongoing deformation of the specimen.

4 Discussion

The rock-sequence at Humbugflats has been thoroughly studied through fieldwork and laboratory work. Throughout the studies the main focus has been on the fracture pattern found in the exposed sequence and the differences in mechanical strength linked up to bleaching. The fractures have been measured and quantified, while the mechanical strengths of the reference layers (L.1, L.2, L.3 and L.4) have been tested.

This chapter will evolve around the trends found in the dataset, mainly discussing patterns in the fracture data and trends amongst the different properties (UCS, Tensile strength, porosity, permeability and fracture frequencies) of the reference layers. Before going further into the discussion, a summary of the results from the brazilian tests and UCS test is given in figure 4.1 and of the fracture data in figure 4.2.

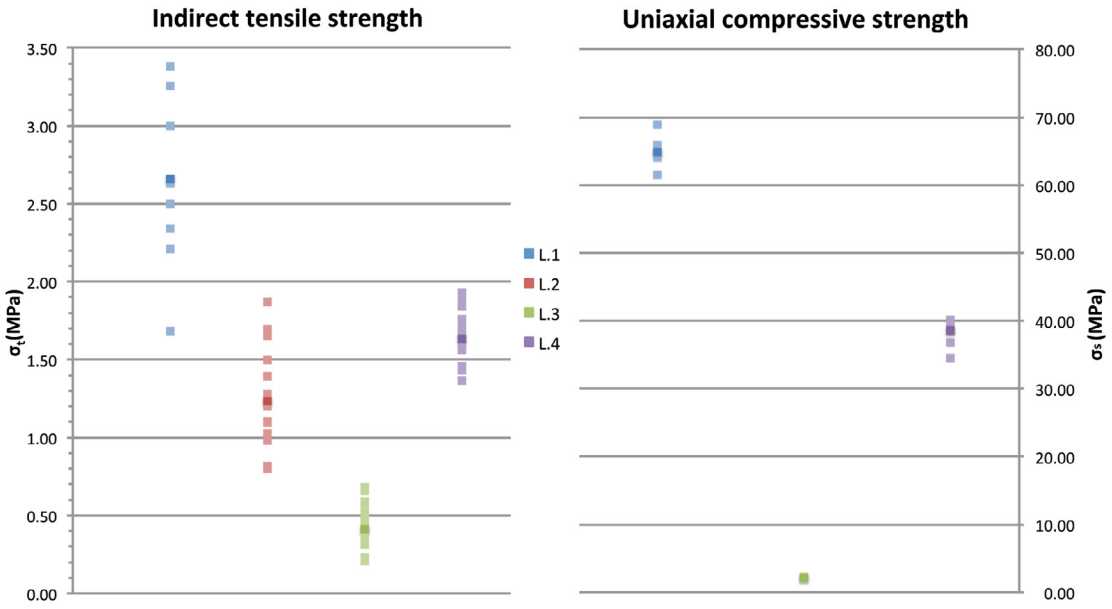

Figure 4.1 Indirect tensile strength and uniaxial compressive strength summarized. Each layer is represented with all the conducted tests and their average highlighted with a darker colored square. The figure illustrates the spread found in the results

4.1 Fracture and deformation band trends

The investigated reference layers of the rock sequence at Humbugflats have a relatively low background fracture frequency of c. 0.7 f/m (see results). Approaching the studied fault in the studied outcrop a general rise can be seen in the fracture frequency of all the investigated layers. Contrary to the fractures, there are no clear peaks in the statistical data on the deformation bands, implying that the deformation bands are related to another event. Commonly the amount of deformation bands is used as a diagnostic factor determining the width of damages zones around faults in highly porous sandstones i.e deformation band faults (Shipton and Cowie, 2001). However, in this case the fault seams to have little to no effect on the apperance of deformation bands found in the damage zone in L.3

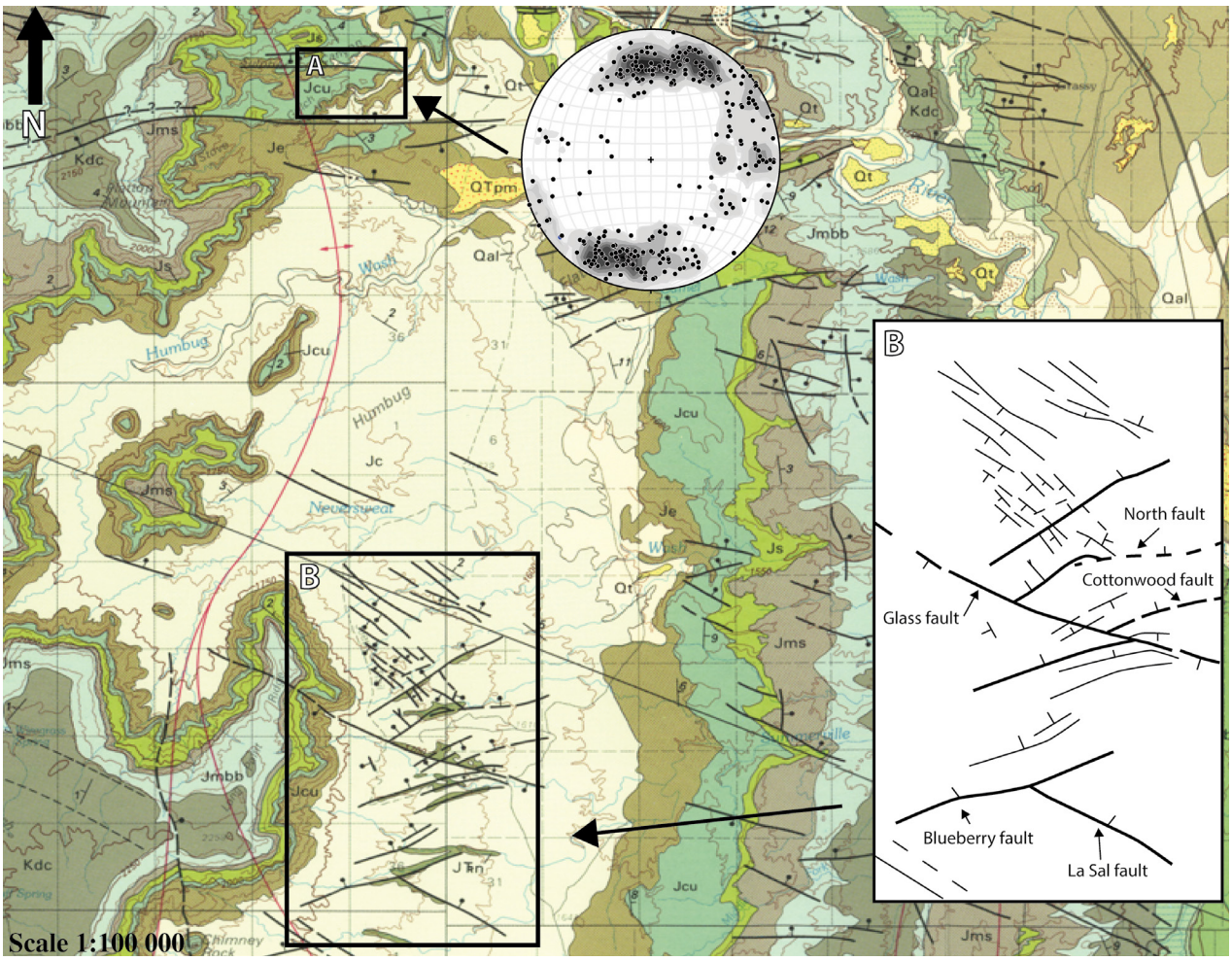

Figure 4.2 Geological map of the wider study, modified from Witkind (1988). A: Outline of the study area with included stereo-nett summarizing the fractures and deformation bands measured in the exposed sequence. B: interpretation of the chimney rock fault array based on the given map.

4.3) of conjugate fractures. Population 1 (set 1a and 1b) trends NNW-SSE, while population 2 (set 2a and 2b) trends WNW-ESE (see fig. 4.3). Pop. 1 can be related to a gentle anticline set up by a large normal fault at the northeast end of the study area (Fig. 4.2) as outlined by Ogata et al. (2014)). This large normal fault offsets the sedimentary sequence in the area with 10s to 100s of meters, juxtaposing the middle to upper Curtis Fm. in the northeast with the upper Entrada Fm. (study area) in the southwest (Ogata et al., 2014). Pop. 1 trends almost parallel to the fold axis of the gentle anticline, implying that fractures are a flexural response to the bending. These fractures are mostly found to be constrained by the interfaces of layers, i.e. they are bed-confined joints. Pop. 2 coincide with the overall trend found for the studied fault (see results), as well as the opposite dipping normal faults associated with the large normal fault to the northeast (described above). Accordingly pop. 2 are ascribed to damage from faulting. The studied fault can be regarded as an associated opposite dipping, ESE striking, normal fault array to the larger network of faults within the area (Krantz, 1988, Shipton and Cowie, 2001, Maerten et al., 2001, Davatzes et al., 2003, Ogata et al., 2014), the so-called Chimney Rock fault array.

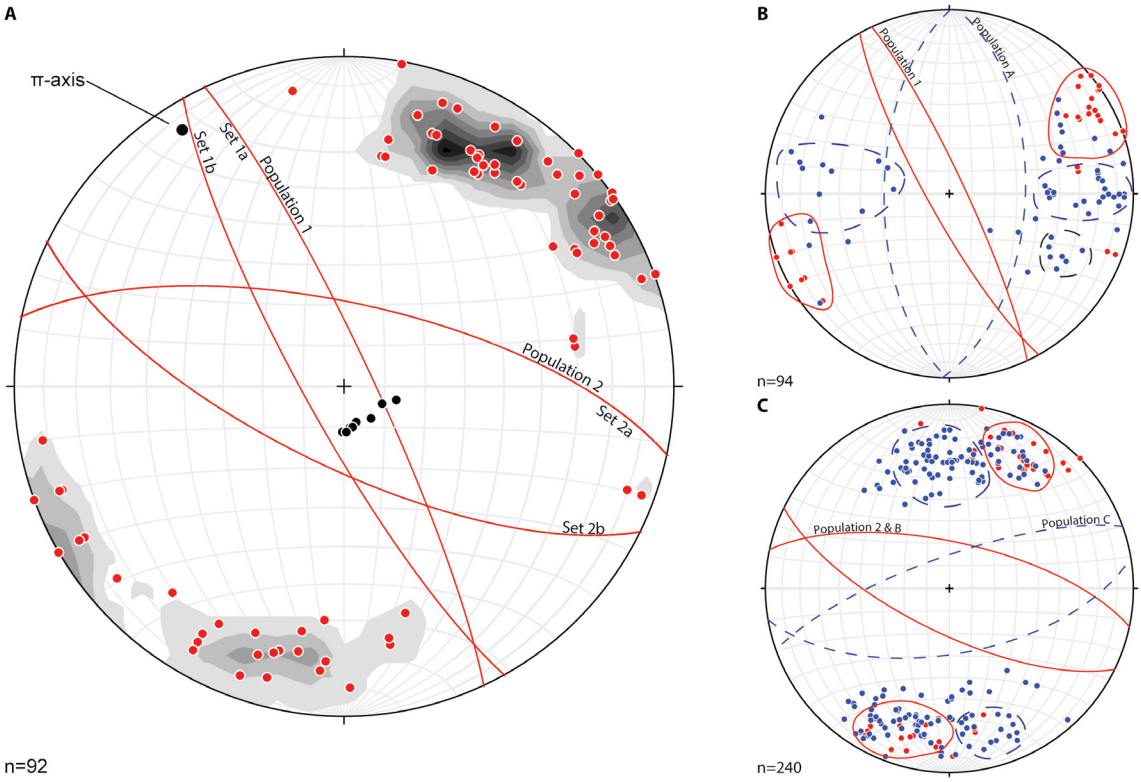

Figure 4.3 Mean fracture planes (red great circles) calculated from the strike/dip data of the recorded fractures (red poles). A: The pi-axis is the fold axis of the gentle folded strata of L.3, with strike/dip was recorded on the surface of L.3, black poles. B: Deformation bands (blue) related to the fractures trending NNW-SSE (red). A red stippled ellipse indicates a group of deformation bands not belonging to the larger trends found in the dataset. C: Deformation bands (blue) related to the WNW-ESE trending fractures (red). Too emphasize the general trends found in the dataset circles have been drawn around the sets to illustrate how the trends are found.

The fractures and faults found within the sequence at Humbugflats can arguably, based on the relations described above, be ascribed to the larger tectonic regime that created the Chimney Rock fault array, a few kilometers SSW of the study area at Humbugflats (as shown in fig. 4.2). The fractures are either directly (pop. B) or indirectly (pop. A) related to the fault array. Fracture pop B fall within the tectonic regime setting up a number of WNW and ESE striking faults, within the northern part San Rafael Swell, exemplified by the Glass fault, La Sal fault and numerous smaller faults associated with the normal fault northeast of the study area at Humbugflats (Krantz, 1988, Maerten et al., 2001, Davatzes et al., 2003, Ogata et al., 2014). Fracture pop. A is proposed to be indirectly related, as a flexural response to the bending of the sequence setting up the dome in response to the tectonic regime, as the population trends parallel with the fold axis of the gentle anticline measured (see results). As these folds have such a low dip, the scatter in the bedding plane measurements can have been analyzed in a way that the found axis is the sum of the two anticlines, setting up the dome. Some uncertainties with regards to this population therefore have to be accounted for.

Although the origin of the normal faults found in the Chimney rock fault array is uncertain, they are likely to be a response to extension before and/or during Laramide uplift (Shipton and Cowie, 2001). There are conflicting views on the stress regime the array is formed under. For instance, Krantz (1988), Shipton and Cowie (2001) and Maerten et al. (2001) regard them as formed as a orthorhombic system in a three-dimensional strain field (3D hypothesis), with maximum strain in the N-S direction, minimum strain in the E-W direction and the last strain axis vertical. Davatzes et al. (2003) conversely propose a non-coaxial strain history (non-coaxial hypothesis), with two phases of deformation based on the style of formation and cutting relationships; deformation bands followed by joints and shearing of joints. The first phase of deformation is related to faults and deformation bands striking ENE-WSW as a response to NNW-SSW extension. The second phase of deformation in the fault array, defined by joints striking WNW-ESE as a response to NNE-SSW extension. On the contrary, 3D hypothesis the faulting is ascribed to one event. It is worth noting that the large monocline of the San Rafael swell has a N-S fold axis consistent with E-W shortening, which could allow N-S extension by lateral escape of material.

The E-W trend links the faulting down towards the Moab fault and Salt Wash Graben, confining W on the little Grand Wash fault and Salt Wash Graben, and from there to Smiths Cabin at the San Rafael swell. These faults are active in the late Cretaceous, possibly as late as Paleocene (Foxford et al., 1998, Frery, 2012). Richey (2013) suggests that the faults following these paths are even younger then the San Rafael Swell.

The structural framework used to explain the fracture patterns can to a large extent explain the formation of deformation bands in L.3. The deformation bands define three relatively large populations of conjugate sets. Some band populations are falling directly within the framework already defined by the fractures. The populations are defined by the mean trend of the conjugated bands, deformation pop. A (N-S), deformation pop. B (WNW-ESE) and deformation pop. C (ENE-WSW). Some of the deformation band pops. can be related directly to the fracture pops., fracture pop. 2 is directly related deformation band pop. B. Furthermore there is a minor set of NNW striking bands with a SW dip coinciding with fracture pop. I (NNW-SSE), indicating a relation to the flexural response to folding (See above).

The remaining pops. can all be ascribed to the regional tectonic regime, deformation band pop. B and C both fall within the general trends found in the Chimney Rock fault array, as described above (Fig. 4.2 and 4.3). Deformation band pop. B coincides with fracture pop. 2 and add deformation bands to the WNW-ESE trending population, defined by the faults in the study area and related to the Chimney rock fault array (see figure 4.1) (Davatzes et al., 2003, Ogata et al., 2014). The final set, deformation band pop. C, coincide with the first population of faults in the Chimney Rock fault array, defined by deformation bands (see above for description). The described faults trending ENE-WSW in the Chimney Rock fault array have associated sub parallel joints to the faults and deformation bands, as highlighted Davatzes et al. (2003). The dataset from the study area lacks related fractures in the ENE-WSW direction. However, a number of deformation bands can be related to the fractures trending WNW-ESE, making the link imposed questionable as fracture set II and deformation band pop. B in this case should be linked to the second phase of faulting in the array. It is also important to note that fractures and joints trending ENE-WSW can be suppressed in the datasets, as the 1D scan lines used to document the fractures in the study were gathered parallel to the exposure, NE-SW (see methods).

An alternative to the proposed explanation above is related to the double-anticline, dome like feature the study area is a part of. The dome is composed of two folding events where the rollover structure set up by the normal fault array northeast of the study area makes up the ENE-WSW trending fold. The WNW-ESE fold makes up the second structure (Hope, pers.comm 2015). Fracture pop. I can still be explained as a flexural response, but the improvement to the model is that it explains deformation band pop. C. The deformation band pop. B is in this model explained as a flexural response to folding by the approximate WSW-ENE rollover structure, related to fracture pop. A (see above), and another folding event trending WNW-ESE, related to fracture sett II running

parallel with the folding. The second fold can also be related to deformation band pop. C as these would be oriented 90° to the fold axis and therefore being compressed.

4.2 Mechanical strength correlations

The stratigraphic sequence at Humbugflats is relatively homogeneous (fig 4.4), consisting of mostly fluvial plain/ overbank deposits (facies A), exemplified by two reference layers, L.1 and L.4. Inside the succession of overbank deposits a bed set of upwards coarsening sandstone appears, starting with a fluvial sandstone, L.2 (facies E), followed by a highly porous eolian sandstone layer, L.3 (facies F) on top eolian deposits are mottled by roots in a 30-40 cm top layer (see results; table 3.1 and fig 3.2).

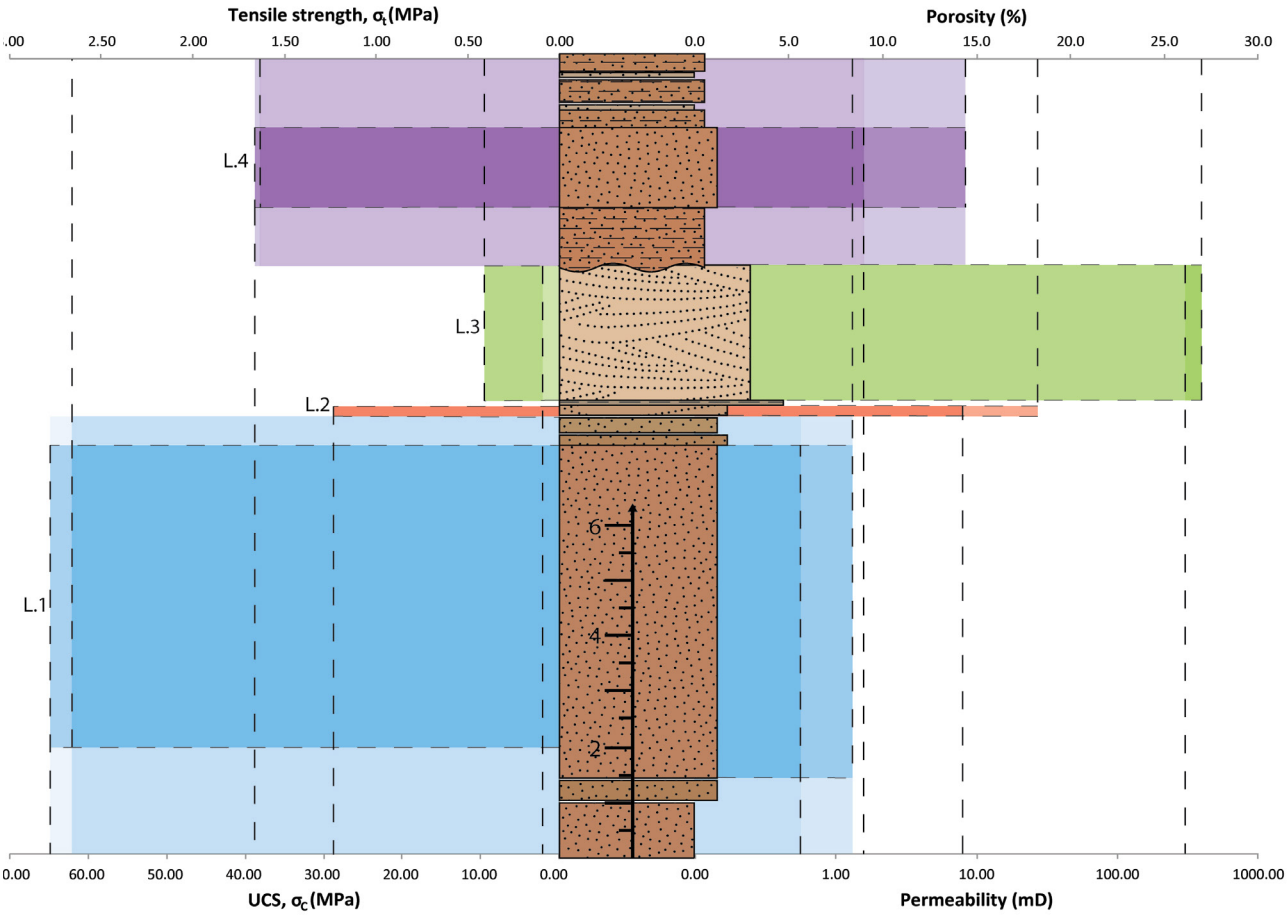

Figure 4.4 Section of the stratigraphic log illustrating the observed relationship between the strength, σ_t and σ_c, and the petrophysical properties, i.e. porosity and permeability. The color indicates which layer the results are obtained from, L.1: blue, L.2: red, L.3: green and L.4: purple. The results are inferred to be applicable for the related facies, shown with lower intensity colors.

The slight shift in depositional environment is reflected in the dataset produced from laboratory testing. The strength of the layers decrease in the fluvial-eolian section, while the porosity and permeability increases. A rough estimation shows that the properties can be oppositely correlated, a slight increase in porosity results in a decrease of both tensile strength and UCS, as shown in fig. 4.4

The data collected on the reference layers outline an empirical relationship between UCS and porosity, as has been shown for other siliciclastic rocks (Dunn et al., 1973, Vernik et al., 1993, Palchik, 1999, Palchik and Hatzor, 2004).

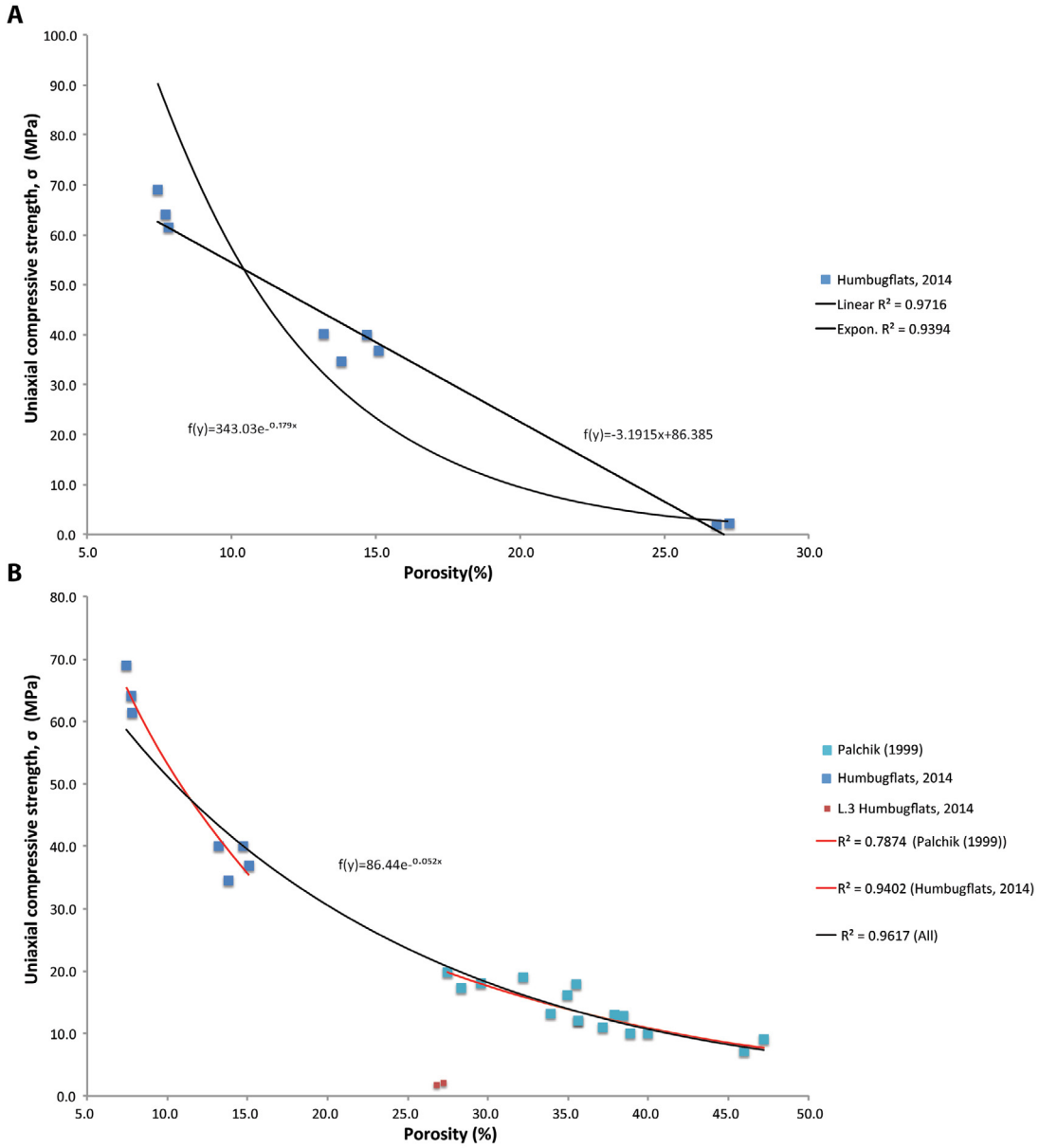

Figure 4.5 Correlation between UCS and Porosity for; A: Dataset gathered on samples from Humbugflats, the three populations are reflecting the sample layers. The population with the highest porosity/lowest strength is L.3, with the decrease of porosity being L.4 followed by L. The correlation can be described both by a linear and an exponential equation. B: Palchik (1999) dataset plotted against Humbugflats data, exhibiting a exponential relationship.

The correlation found in the data can be described with both a linear and an exponential equation. The absence of measurements form L.2 makes it harder to determine which of the two should be regarded as the best fit, although the highest regression is found for the linear equation. It is however important to note that previous work conducted on larger datasets have concluded on a best fit to an exponential relationship (Palchik, 1999, Palchik and Hatzor, 2004). Because of the limited size of the dataset gathered

the data is plotted against the correlation of Palchik (1999) found between UCS and porosity (see fig. 4.5B). Extrapolating the correlation between the two datasets further strengthens the empirically observed dependency between the UCS and porosity (see fig. 4.5B). In order to produce a correlation with statistical significance (R^2 values) the results of L.3 were removed from the trend. The found relationship highlights a problem with the results obtained from L.3; the UCS for this layer, 2.13MPa, is significantly lower than what has been found for other rocks with similar properties (Palchik, 1999, Kahraman, 2001). This implies that the results either are valid, meaning that the rock is far weaker than what could be expected, or the produced results found are unconnected to the actual UCS of L.3.

The fractures generated during testing of L.3 were only tensile fractures. Normally the type of fracture produced is dependent on the test conducted. Brazilian tests produced tensile fractures (extension fractures), while UCS test produced shear fractures. This is the case for all the reference layers except for L.3 (see results: fig. 3.9). The data presented in figure 4.1 illustrates the low strength found for L.3, having a negative relationship between the tensile strength and UCS, unlike what is found for the three remaining layers tested, were the relationship is marginally positive. Essentially these findings suggest that the L.3 layer is incapability of produceing compressive failure without confining pressure, and that this is the reason for the a low measured UCS. Accordingly the low UCS values for L.3 cannot be ascribed to the high porosity found for L.3, as other high porosity layers produce fitting results (e.g.(Palchik, 1999)).

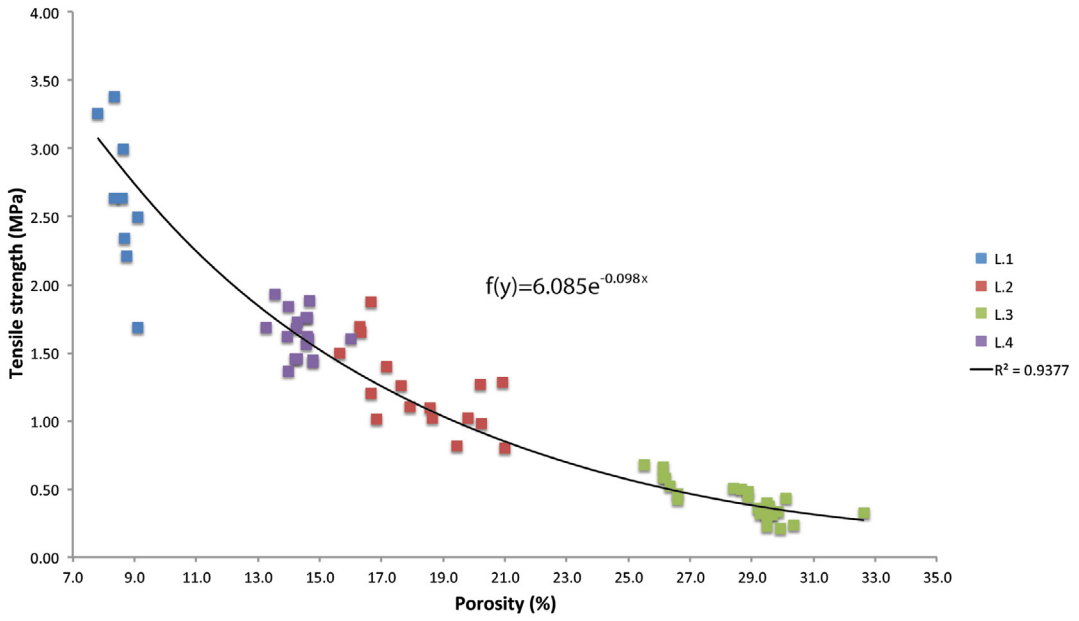

Figure 4.6 Correlation between tensile strength and porosity. Tensile strength and porosity of 71 specimens from the reference layers generating a exponential correlation of the two.

Previous work has focused on the link found between UCS and porosity, only touching on the subject of tensile strength vs. porosity. It has been inferred that there is a link; however, the assumed trend would be too weak to produce a mathematical model (Palchik and Hatzor, 2004). In the dataset from Humbugflats, targeted layers L.1, L.2, L.3 and L.4, the correlation between tensile strength and porosity can be expressed by an exponential equation, with a very robust R^2 value. The increase in tensile strength follows the decreases in porosity much like with the UCS. As with the other parameters of strength, L.3 is the weakest layer while L.1 is the strongest. The exponential trend that best fit the tensile strength versus porosity shows that the total strength of a rock is dependent of the porosity of the rock in question. This is a unique finding that needs to be verified by a larger datasets.

4.3 Bleaching

One of the large unanswered questions regarding the studied sequence at Humbugflats is whether or not the presumed bleached paleo-reservoir (L.3) once was red like the surrounding red sandstones, exemplified in this study by L.1 and L.4. the answer to this question directly relates to the motivation of this study; what caused the geomechanical differences in the studied rocks?

There are several indicators to bleaching in L.3, but none of which are conclusive. However, there are strong empirical evidence present. L.3 is a part of a dome/ anticline structure ideal for entrapment of hydrocarbons or buoyant fluids. The high porosity and permeability in the eolian sandstone, 27% and 409mD, suggest that this unit is the preferred reservoir of the exposed section. The remaining units, L.1, L.2 and L.4 all have significantly lower porosity and permeability (see results), making them undesirable as reservoirs. In the discussed fracture networks in the lower red sandstones (see above) the fractures associated with the fault are exposing bleaching trends assumed related to fluid paths along the fractures as also concluded by Ogata et al. (2014). These fluid paths discolored the red massive sandstone along the fractures. Just before these fractures reach L.3 they branch, forming fracture fans with bleaching fronts transgressing from the massive red sandstones into the fluvial (L.2) and eolian (L.3) sandstones above (fig. 4.6 A and B).

A closer look at the mineralogical composition of massive red sandstones and the white eolian sandstone exhibit two distinctive compositions. An important note to make before going further into details is that these rocks are formed during different depositional events, so a natural difference in composition is expected. In the red sandstones there is iron oxide cement present in the quartz-dominated mineralogy, while in the eolian sandstone almost no hematite is present, except for a few minor grains (Hope, pers. comm 2015). Substantial evidence of hematite removal would for instance be an enclosed hematite grain within the impermeable deformation bands, enclosed in the band prior to or during the introduction of a reducing fluid. This is not the case as the few grains found are present within the host rock of the bands (L.3). Despite this there is evidence of a reducing fluid in the form of K-feldspar alterations within L.3. (Hope, pers.comm 2015).

The anticline/dome structure and the placement of the bleached L.3 conforms to the previous spatial distribution analysis of bleaching in the region. Beitler et al. (2003) have, using Landsat 7 images, found the highest concentrations of bleaching within

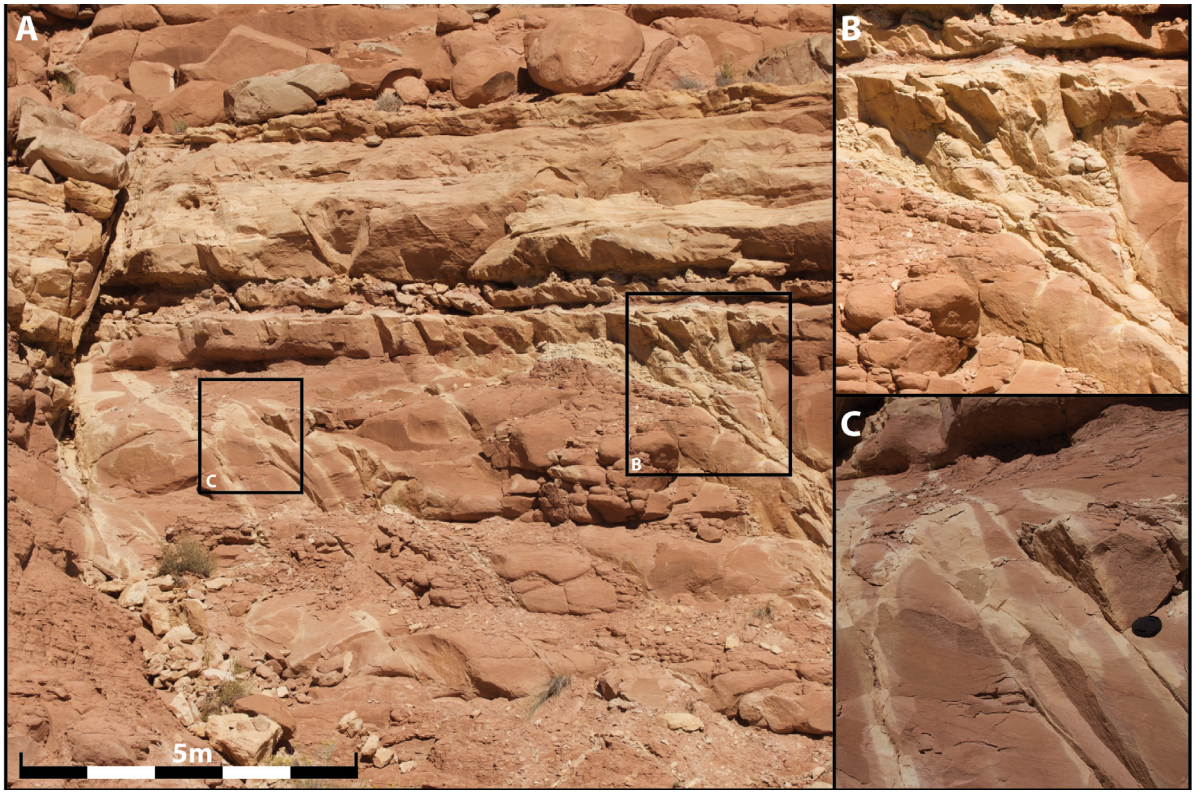

Figure 4.7 A: Bleaching pattern around the studied fault and related fractures. B: Bleaching front widening in a fracture fan towards L.2 and L.3 (white sandstone). C: Close up of bleached fractures in surrounding red host-rock (L.1).

the Navajo Sandstone to be constrained to the flanks and crests of the eroded Laramide uplifts, amongst these the San Rafael swell. This suggests that the reducing fluids must have been buoyant, and traveled up faults or layers before being enclosed by structural traps. This observation is supported by numerous studies (Foxford et al., 1998, Garden et al., 2001, Dockrill and Shipton, 2010, Ogata et al., 2014), showing that fluid flow along faults have allowed bypass of sealing layers and charging of starched reservoirs. removal of said coting.

Garden et al. (2001) describe three styles of iron oxide reduction derived from observations in the Moab anticline; complete reduction, zones of partly removal showing integrated red and white sandstones, and areas of intense bleaching in structural traps (e.g. anticlines and domes). The later two of the styles of reduction can be proven substantiated by empirical observations, as it is difficult to disagree on observed discoloring side by side with the original red sandstone (fig 4.7). On the other hand, complete hematite removal is harder to prove with empirical evidence, as they alone are not substantial enough to be conclusive. Ogata et al. (2014) propose that normal faults and related fractures form pathways/corridors the fluids utilize, allowing fluid flow between reservoirs at different stratigraphic levels, based on the study of normal faults in close proximity to the field area at Humbugflats (discussed above). These fracture

corridors are characterized by bleaching haloes along the fractures, similar to the ones described from the study area (fig. 4.7). As these and other normal faults in the area have facilitated fluid flow, it is reasonable to suggest that reducing fluids reached L.3. and caused nearly total removal of hematite.

Thin-sections of L.3 display albitization of k-feldspar in a large numbers of the grains present (Hope, pers.comm 2015). This is conforms with petrophysical investigations conducted by Beitler et al. (2003) on Navajo sandstone, where the bleached samples generally are characterized by K-feldspar alteration and lack of hematite coatings. This implicates that there must have been a reacting fluid present in L.3. Thus evidence for bleaching requires a reducing fluid containing Na^+ and CHO_2. Simplified reactions for the two can be set up after Saigal et al. (1988) describes albitization (1) and Garden et al. (2001) address hematite reduction with hydrocarbon fluids (2).

$$KAlSi_3O_8 + Na^+ \rightarrow NaAlSi_3O_8 + K^+ \qquad 1$$

$$CH_2O + 2Fe_2O_3 \rightarrow CO_2 + H_2O + 4FeO \rightarrow HCO_3^- + H^+ \qquad 2$$

4.4 Model for temporal geomechanic development

The discussion above can be summarized in a chronological model, from faulting and related fractures until the final exhumation occurs in six stages. A few relative ages needs to be discussed before going into the model.

As discussed above, a fluid would upon entering the succession utilize the fracture conduits generated by faulting (see fig 4.8: stage 1 and 2), an potentially increased fracturing due to fluid pressure (Ogata et al., 2014). When the fluid is introduced to the succession it favors the High porosity and permeability eolian L.3 over the low porosity and permeability alluvial plain L.1 and L.4 units (see above for further details). When the reduction fluid, charged with CO_2, enters the succession the removal of hematite starts, observed along the fracture and fault traces (see fig. 4.8: stage 3). According to Frery (2012) up to 98% of the CO_2 from the Chrystal geyser has an inorganic origin, suggesting that the CO_2 is at least partly from a mantel source. This can be cupped with the magmatic flair-up 20 Ma, triggering CO_2 release from the mantle, see figure 4.11 (Frery (2012))

The buoyancy driven fluids move up the structural trap (dome) as the fluid goes into L.3, saturating the sandstone and increasing the fluid pressure (see fig. 4.9: stage 4). This will effectively reduce the mechanical strength required to fracture the rock (see fig 4.8). The fluid pressure in a rock is proportional to the differential stress required to deform the rock (Phillips, 1972). Thus having a large impact on the mechanical

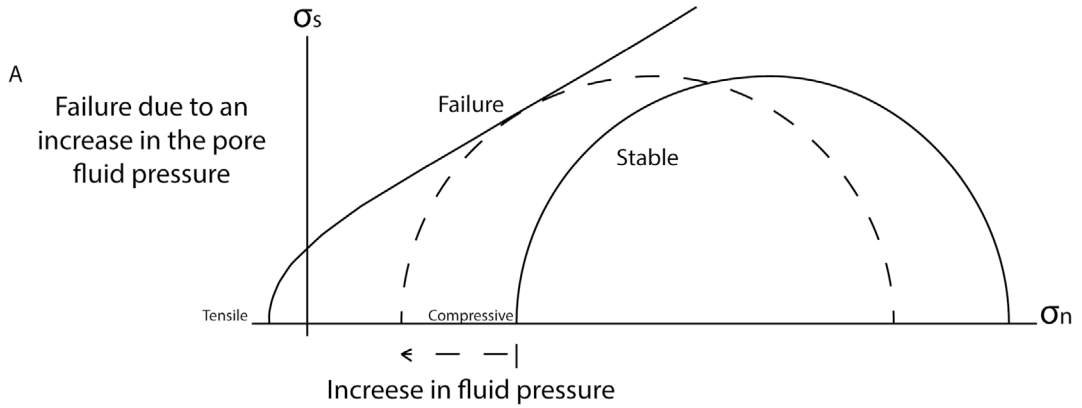

Figure 4.8 The effect fluid pressure has on the strength of a rock illustrated with the Mohr-Coulomb failure criterion. For explanation of the failure criterion see definitions. Modified from Phillips (1972).

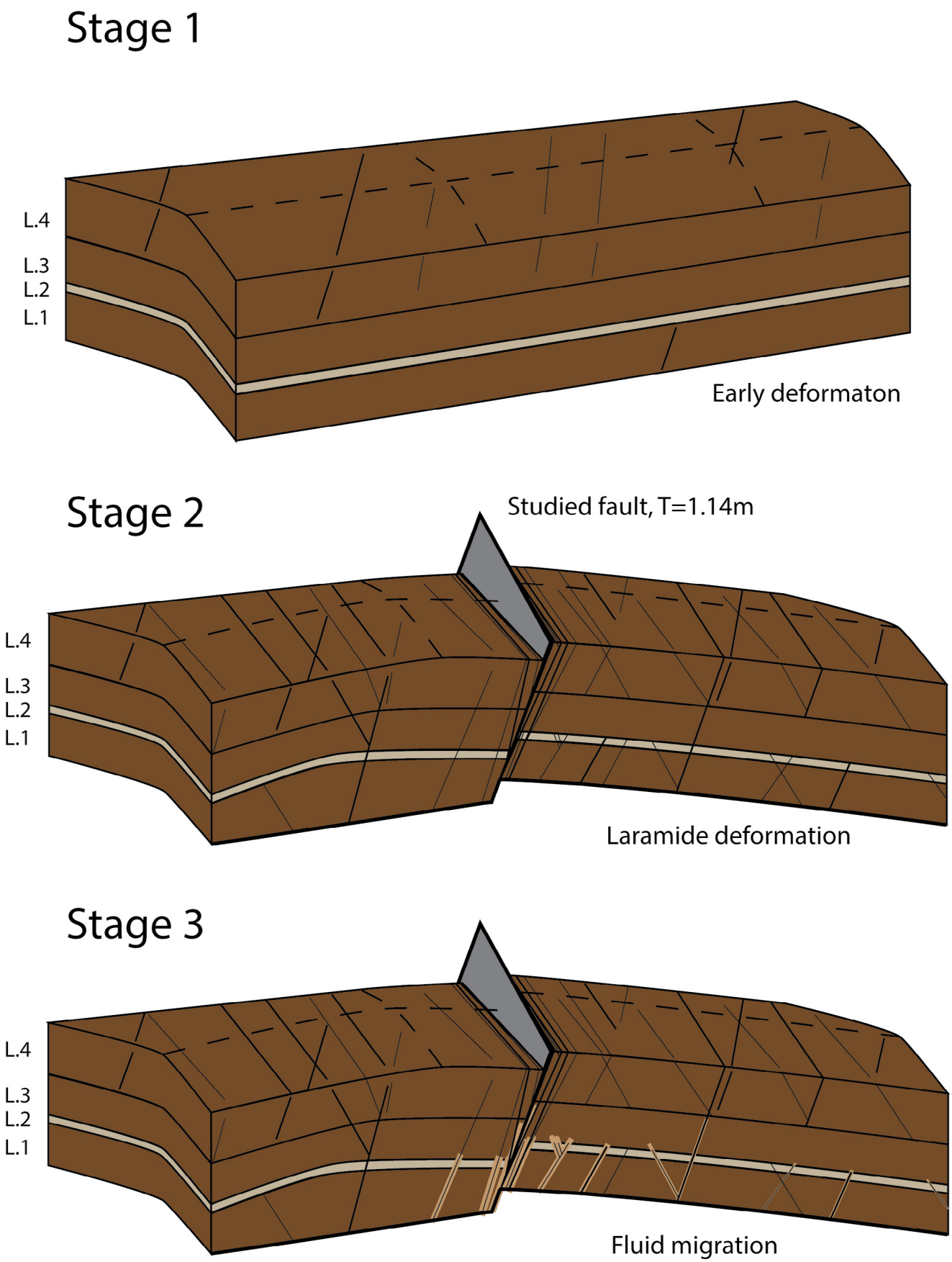

Figure 4.9 The three first stages of the proposed model. Stage 1: Early deformation setting up the first anticline. Stage 2: Laramide deformation, with related faulting. Stage 3: Fluids from a deep source migrate along the fractures, bleaching the red sandstone. The model is a sketch with vertical exaggeration to highlight the gentle dipping anticlines of the dome.

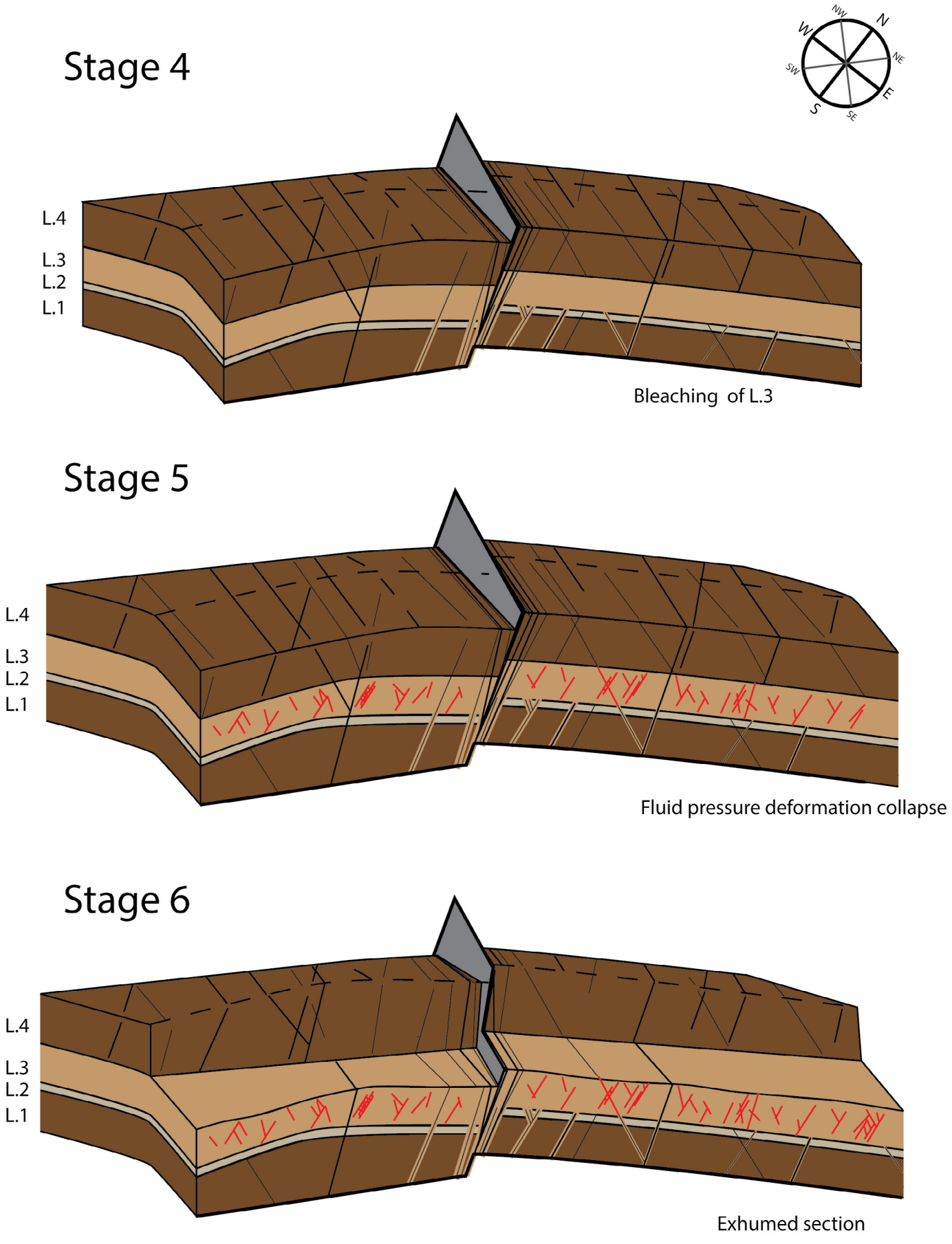

Figure 4.10 The three final stages of the proposed model. Stage 4: The reducing fluid goes into the reservoir and up in the structural trap, bleaching the entire reservoir layer. Stage 5: As the fluid is introduced to the reservoir, it increases the fluid pressure, enhancing deformation. Stage 6: Exhumation of the rocks exposes the sequence to erosion and "unroofes" the reservoir.

integrity of a layer after a critical pore pressure is exceeded for a given rock.

Alongside an increase in fluid pressure, fast removal of hematite can also be regarded as a potential cause for the "selective" deformation of L.3, generally deforming L.3 more than the rest of the sequence. The deformation mechanism of L.3 is predominantly compaction deformation band at variable frequency through the exposure (0.8 DB/m up to 8,4 DB/m) (Hope, pers.comm 2015). The deformation must be seen in conjunction with two plausible causes of deformation. Fast removal of hematite coting of the mineral grains increases the porosity in the sandstone, potentially above the required porosity for the formation dilation bands (Du Bernard et al., 2002, Beitler et al., 2003). However, an increase fluid pressure could potentially cause a collapse in the pore structure is highly likely create compaction bands rather than dilation bands as a result of the reduced effective stress (Phillips, 1972, Du Bernard et al., 2002) (see fig 4.9: stage 5) The rock sequence is eventually exhumed, unroofing the reservoir and breaching the top seal, see fig. 4.9 stage 6.

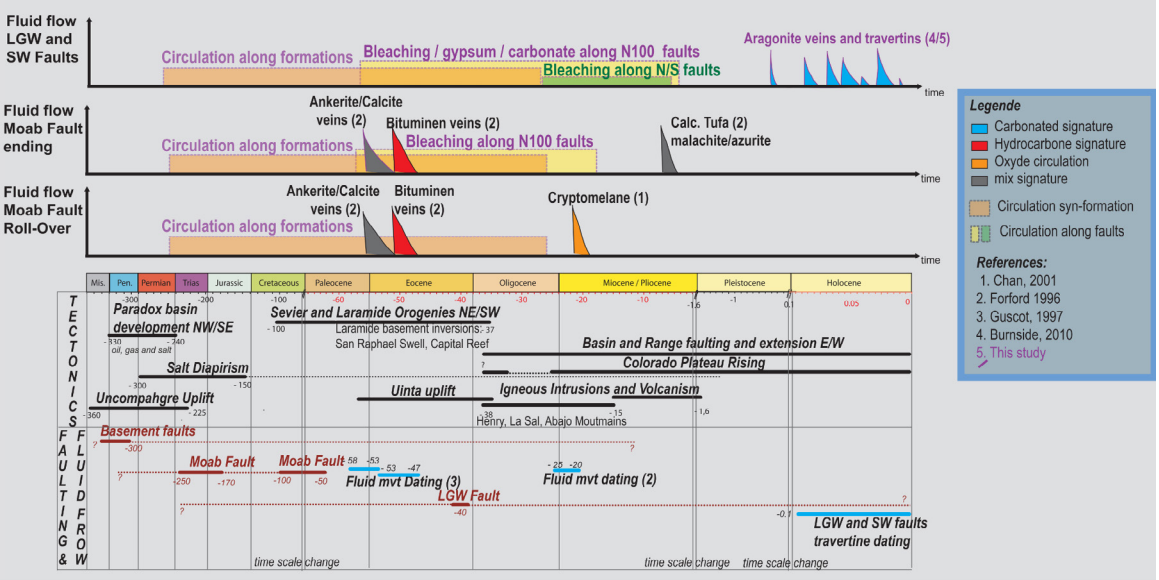

Figure 4.11 Timing of fluid flow along with major events on the colorado platau, e.g. the Laramide Orogony and Magmatic flari-up. Figure is taken form frary (2012, refrences therhin) Note: Foxford is misspeld in the original figure.

5 Conclusion and further research

5.1 Conclusion

This study has evolved around the complex fracture and deformation band patterns around faults in an exposed sedimentary sequence. These are coupled with the mechanical strength differences of the sedimentary sequence in order to get a constraint on an unroofed paleo-reservoir exposed in the sequence. Four different layers were chosen in the sequence as reference layers in order to get data on the dominant features. In total 84 fractures were recorded along ten scan lines and 82 specimens were tested for mechanical strengths. Based on these investigations, the following conclusions can be drawn:

- The strength differences found throughout the stratigraphic sequence exposed are linked to the lithological units and their composition. These differences are also to a certain degree responsible for the observed deformation of the respective layer.

Fracture trends:

- The fractures found within the studied sequence can be separated into two fracture populations of conjugate fractures based on the general trend found. Fracture pop. I trends NNW-SSE with dip towards SW and NE. Fracture pop. II trends WNW-ESE with dip towards NNE and SSW.

- Fracture pop. II and the studied fault within the field area coincide with the WNW-ESE striking faults and related fractures and deformation bands described in the Chimney rock fault array.

- Fracture pop. I is proposed to be a flexural response to the gentle anticlinal, set up by a large normal fault at the northwest end of the exposed sequence. The folding is documented with strike and dip measurements on the bedding surface of L.3.

- The fracture frequency in the reference layers increase within a zone of one meter on both sides of the fault. In L.4 the background fracture frequency goes from just above 0.7 fractures per meter to 4 fractures per meter within this zone.

Deformation band trends:

- The deformation bands outline three large sets of conjugate populations. These are

divided on the same premises as the fractures, Deformation pop. A (N-S), B(WNW-ESE) and C (ENE-WSW). The deformation set A follows the same trend as the large San Rafael anticline. The B and C populations both coincide with faults in the Chimney rock array, deformation pop. B also coincide with fracture pop. II.

- A small number of SSE striking deformation bands fall within the same trend found for fracture set I and can be explained with the same mechanism.

Mechanics:

- Uniaxial compressive strength (UCS) of a specimen can be correlated with the porosity displaying an empirical relationship between the two, where an increase in porosity results in the decrees in UCS. The correlation can be described with both a linear and an exponential equation. When only data from Humbugflats are plotted the resulting trend is inconclusive. When the results from L.3 are removed and the remaining data is plotted against data from Palchik (1999) a good conclusive correlation between UCS and porosity can be described with an exponential equation.

- Tensile strength found for the four reference layers, 71 specimens in total, exhibits a similar empirical relationship, where the degree of porosity determines the tensile strength. Like for the UCS, a high porosity results in a low tensile strength.

Bleaching:

- Traces of bleaching can be observed in L.4 along fractures related to the studied fault and fracture set II. A reducing fluid must have altered the red host rock composition, discoloring the outer rim of the fracture.

- The empirically observed fluid flow along fractures and faults within the study area confines with studies conducted by others in the area proposing fluid flow along conduits created by extensive fracturing.

- Facies A (L.1 and L.4), red sandstones have relatively high contents of iron oxides cements, while almost no hematite is present in facies D(L.3). K-feldspar alteration is common in L.3, implying that there must have been a reducing fluid present at one time.

5.2 Further research

The main goal of this study was to explain the mechanical differences causing the extensive deformation of the paleo reservoir within the studied outcrop, linking it up to the proposed bleaching of the reservoir. Further research should be conducted to establish a greater database regarding the bleaching of the reservoir. Although most of the evidence fund in this study point towards total bleaching, one would have to attain more data to achieve a higher level of confidence. In order to achieve this, sampling of rocks known too be bleached in the area is recommended. A larger set of thin-sections, collected from the visible bleached areas along the fractures in the lower part of the outcrop would enable side by side comparisons of bleached and non-bleached rocks of the same lithological units. This could in turn be compared the findings to the reservoir and potentially produce key observations.

Another aspect requiring further research is the outline a relationship between tensile strength and porosity. As briefly mentioned in the text is not as well documented in the literature as the dependency of UCS and porosity, therefore a larger data set is need to verify this. In conjunction with this relationship, the reference layers outline a linear trend between the UCS and tensile strength, as both are dependent on porosity. This trend only based on three averages, so it was not included in the work, but could potentially be statistically significant if complemented with a more extensive investigation of UCS and tensile strength in broader sense.

References

ASTM 2010. D7012–10, Standard test method for compressive strength and elastic moduli of intact rock core specimens under varying states of stress and temperatures. *Annual Book of ASTM Standards, American Society for Testing and Materials, West Conshohocken, PA*.

BEITLER, B., CHAN, M. A. & PARRY, W. T. 2003. Bleaching of Jurassic Navajo Sandstone on Colorado Plateau Laramide highs: Evidence of exhumed hydrocarbon supergiants? *Geology,* 31**,** 1041-1044.

BIENIAWSKI, Z. T. & HAWKES, I. 1978. Suggested methods for determining tensile strength of rock materials. *International Journal of Rock Mechanics and Mining Sciences & Geomechanics Abstracts,* 15**,** 99-103.

BUMP, A. P. & DAVIS, G. H. 2003. Late Cretaceous-early Tertiary Laramide deformation of the northern Colorado Plateau, Utah and Colorado. *Journal of Structural Geology,* 25**,** 421-440.

CHAN, M. A., PARRY, W. & BOWMAN, J. 2000. Diagenetic hematite and manganese oxides and fault-related fluid flow in Jurassic sandstones, southeastern Utah. *AAPG bulletin,* 84**,** 1281-1310.

DAVATZES, N. C., AYDIN, A. & EICHHUBL, P. 2003. Overprinting faulting mechanisms during the development of multiple fault sets in sandstone, Chimney Rock fault array, Utah, USA. *Tectonophysics,* 363**,** 1-18.

DAVIS, G. H. 1978. Monocline fold pattern of the Colorado Plateau. *Memoir Geological Society of America*.

DAVIS, G. H. 1999. *Structural geology of the Colorado Plateau region of southern Utah, with special emphasis on deformation bands*, Geological Society of America.

DOCKRILL, B. & SHIPTON, Z. K. 2010. Structural controls on leakage from a natural CO< sub> 2</sub> geologic storage site: Central Utah, USA. *Journal of Structural Geology,* 32**,** 1768-1782.

DU BERNARD, X., EICHHUBL, P. & AYDIN, A. 2002. Dilation bands: A new form of localized failure in granular media. *Geophysical Research Letters,* 29**,** 29-1-29-4.

DUNN, D. E., LAFOUNTAIN, L. J. & JACKSON, R. E. 1973. Porosity dependence and mechanism of brittle fracture in sandstones. *Journal of Geophysical Research,* 78**,** 2403-2417.

FILLMORE, R. 2011. *Geological evolution of the Colorado Plateau of Eastern Utah and Western Colorado including the San Juan River, Natural*

Bridges, Canyonlands, Arches, and the Book Cliffs, Salt Lake City, Univ. of Utah Press.

FOSSEN, H. 2010. *Structural geology,* Cambridge, Cambridge University Press.

FOXFORD, K., WALSH, J., WATTERSON, J., GARDEN, I., GUSCOTT, S. & BURLEY, S. 1998. Structure and content of the Moab fault zone, Utah, USA, and its implications for fault seal prediction. *Geological Society, London, Special Publications,* 147**,** 87-103.

FRERY, E. 2012. *Episodic Circulation of Reactive Fluids Along Faults: From Travertine- to Basin-scale Based on the Colorado Plateau Natural Example (USA).* PhD thesis, University of Grenoble.

GARDEN, I., GUSCOTT, S., BURLEY, S., FOXFORD, K., WALSH, J. & MARSHALL, J. 2001. An exhumed palaeo-hydrocarbon migration fairway in a faulted carrier system, Entrada Sandstone of SE Utah, USA. *Geofluids,* 1**,** 195-213.

GUDMUNDSSON, A. 2011. *Rock fractures in geological processes*, Cambridge University Press.

HINTZE, L. F. & KOWALLIS, B. J. 2009. Geologic history of Utah: Brigham Young University Geology Studies, Special Publication 9, 225p.

HOPE. 2015. *RE: pers.comm.*

KAHRAMAN, S. 2001. Evaluation of simple methods for assessing the uniaxial compressive strength of rock. *International Journal of Rock Mechanics and Mining Sciences,* 38**,** 981-994.

KRANTZ, R. W. 1988. Multiple fault sets and three-dimensional strain: theory and application. *Journal of Structural Geology,* 10**,** 225-237.

LI, C., PRIKRYL, R. & NORDLUND, E. 1998. The stress-strain behaviour of rock material related to fracture under compression. *Engineering Geology,* 49**,** 293-302.

MAERTEN, L., POLLARD, D. D. & MAERTEN, F. 2001. Digital mapping of three- dimensional structures of the Chimney Rock fault system, central Utah. *Journal of Structural Geology,* 23**,** 585-592.

MAGNABOSCO, C., BRAATHEN, A. & OGATA, K. 2014. Permeability model of tight reservoir sandstones combining core-plug and Miniperm analysis of drillcore; Longyearbyen CO2 Lab, Svalbard. *Norwegian Journal of Geology,* 94**,** 189-200.

NEW ENGLAND RESEARCH, I. 2015. *TinyPerm* [Online]. Available: http://www.ner.com/site/systems/tinyperm.html 2015].

NICHOLS, G. 2009. *Sedimentology and stratigraphy,* Chichester, Wiley- Blackwell.

O'SULLIVAN, R. B. 2010. Correlation of the upper part of the Middle Jurassic San Rafael Group in northeast Arizona, northwest New Mexico, and southeast Utah. *Guidebook New Mexico Geological Society,* 61**,** 91-100.

OGATA, K., SENGER, K., BRAATHEN, A. & TVERANGER, J. 2014. Fracture corridors as seal-bypass systems in siliciclastic reservoir-cap rock successions: Field-based insights from the Jurassic Entrada Formation (SE Utah, USA). *Journal of Structural Geology,* 66**,** 162-187.

PALCHIK, V. 1999. Influence of porosity and elastic modulus on uniaxial compressive strength in soft brittle porous sandstones. *Rock Mechanics and Rock Engineering,* 32**,** 303-309.

PALCHIK, V. & HATZOR, Y. 2004. The influence of porosity on tensile and compressive strength of porous chalks. *Rock mechanics and rock engineering,* 37**,** 331-341.

PEDERSON, J. L., MACKLEY, R. D. & EDDLEMAN, J. L. 2002. Colorado Plateau uplift and erosion evaluated using GIS. *GSA TODAY,* 12**,** 4-10.

PHILLIPS, W. J. 1972. Hydraulic fracturing and mineralization. *Journal of the Geological Society,* 128**,** 337-359.

RICHEY, D. J. 2013. *Fault seal analysis for CO2 storage: fault zone architecture, fault permeability, and fluid migration pathways in exposed analogs in southeastern Utah.* Master of Science, Utah State University.

SAIGAL, G. C., MORAD, S., BJORLYKKE, K., EGEBERG, P. K. & AAGAARD, P. 1988. Diagenetic albitization of detrital K-feldspar in Jurassic, Lower Cretaceous, and Tertiary clastic reservoir rocks from offshore Norway, I. Textures and origin. *Journal of Sedimentary Research,* 58.

SCHOLZ, C. 1968. Microfracturing and the inelastic deformation of rock in compression. *Journal of Geophysical Research,* 73**,** 1417-1432.

SHIPTON, Z. & COWIE, P. 2001. Damage zone and slip-surface evolution over μm to km scales in high-porosity Navajo sandstone, Utah. *Journal of Structural Geology,* 23**,** 1825-1844.

SINGHAL, B. B. S. & GUPTA, R. P. 2010. Applied Hydrogeology of Fractured Rocks : Second Edition. Dordrecht: Springer Science+Business Media B.V.

SOLUM, J. G., BRANDENBURG, J. P., NARUK, S. J., KOSTENKO, O. V., WILKINS, S. J. & SCHULTZ, R. A. 2010. Characterization of deformation bands associated with normal and reverse stress states in the Navajo Sandstone, Utah. *AAPG Bulletin,* 94**,** 1453-1475.

USGS 2006. FGDC digital cartographic standard for geologic map symbolization. Federal Geographic Data Committee.

VERNIK, L., BRUNO, M. & BOVBERG, C. 1993. Empirical relations between compressive strength and porosity of siliciclastic rocks. *International Journal of Rock Mechanics and Mining Sciences & Geomechanics Abstracts,* 30**,** 677-680.

WITKIND, I. J. 1988. *Geological map of the Huntington 30´x 60´ Quadrangle, Carbon, Emery, Grand, and Uintah counties, Utah* U.S Geological Survey.

Appendices 1

Table 1. The entire dataset produced from Brazilian tests from Humbugflats. As within the text, the samples are referred to by Layer then number index (e.g. L.1.2.2A = Layer 1, 2: brazilian, cylinder 2 from layer the respective layer, test A of that cylinder)

Sample ID	Diameter	Thickness	Weight	Density	Porosity	P_{max}	σ_t	Sett.	Time to failure
	mm	*mm*	*g*	*g/cm³*	*%*	*kN*	*MPa*	*Press.*	*(s)*
L.1.2.2A	25.08	12.62	15.07	2.42	8.7	1.10	2.21	900	32
L.1.2.2B	25.08	12.60	15.11	2.43	8.4	1.68	3.38	900	30
L.1.2.2C	25.05	12.63	15.20	2.44	7.8	1.62	3.26	1100	24
L.1.2.2D	25.07	12.61	15.06	2.42	8.7	1.49	3.00	1100	20
L.1.2.3A	25.06	12.60	14.96	2.41	9.1	1.24	2.50	1100	20
L.1.2.3B	25.07	12.62	15.08	2.42	8.6	1.31	2.63	1100	21
L.1.2.3C	25.08	12.59	15.10	2.43	8.3	1.31	2.64	1100	21
L.1.2.3D	25.07	12.67	15.13	2.42	8.7	1.17	2.34	1100	19
L.1.2.3E	25.04	12.67	15.02	2.41	9.1	0.84	1.68	1100	18
L.2.2.1A	25.08	12.47	13.60	2.21	16.7	0.59	1.20	1100	14
L.2.2.1B	25.09	12.54	13.60	2.19	17.2	0.69	1.39	1100	17
L.2.2.1C	25.07	12.45	13.36	2.17	17.9	0.54	1.10	1100	16
L.2.2.1D	25.07	12.72	13.53	2.16	18.6	0.51	1.02	1100	16
L.2.2.2A	25.05	12.50	12.90	2.10	20.9	0.63	1.28	1100	23
L.2.2.2B	25.06	12.42	13.07	2.13	19.4	0.40	0.82	1100	13
L.2.2.2C	25.10	12.70	13.55	2.16	18.6	0.55	1.10	1100	15
L.2.2.3A	25.11	12.48	13.61	2.20	16.9	0.50	1.01	1100	12
L.2.2.3B	25.12	12.52	13.86	2.23	15.7	0.74	1.50	1100	15
L.2.2.3C	25.12	12.55	13.79	2.22	16.3	0.84	1.69	1100	17
L.2.2.4A	25.08	12.42	12.97	2.11	20.2	0.62	1.27	1100	18
L.2.2.4B	25.07	12.40	13.00	2.12	19.8	0.50	1.02	1100	14
L.2.2.4C	25.07	12.40	12.93	2.11	20.2	0.48	0.98	1100	14

L.2.2.5A	25.11	12.48	13.48	2.18	17.6	0.62	1.26	1100	19
L.2.2.5B	25.12	12.44	13.66	2.22	16.3	0.81	1.65	1100	14
L.2.2.5C	25.12	12.45	13.62	2.21	16.7	0.92	1.87	1100	18
L.2.2.5D	25.07	12.68	13.1	2.09	21.0	0.40	0.80	1100	16
L.3.2.1A	24.69	12.58	11.32	1.88	29.0	0.22	0.45	1100	32
L.3.2.1B	24.71	12.37	11.08	1.87	29.5	0.15	0.31	1100	21
L.3.2.1C	24.74	12.50	11.22	1.87	29.5	0.11	0.23	1100	21
L.3.2.2A	24.65	12.30	10.83	1.85	30.3	0.11	0.23	1100	26
L.3.2.2B	24.66	12.43	11.06	1.86	29.7	0.15	0.31	1100	30
L.3.2.2C	24.60	12.48	11.01	1.86	29.9	0.10	0.21	1100	18
L.3.2.2D	24.58	10.42	8.82	1.78	32.7	0.13	0.32	1100	18
L.3.2.3A	24.68	12.36	11.04	1.87	29.5	0.19	0.40	1100	22
L.3.2.3B	24.65	12.52	11.1	1.86	29.9	0.16	0.33	1100	20
L.3.2.3C	24.63	12.32	10.95	1.87	29.6	0.18	0.38	1100	17
L.3.2.3D	24.62	12.39	11.06	1.88	29.2	0.17	0.35	1100	25
L.3.2.4A	24.60	12.26	10.89	1.87	29.4	0.15	0.32	1100	20
L.3.2.4B	24.62	12.25	10.87	1.86	29.6	0.15	0.32	1100	11
L.3.2.4C	24.60	12.30	10.95	1.87	29.3	0.15	0.32	1100	18
L.3.2.5A	24.53	12.48	11.11	1.88	28.9	0.21	0.44	1100	15
L.3.2.5B	24.61	12.44	11.18	1.89	28.7	0.24	0.50	1100	16
L.3.2.5C	24.59	12.35	11.12	1.90	28.4	0.24	0.50	1100	19
L.3.2.5D	24.61	12.41	11.12	1.88	28.9	0.23	0.48	1100	21
L.3.2.6A	24.67	12.49	11.05	1.85	30.1	0.21	0.43	1100	25
L.3.2.7A	37.80	18.38	40.23	1.95	26.4	0.57	0.52	1100	15
L.3.2.7B	37.85	18.92	41.39	1.95	26.6	0.52	0.46	1100	16
L.3.2.7C	37.84	18.91	41.35	1.95	26.6	0.48	0.43	1100	17
L.3.2.7D	37.97	19.04	42.53	1.97	25.5	0.77	0.68	1100	18

L.3.2.8A	37.69	18.95	41.37	1.96	26.1	0.66	0.59	1100	34
L.3.2.8B	37.66	19.02	41.41	1.96	26.2	0.65	0.58	1100	32
L.3.2.8C	37.64	19.00	41.36	1.96	26.1	0.74	0.66	1100	22
L.4.2.1A	25.04	12.59	14.08	2.27	14.3	0.83	1.67	1100	18
L.4.2.1B	25.01	12.59	13.99	2.26	14.6	0.87	1.76	1100	19
L.4.2.1C	25.02	12.68	14.07	2.26	14.8	0.72	1.44	1100	15
L.4.2.1D	25.00	12.44	13.78	2.26	14.8	0.70	1.43	1100	15
L.4.2.2A	25.02	12.42	13.81	2.26	14.6	0.79	1.62	1100	15
L.4.2.2B	25.05	12.57	14.00	2.26	14.7	0.93	1.88	1100	17
L.4.2.2C	25.02	12.58	14.09	2.28	14.0	0.91	1.84	1100	17
L.4.2.2D	25.01	12.56	14.06	2.28	14.0	0.80	1.62	1100	14
L.4.2.2E	25.00	12.56	14.00	2.27	14.3	0.72	1.46	1100	15
L.4.2.3A	24.99	12.52	13.94	2.27	14.3	0.85	1.73	1100	16
L.4.2.3B	25.02	12.56	14.03	2.27	14.2	0.72	1.46	1100	14
L.4.2.3C	25.03	12.68	14.12	2.26	14.6	0.78	1.56	1100	15
L.4.2.3D	25.02	12.52	14.14	2.30	13.3	0.83	1.69	1100	13
L.4.2.3E	24.98	12.51	13.97	2.28	14.0	0.67	1.36	1100	15
L.4.2.4A	25.04	12.65	13.86	2.23	16.0	0.80	1.61	1100	17
L.4.2.4B	25.01	12.71	14.12	2.26	14.6	0.80	1.60	1100	15
L.4.2.4C	25.05	12.63	14.25	2.29	13.6	0.96	1.93	1100	18
L.4.2.4D	24.97	12.88	14.27	2.26	14.6	0.89	1.76	1100	16